FACULTY
OF MATHEMATICS
AND PHYSICS
Charles University

Doctoral Thesis

Daria Denisova

Electroproduction of Hypernuclei

Institute of Particle and Nuclear Physics

Prague 2024

:

Bibliographic Entry

Title: Electroproduction of Hypernuclei

Author: Daria Denisova

University: Charles University, Faculty of Mathematics and Physics,
Institute of Particle and Nuclear Physics

Supervisor: RNDr. Petr Bydžovský, CSc.,
Nuclear Physics Institute, Czech Academy of Sciences.

Keywords: Hypernucleus, electroproduction of kaons, distorted wave impulse approximation, optimal factorization approximation, effective proton momentum, hyperon-nucleon interaction, shell model, Tamm-Dancoff approximation, one-body density matrix element, Fermi motion.

Abstract

In this work we explore various effects involved in the computation of the cross sections for electroproduction of hypernuclei. The model calculations are performed in the Impulse Approximation (IA) further assumed in the Optimal Factorization Approach (OFA) where the elementary amplitude is evaluated for an effective proton momentum. Our analysis introduces a general two-component form of the elementary amplitude facilitating inclusion of arbitrary effective momentum, thus accounting for Fermi motion effects. At this point, our calculations develop previous calculations performed with the zero value of the proton momentum, i.e., in the so called frozen-proton approximation. Distortion of the final-state kaon wave function is addressed via the eikonal approximation, employing an optical potential for the kaon re-scattering on the nucleus, which can be adjusted using diverse forms of nuclear density.

Furthermore, our formalism for the calculations in Distorted Wave Impulse Approximation (DWIA) accommodates a sufficiently large model space of single-particle states, which is crucial for electroproduction of the medium- and heavy-mass hypernuclei. The single-particle transition densities, represented by the One-Body Density Matrix Elements (OBDME), are obtained from various many-body calculations utilizing different forms of the effective hyperon-nucleon (YN) interactions.

This developed advanced formalism enables a comprehensive examination of predicted cross sections for the electroproduction reaction across a wide range of hypernuclei. In particular, we investigate the impact of the Fermi motion, various kinematical assumptions, the kaon distortion, as well as various many-body approaches and forms of the effective YN interactions. In our analysis we explore effects in the angular and energy dependent cross sections for various hypernuclear states, including the p-shell hypernuclei ${}^{12}_{\Lambda}$B and ${}^{16}_{\Lambda}$N, and the sd-shell hypernuclei ${}^{40}_{\Lambda}$K and ${}^{48}_{\Lambda}$K. Comparisons with experimental data for ${}^{12}_{\Lambda}$B and ${}^{16}_{\Lambda}$N highlight sensitivity of the cross sections to different computational schemes, emphasizing importance of selecting the optimum proton momentum.

Moreover, the analysis reveals systematic variations in the Fermi motion effects among groups of the hypernuclear states with a specific spin and parity, allowing to formulate a "dynamical selection rule". It was also shown that the kaon distortion significantly suppresses the cross sections, particularly for deeply Λ bound states. These effects are more pronounced in heavier hypernuclei. The predicted spectra for medium-mass hypernuclei, ${}^{48}_{\Lambda}$K and ${}^{40}_{\Lambda}$K, show a potential of the Tamm-Dancoff approach and provide insights into preparation and data

analysis of the experiments planned at the Jefferson Laboratory (JLab).

In conclusion, our comprehensive theoretical framework offers valuable insights into the complex dynamics of hypernuclear electroproduction, facilitating deeper understanding of it. It can be also utilized in preparing future experiments in hypernuclear physics.

Declaration

I declare that I carried out this doctoral thesis independently, and only with the cited sources, literature and other professional sources. It has not been used to obtain another or the same degree. I understand that my work relates to the rights and obligations under the Act No. 121/2000 Sb., the Copyright Act, as amended, in particular the fact that the Charles University has the right to conclude a license agreement on the use of this work as a school work pursuant to Section 60 subsection 1 of the Copyright Act.

In ..... date ....

Author's signature

Acknowledgement

I would like to express my sincere gratitude to my supervisor, Petr Bydžovský, for his invaluable support, guidance, and encouragement throughout my research. His expertise and patience were crucial to the completion of this dissertation.

My thanks also go to the faculty and staff of the Institute of Particle and Nuclear Physics at Charles University for their support. I am grateful to Petr Veselý and Dalibor Skoupil, my colleagues at the Nuclear Institute in Řež, for their collaboration and insightful discussions.

Finally, I am deeply grateful to my family for their unwavering love and encouragement.

List of Abbreviations

BS3	Bydzovsky-Skoupil model 3
CGLN	Chew, Goldberger, Low and Nambu
DWIA	Distorted Wave Impulse Approximation
EMPM	Equation of Motion Phonon Method
FWHM	Full Width in Half of Maximum
SLA	Saclay-Lyon A model
HF	Hartree-Fock
HO	Harmonic Oscillator
IA	Impulse Approximation
JLab	Jefferson Laboratory
L	Longitudinal
NN	Nucleon-nucleon
OPEA	One-Photon Exchange Approximation
OBDME	One-Body Density Matrix Element
OFA	Optimal Factorization Approximation
PWIA	Plain Wave Impulse Approximation
RPR	Regge-Plus-Resonance
SM	Shell Model
T	Transversal
TD_Λ	Tamm-Dancoff Λ Approximation
TL	Transverse-longitudinal interference
TT	Transverse-transverse interference
WS	Woods-Saxon
YN	Hyperon-nucleon

Contents

Preface

Production of hypernuclei, multibaryonic systems with nonzero strangeness, provides an opportunity to investigate various aspects of the strong and weak interactions in nuclei, mainly the hyperon-nucleon (YN) interaction [1]. Since very limited information can currently be obtained from the free-space YN scattering experiments, especially on the spin-dependent component of the YN interaction, hypernuclei are unique laboratories for studying this interaction [2]. Among possible hypernuclei the well established Λ-hypernuclei, atomic nuclei where one nucleon is replaced by the Λ hyperon, are the most frequently observed and studied objects [3]. In this work, therefore, the hypernucleus stands for the Λ-hypernucleus unless stated otherwise.

The reaction spectra in electroproduction of hypernuclei allow to study various forms of the YN interaction as well as other components involved in the reaction dynamics, such as the elementary-production amplitude, many-particle approach, and kaon distortion. In this work, we performed a comprehensive exploration of computing the cross sections in electroproduction of light and medium-mass hypernuclei. Our aim was to demonstrate theoretical uncertainty in predicting the cross sections, which is needed in data analysis as well as in preparation of experiments. Selected results of this study were already published in Physical Review C: "Fermi motion effects in electroproduction of hypernuclei" [4] and "Self-consistent many-body approach to the electroproduction of hypernuclei" [5] and presented at the international conferences MESON2021 [6] , HYP2022 [7], and MESON2023 [8].

Our advanced theoretical framework relies on the impulse approximation considered in the optimal factorization approximation, where the elementary amplitude is evaluated for an effective, i.e., generally non-zero, proton momentum. Therefore, central to our analysis is the development and utilization of a two-component (CGLN-like) form of the elementary amplitude for a general reference frame, which is needed to evaluate the many-body matrix element. This general form enables to incorporate an arbitrary value of the effective proton momentum wherewith effects of the proton Fermi motion in the target nucleus can be included. We aim at capturing the dynamic interplay between the values of the particle momenta and their response in behaviour of the cross sections. The effects are studied using two elementary amplitudes with different energy-momentum dependence [4].

Considering a sufficiently large model space of the single-particle states in our DWIA calculations allowed to study sensitivity of the cross sections, and herewith

the excitation spectra in the reaction, to applied many-body approaches and different forms of the effective YN interaction. We showed that the excitation spectra are considerably sensitive to the form of the YN interaction. We also provided predictions for the electroproduction on the ^{40}Ca and ^{48}Ca targets that are planned to be measured at Jefferson Laboratory [5].

Moreover, our study addresses important aspects of distortion of the final-state kaon wave function included via the framework of the eikonal approximation. This involves using an optical potential that describes the kaon re-scattering on the nucleus. This first-order optical potential is constructed assuming the kaon-nucleon scattering amplitude and diverse forms of the nucleus density.

The thesis is divided into the following parts:

In Introduction, we delve into the current knowledge of models and experiments on photo- and electroproduction of hypernuclei, providing an overview of existing knowledge in the field. We also briefly mention other hadron-induced reactions used to study hypernuclei and outline properties of interactions with strange particles.

The second chapter outlines a theoretical framework used in computing the cross sections in electroproduction of hypernuclei. Here we detail the main ingredients needed to calculate the reduced amplitudes, particularly the elementary amplitude, the radial integrals and the OBDME providing information about the nucleus and hypernucleus structure.

Results and their discussion is given in the third chapter focusing on effects from the proton Fermi motion, the kaon distortion, and various approaches and YN interactions used to determine the nuclear structure, i.e. OBDME. Here, I would also like to note a fruitful collaboration with my colleagues Dalibor Skoupil and Petr Veselý. Dalibor helped me in implementing the BS3 model for the elementary amplitude. Petr taught me the shell model and Tamm-Dancoff Λ approach and provided me with the numerical values of OBDME. I also appreciate numerous discussions with the colleagues on the results.

In the fourth chapter, we present a summary of our findings and draw conclusions from our study.

Technical details on derivation of the production amplitude, the two-component form of the elementary amplitude (CGLN-like), the spherical amplitudes, and further details on the numeric calculations are given in the appendices A – D.

1 Introduction

In the realm of nuclear physics, hypernuclei constitute a compelling field of study as they include another quantum number, the strangeness. The persisting interest in investigating the hypernuclei can be attributed to advancements in both theoretical and experimental methodologies. Moreover, presence of the open strangeness in the nucleus can also shed more light on dynamics of the nucleus, particularly it reports on relevance of the hadronic degrees of freedom in the nucleus.

When approaching the nucleus from the perspective of a system comprised of hadrons, baryons and mesons, rather than quarks and gluons, it becomes possible to introduce Λ particles into various energy states. Remarkably, this encompasses even the deeply bound states, as the Pauli exclusion principle does not act as a barrier. The relatively long lifetime of the Λ hyperon ($10^{-10}s$) in comparison with the typical time-scale of the strong and electromagnetic reactions enables the formation of relatively stable systems such as Λ-hypernuclei. These properties of the Λ hyperon open the door to studying nuclear structure. Researchers are now investigating a wide spectrum of hypernuclear systems, spanning from lighter to heavier elements along the periodic table. The obtained results broaden our understanding of atomic nuclei and their complex interactions.

1.1 Description and history of hypernuclei

The first hypernucleus, consisting of a Λ hyperon bound to a nuclear fragment, was observed in an emulsion exposed to cosmic rays. This groundbreaking discovery was made by Danysz and Pniewski in 1953 [9]. Over the following two decades, the hypernuclei have been studied using emulsion detectors, initially with cosmic rays and later with beams from existing accelerators.

In the later years, the field of hypernuclear physics has experienced a significant advancement due to the availability of modern particle accelerators and electronic instrumentation. These technological developments have considerably increased the rate and scope of experimental investigations concerning strangeness in nuclei. The hypernuclei have started to be studied on the hadron (π^+ and K^-) beams and in recent years also on the electron beams.

In 1972, the existence of a particle-unstable state of ${}^{12}_{\Lambda}\mathrm{C}$ with the Λ hyperon in the p orbit was confirmed [10]. The reaction $\mathrm{K}^- + {}^{12}\mathrm{C} \rightarrow \pi^- + p + {}^{11}_{\Lambda}\mathrm{B}$, observed in

the emulsion, was employed to study excited states of ${}^{12}_{\Lambda}$C.

From the mid-1970s onward, investigation of the p-shell hypernuclei continued utilizing the (K^-, π^-) reaction and the magnetic spectrometers. The binding energies of heavier hypernuclear systems were extracted by analyzing the spectra obtained in the (π^+, K^+) reaction, which has a higher probability of populating interior states within the hypernucleus. However, there were challenges in determining the mass or binding energy scale for most of the data. The normalization of the data to the binding energy value of ${}^{12}_{\Lambda}$C in the emulsion, which was determined from only a few events, contributed to uncertainties in the binding energies. Additionally, resolution issues in the reaction spectra added further complexity to the measurements.

To address some of these uncertainties, recent progress has been made by comparing the experimental data with $(e, e'K^+)$ electroproduction measurements which provides independent information on the binding energies [3]. This comparison has helped to refine the determination of binding energies and improved our understanding of hypernuclear structure.

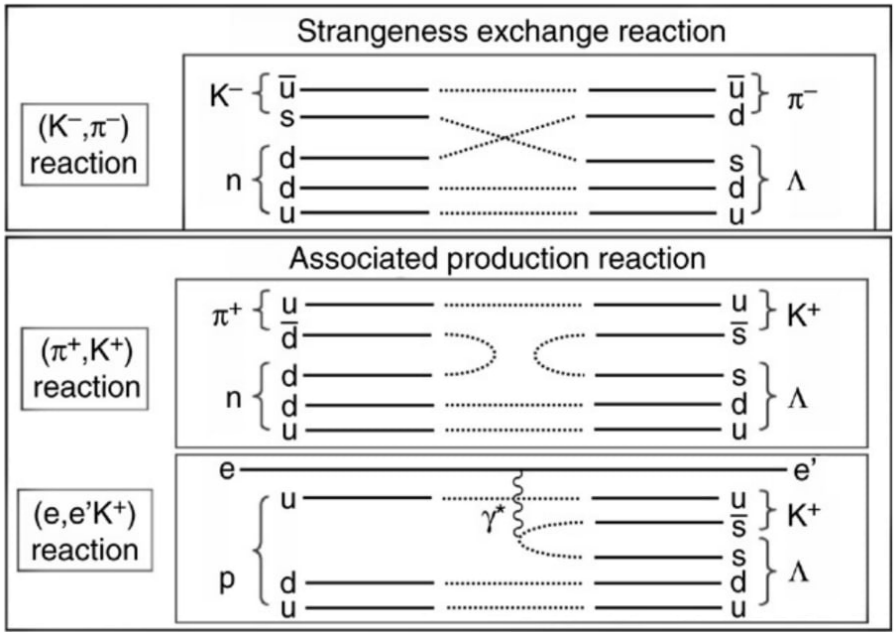

Figure 1: Schematic diagram of three strangeness producing reactions used to study hypernuclei. The figure is adopted from Ref. [11].

In Fig. 1 we show characteristic features of the elementary processes (K^-, π^-), (π^+, K^+), and $(e, e'K^+)$, used to produce hypernuclei. On the quark level, the interactions exhibit distinct features. In the (K^-, π^-) reaction, the s quark in the initial

anti-kaon exchanges with the d quark in the neutron forming the Λ hyperon. On the other hand, both in the (π^+, K^+) and $(e, e'K^+)$ reaction, a pair of the strange quarks, $\bar{s}s$, is created associated in both final-state hadrons, leading to the simultaneous production of a Λ hyperon and kaon. Therefore, as illustrated in Fig. 1, the (π^+, K^+) and (K^-, π^-) reactions convert a neutron in the target nucleus into Λ. In contrast, the $(e, e'K^+)$ reaction converts a proton to Λ. Additionally, since the spin-flip amplitudes in the $n(\pi^+, K^+)\Lambda$ and $n(K^-, \pi^-)\Lambda$ reactions are typically small unless specific kinematic conditions are met, these reactions predominantly populate non-spin-flip states of hypernuclei. On the other hand, the $(e, e'K^+)$ reaction can populate spin-flip hypernuclear states with unnatural parities. Note that hypernuclei can be also produced in collisions of heavy ions [3].

The hypernuclear reactions are significantly influenced by the momentum transfer between the beam particle and the Λ hyperon which is a crucial factor in forming the hypernuclear states. A larger momentum transfer typically results in a smaller hypernuclear cross section. Different reactions offer distinct advantages in a hypernuclear spectroscopy. The (K^-, π^-) reaction tends to preferentially populate substitutional states, where a nucleon is converted to a Λ in the same orbit without an orbital momentum transfer. On the contrary, in the (π^+, K^+) and $(e, e'K^+)$ reactions a substantial momentum is transferred to the hypernucleus as these reactions are endothermic. This characteristic allows them to excite high-spin hypernuclear states with the nucleon hole possessing a large angular momentum and the Λ with a small angular momentum. This makes these reactions advantageous for the Λ-hypernucleus spectroscopy.

Naturally, theoretical interest has closely followed the experimental progress. Researchers in the field have developed theoretical models and frameworks to explain and understand the behavior of hypernuclei and the interactions involving strange particles within nuclei. The close interplay between experimental and theoretical efforts has been instrumental in advancing our understanding of hypernuclear physics.

The behavior of the Λ hyperon in a nuclear system possesses a nuclear many-body problem due to the predominant hadronic forces between the baryons. The timescale of the strong interaction is of the order of 10^{-23} seconds, which is much shorter compared to the weak-interaction lifetime of a Λ hyperon in the nuclear medium, approximately 10^{-10} seconds [12]. As a result, the hypernuclear system can be effectively treated using well-established nuclear theory models, such as shell or mean-field mod-

els, incorporating in medium effective Λ-nucleon interaction. The Λ hyperon serves as a unique and selective probe of the nuclear medium, offering valuable insights into nuclear properties that are not easily accessible through other experimental techniques.

Numerous prior investigations have delved into the study of the electroproduction of hypernuclei. Here, we highlight notable references and authors who have contributed to these analyses.

Sotona and Žofka [13] have demonstrated that photoproduction reactions significantly polarize hypernuclear (HY) states that are strongly populated, distinct from those polarized in the (π^+, K^+) reactions. To fully unveil the rich spectroscopic information of HY states, hypernuclear productions involving (K^-, π^-), (π^+, K^+), and (γ, K^+) should be combined in corresponding kinematic regimes and on neighboring targets. This approach allows access to all parts of the hypernuclei spectra, enabling quantitative distinctions among well-defined configurations. Sotona and Žofka studied the targets with a simple structure like ^{12}C and ^{16}O considering the HY states with the pronounced particle-hole configurations.

Sotona and Frullani [14] reviewed the formalism for electroproduction processes in the one-photon exchange approximation, along with the models of elementary production based on the tree-level Feynman diagrams. Contributions of the nucleon and hyperon resonances with spin 1/2, as well as the kaon resonances with spins 0 and 1, to the amplitude were outlined in both covariant and two-component forms. While these models reasonably match available data on photoproduction cross-sections and polarizations, understanding the process remains incomplete. They highlighted discrepancies among the model predictions for the higher-energy real photons and medium-energy virtual photons. Precision measurements with both real and virtual photons could refine the elementary amplitudes, addressing theoretical uncertainties like coupling constants and the electromagnetic form factor of the kaon. They summarized the DWIA formalism for electroproduction of Λ hypernuclei, demonstrating its general features on the case of ^{16}O target. They showed that the model uncertainties strongly influence estimated cross sections and that the predicted triple differential cross section decreases rapidly with increasing virtual photon "mass" q^2. By employing more complex targets like ^{7}Li, ^{9}Be, and ^{12}C, they also showed that the electroproduction reaction is a unique tool for studying the spectroscopy of light hypernuclei.

Motivated by successful predictions of the production spectra in the first high-resolution $(e, e'K^+)$ experiments at Jefferson Laboratory on the p-shell nuclear targets,

Bydžovský, Sotona, Motoba, Itonaga, Ogawa and Hashimoto [15, 16] extended the DWIA calculations to the sd- and fp-shell regions for the first time. First, they carefully assessed available models describing the elementary process $\gamma p \to K^+\Lambda$ which is a crucial input in the DWIA calculations. They found a good agreement between four selected elementary amplitudes and the experimental data on the elementary process, particularly at energies relevant to the hypernuclear calculations in DWIA. Then their focus turned to examining the excitation spectra of $^{28}\mathrm{Si}(\gamma, K^+)^{28}_{\Lambda}\mathrm{Al}$, revealing unique features such as the selective population of unnatural-parity states attributed to the spin-flip dominance. They presented realistic excitation functions for the $^{28}\mathrm{Si}(\gamma, K^+)^{28}_{\Lambda}\mathrm{Al}$ reaction, taking into account fragmentation effects and core-excited configurations. Additionally, for the $^{40}\mathrm{Ca}$ and $^{52}\mathrm{Cr}$ targets, they observed distinct peak series corresponding to natural and unnatural parity states, respectively.

Bennhold and Wright [17] showed that the theoretical and calculation groundwork for investigating hypernuclear states through kaon photoproduction is well established. Their conclusions underscored the importance of additional photoproduction experiments to confirm the validity of the basic operator, particularly for photon energies up to about 2 GeV. Unlike previous results showing discrepancies with hadronic analyses, they observed relatively modest relativistic effects in the cross sections, especially for high-spin transitions. Their examination of nonlocalities arising from Fermi motion and the elementary-transition operator revealed notable changes in the cross sections, particularly for relativistic wave functions. Furthermore, they discovered the importance of retaining all terms in the production operator, as neglecting certain terms could lead to significant variations in the cross sections, especially for high-spin states.

Lee, Ma, Saghai, and Toki [18] investigated the $^{12}\mathrm{C}(\gamma, K^+)^{12}_{\Lambda}\mathrm{B}$ reaction by utilizing the recently developed Saclay-Lyon amplitudes of the $\gamma p \to K^+\Lambda$ reaction [19, 20] and the wave functions from the relativistic mean-field model of nuclei and hypernuclei. With the nuclear transition matrix elements taken from a shell-model calculation, they found that the predicted bound-Λ production cross section is close to the data. However, in a quasifree calculation based on a simple three-body model, they observed that the predicted unbound-Λ production is about a factor of 2 larger than the data. This discrepancy cannot be fully understood in terms of the medium effects on the incoming photons and outgoing kaons. Their results suggest that the medium effects on the Λ propagation need to be included in future investigations.

Cohen [21] discussed the importance of the $(e, e'K^+)$ reaction in hypernuclear physics, comparing it with the (K^-, π^-) reaction and suggesting specific problems that could be studied preferentially with the $(e, e'K^+)$ reaction. He provided the cross sections for both exclusive and inclusive processes across a wide range of nuclear masses. However, he noted that the elementary process $p(e, e'K^+)\Lambda$ was not well understood and rised questions about coupling constants and electromagnetic moments that called for a further discussion.

Hsiano and Cotanch [22] noted that kaon photoproduction, being the weakest nuclear interaction involving a hadron, is an ideal probe for analysis of both the nuclear and hypernuclear structure, especially for studying transition spin densities and unnatural parity states. They highlighted that the reaction mechanism is reasonably understood and amenable to an accurate theoretical description, with uncertainties primarily concerning the energy and off-shell behavior of the elementary amplitudes. For energies above 1.2 GeV, they suggested the inclusion of contributions from baryon resonances and emphasized the need for a phenomenological analysis of the $\gamma + p \rightarrow K^+ + \Lambda$ reaction for energies between 1.2 GeV and 3.0 GeV. Due to the large momentum transfer associated with the (γ, K) process, they suggested that off-shell effects may be significant and planned further detailed study. Additionally, they expressed intentions to investigate other topics such as Σ hypernuclei and kaon photoproduction through strange quark pair creation. They suggested that a comparison of a quark versus a meson-baryon exchange picture might provide useful insight, owing to the weak absorption associated with kaon photoproduction.

Shyam, Lenske, and Mosel [23] have discovered that hypernuclear production via the (γ, K^+) reaction on ^{16}O involves the excitation of $N^*(1710)$, $N^*(1650)$, and $N^*(1720)$ baryonic resonances, leading to the subsequent decay into the Λ hyperon and K^+. Although distortion effects in the K^+ channel were not considered, their impact is noted to be weak for reactions on p-shell nuclei but potentially more significant for heavier systems. The absence of nucleon intermediate states introduces some uncertainty in the total cross section magnitudes, approximately up to 10%. It was found that the excitation of $N^*(1710)$ resonance predominantly drives the hypernuclear production process, consistently with previous studies. Additionally, they observed that total production cross sections peak at photon energies slightly above the corresponding production threshold.

Shyam, Tsushima and Thomas [24] found that hypernuclear production through

the (γ, K^+) reaction on ^{12}C involves the excitation and subsequent decay of $N^*(1710)$, $N^*(1650)$, and $N^*(1720)$ baryonic resonances, leading to the capture of the Λ hyperon in a nuclear orbit while emitting the K^+ particle. By incorporating hyperon bound state spinors derived from the latest quark-meson coupling model, they introduced quark degrees of freedom into the description for the first time. Fixing the coupling constants based on the total and differential cross sections of the elementary $\gamma p \rightarrow \Lambda K^+$ reaction improved parameter constraints. Their study confirmed that the (γ, K^+) reaction is a suitable tool for investigating the spin-flip transitions offering insights into the hypernuclear spectra, albeit with uncertainties due to excluded nucleon intermediate states.

Mart, Tiator, Drechsel, Bennhold, and Ventel focused on the electromagnetic production of the hypertriton, studying the effects of Fermi motion. They derived the two-component form of the elementary production amplitude in a general reference frame [25, 26]. Utilizing the Kaon-MAID [27, 28] model for the elementary amplitude, Mart and Ventel [26] highlighted the significance of Fermi motion effects in describing the cross sections for hypertriton electroproduction. They emphasized that the frozen-proton assumption yields notably different results, particularly at lower energies.

These researchers and their respective works have contributed to advancing our understanding of electromagnetic production of hypernuclei, providing insights into the underlying dynamics and properties of these unique nuclear systems.

1.2 Approaches used to study electroproduction of hypernuclei

In recent times, the study of Λ hypernuclei using spectroscopy has emerged as a valuable tool for exploring the field of strangeness nuclear physics through experimental investigation. The pioneering spectroscopy experiments, conducted in the 1970s using the (π^+, K^+) reaction at the Brookhaven National Laboratory Alternating Gradient Synchrotron (BNL AGS) [29, 30], paved the way for the measurement of excitation spectra of a diverse range of Λ hypernuclei. The experiments were further conducted using the superconducting kaon spectrometer (SKS) at the KEK [31, 32, 33] 12 GeV Proton Synchrotron (PS).

The $(e, e'K^+)$ reaction was used for the first time to study Λ hypernuclear spectroscopy at the Thomas Jefferson National Accelerator Facility (Jefferson Lab) using

the continuous electron beam [34]. This reaction has been further explored through the use of a new high-resolution kaon spectrometer (HKS) installed at Jefferson Lab. At the same time, precision γ-ray spectroscopy has been successfully performed for p-shell Λ hypernuclei at both the KEK 12 GeV PS and the BNL AGS using the germanium detector array known as Hyperball [11]. The results obtained from these experiments have provided quantitative information on the structure of Λ hypernuclei and enabled determination of the strengths of the spin-dependent Λ-nucleon interaction in the p-shell region [35].

In the field of hypernuclear reaction spectroscopy, significant efforts have been made to improve the energy resolution of analyses and find new ways to produce hypernuclei. In recent years, one of the most exciting developments in hypernuclear reaction spectroscopy has been driven by the availability of high-energy and high-intensity electron beams at the Jefferson Lab.

In fact, the first successful experiment on the nuclear target, $^{12}\mathrm{C}(e,e'K^+)^{12}_{\Lambda}\mathrm{B}$ [34, 36], was carried out using these beams. The energy resolution achieved in these experiments, close to 0.5 MeV, is a significant improvement over the best energy resolution achieved so far in the (π^+,K^+) reactions. Following the Hall C experiments with ^{12}C, experimental data at higher virtual-photon energies from Hall A was reported [37, 38, 39].

Before these experiments were completed, theoretical (γ,K^+) spectra were predicted for the ^{10}B, ^{12}C, and ^{16}O targets, and $(e,e'K^+)$ spectra were predicted for the ^{7}Li, ^{9}Be, ^{12}C, and ^{16}O targets. Among these, the prediction for the ^{12}C target was remarkably confirmed by the pioneering experiment. The good agreement between theory and experiment encourages researchers to extend the theoretical framework to the production of heavier hypernuclei beyond the p-shell [15].

In this stage of new developments in hypernuclear spectroscopy it is worth emphasising pioneering experimental proposals made many years ago. One of the priorities was to establish a status of the theoretical attempts to describe the elementary process of the $\gamma p \to K^+\Lambda$ reaction and identify appropriate amplitudes to estimate the hypernuclear production cross sections [19, 20, 27, 40]. The comparison to other reactions such as (K^+,π^+) and (K^-,π^-) is important for further investigation of hypernuclei.

1.3 Properties of interactions with strange particles

The models of kaon and hyperon production that are closely connected to Quantum Chromodynamics (QCD) rely on the quark degrees of freedom. These quark models require a relatively small number of parameters and explicitly consider the spatially-extended structure of baryons, which has been found to be crucial for a reasonable description of photoproduction data [41, 42]. In these models, contributions from baryon resonances in the intermediate state naturally arise from the effects of excited states of the quark system.

Alternatively, other approaches aim to describe the production process at low energies by treating hadrons as effective degrees of freedom. Calculations based on effective Lagrangians, which incorporate interactions among mesons, baryons, and electromagnetic fields, provide a valuable tool for analyzing experimental data. Unlike the quark models, these approaches do not have an explicit connection to QCD. Consequently, the number of parameters in these models is related to the number of resonances considered in the calculations, leading to a relatively large number of parameters in kaon production studies [43, 44, 45].

Certain models incorporate the concept of chiral symmetry to account for the pseudoscalar mesons, which are the Goldstone bosons, in the context of kaon-hyperon photoproduction processes. In the chiral quark model [46], pseudoscalar mesons are included as essential components, utilizing chiral symmetry. Another approach is the gauge-invariant chiral unitary model [47], which constructs a chiral effective meson-baryon Lagrangian to describe the interactions. This model also considers the chiral symmetry. Additionally, attempts have been made to calculate kaon-hyperon photoproduction processes near the threshold using the chiral perturbation theory [48]. In this framework, the interactions are described by an expansion based on chiral symmetry. These different models and approaches involving chiral symmetry provide valuable insights into the dynamics of kaon-hyperon photoproduction and its connection to fundamental symmetries in particle physics.

In the hadrodynamical approach, it is important to consider the coupling between different production channels, which occurs through the meson-baryon interaction in the final state. Therefore, treating these channels simultaneously is necessary to preserve unitarity.

A significant simplification is achieved by neglecting the rescattering effects in the formalism, assuming that their impact on the results is partially accounted for through

effective values of the coupling constants that are fitted to experimental data. This simplifying assumption is commonly adopted in single-channel isobar models, such as the Saclay-Lyon (SL) [19, 20], Kaon-MAID (KM) [27], and Gent-Isobar [43, 44, 45] models. In the single-channel approach, unitarity corrections can be incorporated by introducing energy-dependent widths in the resonance propagators [27, 28].

The isobar models [49] were among the first models capable of accurately describing kaon photoproduction in the resonance region. These models have played a crucial role in understanding the dynamics of kaon production and have achieved good agreement with experimental data by considering the contributions from resonant states. The neglect of rescattering effects simplifies the calculations while maintaining reasonable agreement with experimental observations, highlighting the importance of the effective values of coupling constants and the inclusion of unitarity corrections in the form of energy-dependent widths.

The Regge-plus-resonance (RPR) model, developed by the Gent group [50, 51], offers a description of kaon-hyperon photo- and electroproduction from the threshold up to energies above the resonance region ($E_\gamma \approx 16$ GeV).

In this RPR model, the amplitude is divided into two parts: the Regge-based part and the resonance part. The Regge-based part, characterized by a smooth energy dependence, contributes predominantly to the background in the resonance region. This part of the amplitude provides a systematic and model-independent description of the non-resonant contributions.

The resonance part of the amplitude is responsible for modeling the contributions from nucleon resonances. These resonances are represented by s-channel exchanges, where the intermediate particles are considered as excited states of the nucleon. In the RPR model, these resonant contributions are modified by strong hadron form factors. These form factors ensure that the resonant contributions diminish rapidly above the resonance region, where the Regge-based part dominates.

The advantage of the RPR model is that it reduces the number of background parameters compared to traditional isobar models. This is achieved by utilizing the Regge-based form to describe the smooth background which eliminates the need for introducing a set of the u-channel exchanges. This simplification enhances the model's interpretability and reduces potential uncertainties associated with background parameterization.

Recently new isobar models were developed for the photoproduction [40] and elec-

troproduction [52] of $K\Lambda$. These models employed a consistent and new formalism for describing higher-spin baryon resonances, as introduced by Pascalutsa [53, 54]. This formalism also facilitated the inclusion of hyperon resonances with spin 3/2. Special attention was given to the properties of the model at very forward kaon-angle production, a crucial aspect for calculating cross sections in hypernucleus photo- and electroproduction [16, 55].

1.4 Jefferson Lab Hall A and Hall C experiments

A substantial amount of data has been obtained through two hypernuclear spectroscopy techniques: the reaction-based spectroscopy using the hadron and electron beams and the γ-ray spectroscopy [3, 11].

The reaction spectroscopy directly populates hypernuclear states allowing to explore the level structure of the bound Λ within the bound region. This technique can even investigate the excited states between the nucleon and hyperon emission thresholds. It provides valuable insights into the hypernuclear structure, the binding energies, and the reaction cross sections. Additionally, precise measurements of the production cross sections offer information about the hypernuclear production mechanism and the dynamics of the elementary production reaction.

On the other hand, the γ-ray spectroscopy achieves a very high resolution, typically a few keV, making it a powerful tool for studying the spin-dependent aspects of the effective ΛN interaction. This technique provides precise information on the level structure of hypernuclei and is particularly useful for investigating small spin-flip amplitudes associated with the baryon-baryon interaction. However, the γ-ray spectra can be obtained only up to the nucleon-emission threshold.

Jefferson Lab's Hall A provides an ideal setting for conducting the $(e, e'K^+)$ experiments [56]. The setup involves detecting scattered electrons using the high-resolution spectrometer (HRS) in the electron arm, while coincident kaons are identified in the HRS hadron arm [57]. Although the electromagnetic cross sections are relatively small compared to the hadron-induced reactions, the high beam current, duty cycle, and energy-resolution capabilities help compensate for this drawback. In the experiment E94-107 [56], a coplanar configuration was chosen with the angle between the scattering (leptonic) and reaction (hadronic) planes, which equals to the kaon azimuthal angle, set at $\phi_K = 180°$. Subsequently, the kaon laboratory angle relative to the photon momentum is given by $\theta_K = \theta_{Ke} - \theta_{\gamma e}$. The cross sections were measured at

the virtual photon energy 2.2 GeV and the kaon angle relative to the beam direction $\theta_{Ke} = 6^{\circ}$.

In the Hall C hypernuclear spectroscopy program [58], the experiments aimed at a high resolution, targeting at the full width at the half of the maximum (FWHM) as low as 300-400 keV, while also prioritizing hypernuclear yield rates comparable to those in the (π^+, K^+) reaction. This dual focus is crucial for the success of intensive hypernuclear spectroscopy programs. Across three generations of Hall C experiments, E89-009, E01-011, and E05-115, a virtual photon energy around 1.5 GeV was selected, with the kaon central momentum set at 1.2 GeV/c. The experimental setup evolved from using the superconducting kaon spectrometer in the first generation to the high-resolution large-solid angle QQD spectrometer (HKS) in the subsequent generations.

Progress in the experimental study of bare YN and YY interactions, as well as elementary strangeness production through electromagnetic interaction, forms the foundation of the hypernuclear program at the Jefferson Laboratory.

2 Theoretical background

In this section, we present an essential formalism used in description of the electroproduction of hypernuclei. This formalism was used in our works [5] and [4].

2.1 Cross section

Based on that the electromagnetic interaction is well known and weak, with the coupling constant $\alpha \approx 1/137$, therefore the electroproduction of hypernuclei

$$e(k) + A(P_{\mathrm{A}}) \longrightarrow e'(k') + H(P_{\mathrm{H}}) + K^{+}(P_K)\,, \tag{1}$$

can be treated in the one-photon exchange approximation (OPEA) as depicted in Fig. 2. The production is mediated by a virtual photon γ_v with the momentum $P_\gamma = k - k'$, where k and k' represent the momenta of the incident electron and the scattered electron, respectively.

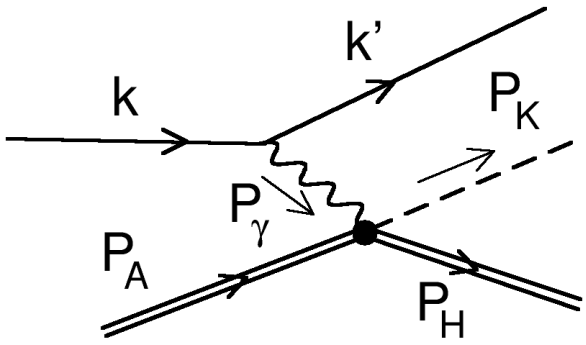

Figure 2: Electroproduction of a hypernucleus in the one-photon exchange approximation. The external particles are on their mass shells but the virtual photon is off-mass-shell, $P_\gamma^2 < 0$.

The formula for the S matrix of the process shown in Fig. 2 and considering the case when the nucleus (A) and hypernucleus (H) are bosons, i.e. they have integer spins is

$$S_{fi} = \delta_{fi} + i(2\pi)^4\,\delta^{(4)}(P_f - P_i)\,\frac{m_e}{\sqrt{8E_e E_{\mathrm{A}} E_{\mathrm{H}} E_K E'_e}}\,M_{fi}\,, \tag{2}$$

where $P_i = k + P_{\mathrm{A}}$ and $P_f = k' + P_K + P_{\mathrm{H}}$. The case with half-integer nuclear spins means the additional factor $\sqrt{4M_{\mathrm{A}}M_{\mathrm{H}}}$. It's important to note that while we describe

the process in the formalism of quantum field theory, the ultimate description of the nuclear and hypernuclear structure will be in a non-relativistic framework using quantum-mechanical wave functions. Consequently, a renormalization of the nuclear current will be necessary.

The invariant amplitude is

$$M_{fi} = (-ie)\,\bar{u}_e(k')\gamma_\mu u_e(k)\,\frac{-i}{{P_\gamma}^2}\,\mathcal{I}^\mu(P_{\rm A}, P_\gamma, P_{\rm H}, P_K)(-ie)\,. \tag{3}$$

Here, the lepton and hadron ($\mathcal{I}^\mu$) currents are gauge invariant. After averaging over the electron and nucleus spins and summing over the final spins we obtain

$$\frac{1}{2(2J_{\rm A}+1)}\sum_{spin}|M_{fi}|^2 = \frac{1}{2(2J_{\rm A}+1)}\,\frac{e^4}{{P_\gamma}^4 m_e^2}\,L_{\mu\nu}W^{\nu\mu}\,, \tag{4}$$

where the lepton and nuclear tensors are, respectively

$$L_{\mu\nu} = \frac{1}{2}\,P_\gamma^2 g_{\mu\nu} + k_\mu k'_\nu + k_\nu k'_\mu \quad \text{and} \quad W^{\nu\mu} = \sum_{J_{\rm A}J_{\rm H}} \mathcal{I}^\nu \mathcal{I}^{\mu+}\,. \tag{5}$$

The nucleus and hypernucleus spins are denoted as $J_{\rm A}$ and $J_{\rm H}$, respectively, m_e is the electron mass, and e the charge unit with $e^2/(4\pi) = \alpha \approx 1/137$.

In the laboratory frame (see Fig. 4), we explicitly express the lepton tensor and evaluate the tensor product

$$\begin{aligned} L_{\mu\nu}\,W^{\nu\mu} = \quad & \frac{Q^2}{2(1-\varepsilon)}\left[W^{xx} + W^{yy} + \varepsilon\,(W^{xx} - W^{yy}) + 2\varepsilon\frac{Q^2}{\omega^2}W^{zz} - \right. \\ & \left. -\sqrt{2\varepsilon(1+\varepsilon)}\sqrt{\frac{Q^2}{\omega^2}}(W^{xz} + W^{zx})\right]\,, \end{aligned} \tag{6}$$

where $Q^2 = -P_\gamma^2$, ω is the photon energy and its transverse polarization is characterized by the parameter

$$\varepsilon \equiv \frac{L_{xx} - L_{yy}}{L_{xx} + L_{yy}} = \left[1 + 2\,\frac{{\vec{P}_\gamma}^{\,2}}{Q^2}\left(\tan\frac{\theta_e}{2}\right)^2\right]^{-1}\,. \tag{7}$$

The cross section, still for specific spin states and A and H as bosons, is

$$d\sigma = \frac{1}{F}\,(2\pi)^4\,\delta^{(4)}(P_f - P_i)\,|M_{fi}|^2\,\frac{m_e^2}{2E'_e E_K E_{\rm H}}\,\frac{d^3k'}{(2\pi)^3}\,\frac{d^3P_K}{(2\pi)^3}\,\frac{d^3P_{\rm H}}{(2\pi)^3}\,, \tag{8}$$

where the initial flux factor in the laboratory frame (lab) reads $F = 4\sqrt{(k\cdot P_{\rm A})^2 - m_e^2 M_{\rm A}^2} = 4M_{\rm A}|\vec{k}|$. Then the lab cross section for A$(e,e'K^+)$H is

$$d\sigma = \frac{m_e^2}{(2\pi)^5 M_{\rm A}|\vec{k}|}\,\delta^{(4)}(P_f - P_i)\,|M_{fi}|^2\,\frac{d^3k'}{2E'_e}\,\frac{d^3P_K}{2E_K}\,\frac{d^3P_{\rm H}}{2E_{\rm H}}\,. \tag{9}$$

In Eqs. (4), (6), and (9) we see that the lepton part of the electroproduction process is described explicitly in the OPEA and the non trivial, yet unknown, dynamics is included in the nuclear tensor which describes a binary process $\mathrm{A}(\gamma_v, K^+)\mathrm{H}$ with $P_f - P_i = P_\mathrm{H} + P_K - P_\mathrm{A} - P_\gamma$. The δ-function in Eq. (9) then allows a decomposition

$$\begin{aligned}\delta^{(4)}(P_\mathrm{H} + P_K - P_\mathrm{A} - P_\gamma) \;&= \int d^4p_p\, d^4p_\Lambda\, \delta^{(4)}(P_K + p_\Lambda - P_\gamma - p_p) \\ &\quad \delta^{(4)}(p_p + p_c - P_\mathrm{A})\, \delta^{(4)}(P_\mathrm{H} - p_c - p_\Lambda)\,, \end{aligned} \tag{10}$$

representing a factorization of kinematics in the impulse approximation (see next subsection). The first δ-function in the integral corresponds to the elementary vertex, while the other two account for the energy-momentum conservation in the nucleus and hypernucleus vertex functions. This decomposition ensures that the elementary amplitude is on its energy-momentum shell.

In equation (9), integration over d^3P_H can be performed using the δ-function, leaving $\delta^{(1)}(E_\mathrm{H} + E_K - M_\mathrm{A} - \omega)$. This is then employed to determine the kaon energy by integrating over $d|\vec{P}_K|$ using the identity $|\vec{P}_K|\, d|\vec{P}_K| = E_K dE_K$. The remaining differentials dE'_e, $d\Omega'_e$, and $d\Omega_K$ are utilized to express the 3-fold differential cross section.

$$\frac{d^3\sigma}{dE'_e\, d\Omega'_E\, d\Omega_K} = \frac{1}{(2\pi)^5}\, \frac{m_e^2 |\vec{P}_K||\vec{k}'|}{8 M_\mathrm{A} E_\mathrm{H} |\vec{k}|}\, |M_{fi}|^2\,, \tag{11}$$

where $d^3P_K = \vec{P}_K^{\,2}\, d|\vec{P}_K|\, d\Omega_K = |\vec{P}_K| E_K dE_K d\Omega_K$ and $d^3k' = |\vec{k}'| E'_e dE'_e d\Omega'_e$. It also holds $P_\mathrm{A} + P_\gamma = P_\mathrm{H} + P_K$.

After summing and averaging over the spins

$$\begin{aligned}\frac{d^3\sigma}{dE'_e\, d\Omega'_E\, d\Omega_K} &= \frac{\alpha^2}{(2\pi)^3}\, \frac{1}{2J_\mathrm{A}+1}\, \frac{1}{Q^2(1-\varepsilon)}\, \frac{|\vec{P}_K||\vec{k}'|}{2M_\mathrm{A} E_\mathrm{H} |\vec{k}|} \Big[\, W^{xx} + W^{yy} \\ &+\varepsilon\,(W^{xx} - W^{yy}) + 2\varepsilon\, \frac{Q^2}{\omega^2}\, W^{zz} - \sqrt{2\varepsilon(1+\varepsilon)}\, \sqrt{\frac{Q^2}{\omega^2}}\, (W^{xz} + W^{zx}) \Big]\,. \end{aligned} \tag{12}$$

The virtual-photon flux factor can be introduced into the formula, considering the ultra-relativistic limit where electron energies are above 1 GeV and the electron mass can be neglected leading to $E_e \approx |\vec{k}|$. Defining

$$\Gamma = \frac{\alpha}{2\pi^2} \frac{|\vec{P}_\gamma|}{Q^2(1-\varepsilon)} \frac{E'_e}{E_e} = \frac{\alpha}{2\pi^2}\, \frac{|\vec{P}_\gamma\,|}{Q^2(1-\varepsilon)}\, \frac{|\vec{k}'|}{|\vec{k}|}\,, \tag{13}$$

we get the expression where a non trivial contribution is given only by the nuclear

tensor

$$\frac{d^3\sigma}{dE'_e\, d\Omega'_E\, d\Omega_K} = \Gamma \frac{1}{2J_{\rm A}+1} \frac{\alpha}{4\pi} \frac{|\vec{P}_K|}{4M_{\rm A}E_{\rm H}|\vec{P}_\gamma|} \frac{1}{2} \Big[W^{xx} + W^{yy} + \varepsilon\,(W^{xx} - W^{yy}) + 2\varepsilon \frac{Q^2}{\omega^2} W^{zz} - \sqrt{2\varepsilon(1+\varepsilon)} \sqrt{\frac{Q^2}{\omega^2}} (W^{xz} + W^{zx}) \Big] . \quad (14)$$

Now we can re-write the 3-fold differential cross section for electroproduction of an unpolarized hypernucleus induced by an unpolarized electron beam and target in terms of following contributions

$$\frac{d^3\sigma}{dE' d\Omega' d\Omega_K} = \Gamma \left(\frac{d\sigma_{\rm T}}{d\Omega_K} + \varepsilon_L \frac{d\sigma_{\rm L}}{d\Omega_K} + \varepsilon \frac{d\sigma_{\rm TT}}{d\Omega_K} + \sqrt{\varepsilon_L(\varepsilon+1)} \frac{d\sigma_{\rm TL}}{d\Omega_K} \right) , \quad (15)$$

where ε and $\varepsilon_{\rm L}$ are the transverse and longitudinal photon polarization parameters, respectively. The relation between them is $\varepsilon_{\rm L} = \varepsilon\, Q^2/\omega^2$.

Functions $d\sigma_{\rm T}$ and $d\sigma_{\rm L}$ describe the cross sections in $\mathrm{A}(\gamma_v, K^+)\mathrm{H}$ for transversally and longitudinally polarized photon beam, respectively. On the other hand, $d\sigma_{\rm TT}$ represents the asymmetry for a transversally polarized photon beam. The final term $d\sigma_{\rm TL}$ accounts for interference effects between the longitudinal and transverse components of the photon beam. It is worth noting that $d\sigma_{\rm T}$ and $d\sigma_{\rm TT}$ are related to the cross section and beam asymmetry, respectively, observed in the production with real photons (photoproduction).

The terms in Eq. (15) are expressed via reduced amplitudes A^{λ}_{Jm} as follows:

$$\frac{d\sigma_{\rm T}}{d\Omega_K} = \frac{\beta}{2\,(2J_A+1)} \sum_{Jm} \frac{1}{2J+1} \left[(A^{+1}_{Jm} + A^{-1}_{Jm}) \right] , \quad (16)$$

$$\frac{d\sigma_{\rm L}}{d\Omega_K} = \frac{\beta}{2J_{\rm A}+1} \sum_{Jm} \frac{1}{2J+1} \left| A^{0}_{Jm} \right|^2 , \quad (17)$$

$$\frac{d\sigma_{\rm TT}}{d\Omega_K} = \frac{\beta}{2J_{\rm A}+1} \sum_{Jm} \frac{1}{2J+1} Re \left[A^{+1}_{Jm} A^{-1*}_{Jm} \right] , \quad (18)$$

$$\frac{d\sigma_{\rm TL}}{d\Omega_K} = \frac{\beta}{2J_{\rm A}+1} \sum_{Jm} \frac{1}{2J+1} Re \left[A^{0*}_{Jm} \left(A^{+1}_{Jm} - A^{-1}_{Jm} \right) \right] . \quad (19)$$

The kinematic factor β [14] is reliant on the kaon momentum. In the kinematic regime under consideration, as observed in previous experiments [56], the dominant component of the cross section is the transverse part $d\sigma_{\rm T}$. Although the longitudinal part $d\sigma_{\rm L}$, makes minor contributions, we will demonstrate its sensitivity to kinematic effects and elementary amplitudes. The interference between the transverse and longitudinal

components $d\sigma_{\rm TL}$, constitutes a significant contribution to the overall cross section, even when dealing with relatively low photon virtualities, such as $Q^2 \approx 0.01(GeV/c)^2$. In the next subsection we will show how the reduced amplitude A^{λ}_{Jm} is calculated.

2.2 Reduced amplitude

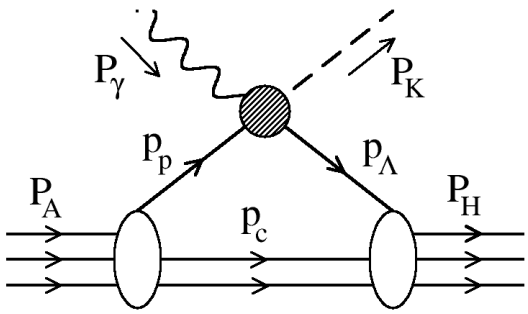

Figure 3: A simplified depiction of the amplitude for the photoproduction (electroproduction) of a hypernucleus (H) caused by real(virtual) photons in the plane-wave impulse approximation (PWIA).

Production of hypernuclei by a virtual photon associated with a kaon in the final state

$$\gamma_v(P_\gamma) + \mathrm{A}(P_\mathrm{A}) \longrightarrow \mathrm{H}(P_\mathrm{H}) + K^+(P_K)\,, \tag{20}$$

can be described in the impulse approximation (IA) where the elementary reaction takes place on individual protons bound in the nucleus. This approach, shown in Fig. 3 is justified for kinematics of the experiments performed at JLab [56] because both photon and kaon momenta are reasonably high, specifically more than 1 GeV. In the IA the total amplitude of the process can be separated into the two-body part, represented by the shaded circle in Fig. 3, and the many-body one, represented by the lower part of the diagram.

The cross section for the production of the ground and excited states of a hypernucleus depends on the many-particle matrix element M_μ between the non-relativistic wave functions of the target nucleus Ψ_A and the hypernucleus Ψ_H

$$M_\mu = \langle \Psi_\mathrm{H} | \langle \chi_K | \sum_{j=1}^{\mathsf{z}} \hat{\mathrm{J}}_\mu(\mathrm{j}) \, | \chi_\gamma \rangle | \Psi_\mathrm{A} \rangle \,, \tag{21}$$

where χ_K is the wave function of the kaon that can be described as a plane wave in PWIA or a distorted wave in DWIA. The wave function χ_γ of a virtual photon, without Coulomb distortion of initial and final electrons, is assumed as a plane wave. $\hat{\mathrm{J}}_\mu(\mathrm{j})$ is an elementary operator for the Λ particle production on the j^{th} nucleon. Utilizing symmetry of the nuclear wave function Ψ_A we can consider that the target proton is the A^{th} particle in the nucleus and replace the sum over the protons with the product $\mathrm{Z}\hat{\mathrm{J}}_\mu$, where Z is the atomic number of the target nucleus. The Λ particle is also taken as the A^{th} particle in the hypernucleus Ψ_H. Then the nucleus and hypernucleus can be taken for particle-core systems where the $(\mathrm{A}-1)$ core nucleons are spectators in the production process with no dynamical response i.e., the structure of the core nucleus is not changed during the process (a weak-coupling scheme). More details on derivation of the matrix element (21) using the Jacobian coordinates ξ_i can be found in the Appendix A. Here we give only basic assumptions.

Assuming translation invariance in the two-body part in Fig. 3, the elementary amplitude can be introduced as $\mathcal{J}_\mu(\vec{P}_K, \vec{P}_\gamma, \vec{p}_p)$

$$\langle \vec{P}_K, \vec{p}_\Lambda \,|\hat{\mathrm{J}}_\mu|\, \tilde{\mathrm{P}_\gamma}, \tilde{\mathrm{p}}_\mathrm{p}\rangle = (2\pi)^3\, \delta^{(3)}(\tilde{\mathrm{p}}_\Lambda - \tilde{\mathrm{p}}_\mathrm{p} - \tilde{\Delta})\, \mathcal{J}_\mu, \tag{22}$$

where $\vec{\Delta} = \vec{P}_\gamma - \vec{P}_K$ is the momentum transfer in the process. This amplitude must be expressed in the two-component form to correspond with the non-relativistic nuclear and hypernuclear wave functions in the many-particle matrix element. Furthermore, this form have to be written for a general two-body reference frame defined by a specific value of the proton momentum. In previous calculations, e.g. in Ref. [56], a special form of the amplitude was used assuming that the target proton is at rest in the laboratory frame ($\vec{p}_p = 0$). A more general form of the amplitude is constructed in section 2.4.

The matrix element (21) is written in terms of a hypernucleus production amplitude as

$$M_\mu = (2\pi)^3 \delta^{(3)}(\vec{P}_\mathrm{A} - \vec{P}_\mathrm{H} + \vec{\Delta})\, \mathcal{T}_\mu\,, \tag{23}$$

where the amplitude reads in the laboratory frame, $\vec{P}_A = 0$ and $\vec{P}_\mathrm{H} = \vec{\Delta}$

$$\begin{aligned} \mathcal{T}_\mu = & Z\, Tr \left[\int \frac{d^3 p_p}{(2\pi)^3}\, \mathcal{J}_\mu(\vec{P}_K, \vec{P}_\gamma, \vec{p}_p) \right. \\ & \times \int d^3 r_\Lambda\, d^3 \xi_p\, \exp\left\{ i \left[\frac{A-1}{A-1+\gamma} \vec{\Delta} \cdot \vec{\xi}_\Lambda + \vec{p}_p \cdot (\vec{\xi}_\Lambda - \vec{\xi}_p) \right] \right\} \\ & \left. \times \int d^3 \xi_1 \ldots d^3\, \xi_{\mathrm{A}-2}\, \Phi_\mathrm{A}(\vec{\xi}_1, \ldots \vec{\xi}_{\mathrm{A}-2}, \vec{\xi}_p)\, \Phi^*_\mathrm{H}(\vec{\xi}_1, \ldots \vec{\xi}_{\mathrm{A}-2}, \vec{\xi}_\Lambda) \right] . \end{aligned} \tag{24}$$

The integral over d^3p_p includes averaging over the Fermi momentum of the target proton since the nucleons are not at rest in nuclei. This averaging makes the calculation quite complicated. However, if dependence of the elementary amplitude on $\vec{p}_p$ is smooth one can consider some specific effective value of the proton momentum, replace $\mathcal{J}_\mu(\vec{P}_K, \vec{P}_\gamma, \vec{p}_p)$ with $\mathcal{J}_\mu(\vec{P}_K, \vec{P}_\gamma, \vec{p}_{\rm eff})$ and take the amplitude out of the integral. Then the integration over $\vec{p}_p$ is trivial giving a δ-function which further allows integration over $\vec{\xi}_p$. From all above we obtain the expression for the hypernucleus production amplitude in the optimum-factorization approximation, which also includes the kaon distortion and which in the lab frame reads

$$\begin{aligned} \mathcal{T}_\mu = Z \cdot \int d^3\xi \; \chi_K^*\left(\vec{p}_K, B\vec{\xi}\,\right) e^{iB\vec{\xi}\cdot(\vec{P_\gamma}-\vec{P_K})} \\ \times \int d^3\xi_1 ... d^3\xi_{\rm A-2} \Phi_{\rm H}^*\left(\vec{\xi_1}...\vec{\xi}_{\rm A-2}, \vec{\xi}\right) \mathcal{J}_\mu(\vec{P}_K, \vec{P}_\gamma, \vec{p}_{\rm eff}) \Phi_{\rm A}\left(\vec{\xi_1}...\vec{\xi}_{\rm A-2}, \vec{\xi}\right) \end{aligned} \tag{25}$$

or

$$\begin{aligned} \mathcal{T}_\mu = Z\, Tr\left[\mathcal{J}_\mu(\vec{P}_K, \vec{P}_\gamma, \vec{p}_{\rm eff}) \int d^3\xi \; e^{iB\,\vec{\Delta}\cdot\vec{\xi}}\, \chi_K^*(\vec{p}_K, B\vec{\xi}\,) \right. \\ \left. \times \int d^3\xi_1 ... d^3\,\xi_{\rm A-2} \Phi_{\rm A}(\vec{\xi}_1, ...\,\vec{\xi}_{\rm A-2}, \vec{\xi}\,)\, \Phi_{\rm H}^*(\vec{\xi}_1, ...\,\vec{\xi}_{\rm A-2}, \vec{\xi}\,)\right], \end{aligned} \tag{26}$$

where $B = (A-1)/(A-1+\gamma)$, $\gamma = m_\Lambda/m_p$, χ_K^* is the kaon distorted wave function, $\vec{p}_K$ is the kaon-hypernucleus relative momentum, and $\vec{\xi} = \vec{\xi}_p = \vec{\xi}_\Lambda$.

Due to gauge invariance of the amplitudes we can set up $\mathcal{T}_\mu\, \varepsilon^\mu \;\to\; \vec{\mathcal{T}} \cdot \vec{\epsilon} \;=\; \sum_\lambda \mathcal{T}_\lambda^{(1)} \epsilon_{-\lambda}$ and $\mathcal{J}_\mu\, \varepsilon^\mu \;\to\; \vec{\mathcal{J}} \cdot \vec{\epsilon} \;=\; \sum_\lambda \mathcal{J}_\lambda^{(1)} \epsilon_{-\lambda}$ with a new polarization vector $\epsilon_\mu \;=\; \varepsilon_\mu - \varepsilon_0 (P_\gamma)_\mu/(P_\gamma)_0 = (\,0,\, \vec{\epsilon}\,)$, where $\lambda = \pm 1, 0$.

Using partial wave decomposition of the product of the photon and kaon wave functions we can separate its orbital dependence

$$\chi_K^*\left(\vec{p}_K, B\vec{\xi}\right) e^{iB\vec{\xi}\cdot\left(\vec{P}_\gamma - \vec{P}_K\right)} = \sum_{LM} F_{LM}\left(\Delta B|\vec{\xi}\,|\right) Y_{LM}\left(\widehat{\xi}\right) , \tag{27}$$

where Y_{LM} is the spherical harmonic function.

The elementary amplitude in the spherical coordinates $\mathcal{J}_\lambda^{(1)}$ can be written in the form

$$\mathcal{J}_\lambda^{(1)} = \sum_{S\eta} \mathcal{F}_{\lambda\eta}^S\, \sigma_\eta^S\,, \tag{28}$$

where $S = 0, 1$, σ_η^1 are the spherical components of Pauli matrices with $\eta = \pm 1, 0$ and σ_0^0 is the unit matrix. The spherical amplitudes $\mathcal{F}_{\lambda 0}^0$ and $\mathcal{F}_{\lambda\eta}^1$ are for the spin non-flip and spin flip transitions, respectively.

The partial wave decomposition and the form of the spherical amplitude (28), enables us to employ the algebra of spherical-tensor operators

$$Y_{LM}(\widehat{\xi})\,\sigma^S_\eta = \sum_{Jm} \mathrm{C}^{Jm}_{LMS\eta}[Y_L(\widehat{\xi})\otimes\sigma^S]^J_m \tag{29}$$

so that Eq. (25) acquires the form

$$\begin{aligned}\mathcal{T}_\lambda = Z\sum_{LM}\sum_{S\zeta}\sum_{Jm} C^{Jm}_{LMS\zeta}\mathcal{F}^S_{\lambda\zeta}\int d^3\xi F_{LM}(B|\vec{\xi}|) \\ \times\int d^3\xi_1...d^3\xi_{\mathrm{A}-2}\Phi^*_{\mathrm{H}}\left(\vec{\xi}_1...\vec{\xi}_{\mathrm{A}-2},\vec{\xi}\right)\left[Y_L(\widehat{\xi})\otimes\sigma^S\right]^J_m\Phi_{\mathrm{A}}(\vec{\xi}_1...\vec{\xi}_{\mathrm{A}-2},\vec{\xi})\end{aligned} \tag{30}$$

where $\mathcal{F}^S_{\lambda\zeta}$ represents the elementary production amplitudes. A more compact form of the hypernuclear production amplitude is:

$$\mathcal{T}_\lambda = Z\sum_{LM}\sum_{S\zeta}\sum_{Jm} C^{Jm}_{LMS\zeta}\mathcal{F}^S_{\lambda\zeta}\left\langle\Phi_{\mathrm{H}}\left|F_{LM}\left[Y_L\otimes\sigma^S\right]^J_m\right|\Phi_{\mathrm{A}}\right\rangle. \tag{31}$$

Then, using the Wigner-Eckart theorem for the nuclear (A) and hypernuclear (H) states we introduce the reduced matrix elements

$$\mathcal{T}_\lambda = Z\sum_{Jm} C^{J_{\mathrm{H}}M_{\mathrm{H}}}_{J_{\mathrm{A}}M_{\mathrm{A}}Jm}\frac{1}{[J_{\mathrm{H}}]}\sum_{S\zeta}\sum_{LM} C^{Jm}_{LMS\zeta}\mathcal{F}^S_{\lambda\zeta}\left(J_{\mathrm{H}}\left\|F_{LM}\left[Y_L\otimes\sigma^S\right]^J\right\|J_{\mathrm{A}}\right). \tag{32}$$

We introduce single-particle states characterized by quantum numbers $|\,\alpha\,\rangle = |\,n\,l\,\frac{1}{2}\,j\,\mu\,\rangle$ generated by the creation operators $|\alpha\rangle = a^+_\alpha\,|\,0\,\rangle$ for a nucleon and $|\alpha'\rangle = b^+_{\alpha'}\,|\,0\,\rangle$ for the Λ. Assuming completeness of the single-particle states, we can express the single-particle operator

$$F_{LM}\left[Y_L\otimes\sigma^S\right]^J_m = \frac{1}{Z}\sum_{\alpha\alpha'}\langle\,\alpha'\,|\,F_{LM}\left[Y_L\otimes\sigma^S\right]^J_m|\,\alpha\,\rangle\;b^+_{\alpha'}\,a_\alpha. \tag{33}$$

The normalization condition is given as $\sum b^+_{\alpha'}a_\alpha = Z$, where Z represents the number of protons since only protons can be converted to Λ particles. It is important to note that we have introduced separate spaces for single-particle states corresponding to the target proton and the final Λ particle. By employing the Wigner-Eckart theorem, we can express the above operator in a specific form.

$$\frac{1}{Z[J]}\sum_{aa'}\left(\,\alpha'\,\|\,F_{LM}\left[Y_L\otimes\sigma^S\right]\,\|\,\alpha\,\right)[b^+_{\alpha'}\otimes a_\alpha]^J_m\,, \tag{34}$$

where $[J] = \sqrt{2J+1}$.

In the summation, we are using notations $\alpha = (n, l, j)$ and $\alpha' = (n', l', j')$, and the reduced matrix element depends solely on these quantum numbers. This decomposition of the one-particle operator enables separation of the reduced many-particle matrix element into the basis of α, α' states.

$$\begin{aligned}(J_{\rm H}|| F_{LM}\left[Y_L \otimes \sigma^S\right] || J_{\rm A}) = \frac{1}{Z[J]} \sum_{aa'} (\alpha' || F_{LM}\left[Y_L \otimes \sigma^S\right] || \alpha) \\ \times (\Phi_{\rm H} || [b^+_{\alpha'} \otimes a_\alpha]^J || \Phi_{\rm A}) .\end{aligned} \tag{35}$$

The second term in the equation represents the one-body density matrix element (OBDME) in the jj coupling scheme. In our actual calculations, the OBDMEs, along with the spherical elementary amplitudes $\mathcal{F}^S_{\lambda\zeta}$, serve as inputs.

To calculate the reduced matrix element of the one-particle operator (35) we employ an explicit form of single-particle wave functions in coordinate space

$$\langle \vec{r} \,|\, \alpha \rangle = \langle \vec{r} \,|\, n\, l\, \frac{1}{2}\, j\, \mu \rangle = R_\alpha(r) \sum_{\nu\eta} \mathcal{C}^{j\mu}_{l\nu\frac{1}{2}\eta} Y_{l\nu}(\hat{r})\, X^{\frac{1}{2}}_\eta \,. \tag{36}$$

Here $R_\alpha(r)$ is the radial part of the wave function and $X^{\frac{1}{2}}_\eta$ is the Pauli spin tensor.

It is important to note that in this context, the vector $\vec{r}$ represents the relative particle-core coordinate which is equivalent to the Jacobi coordinate $\vec{\xi}$. After some certain manipulations, we obtain the following expression

$$\begin{aligned}(\alpha' || F_{LM}\left[Y_L \otimes \sigma^S\right] || \alpha) = \frac{1}{\sqrt{2\pi}} [L][S][J][l][l'][j][j'] \begin{pmatrix} l' & L & l \\ 0 & 0 & 0 \end{pmatrix} \begin{Bmatrix} \frac{1}{2} & \frac{1}{2} & S \\ j' & j & J \\ l' & l & L \end{Bmatrix} \\ \times\ (-1)^{-l'} \int_0^\infty dr\, r^2\, [R_{\alpha'}(r)]^*\, F_{LM}(Br)\, R_\alpha(r) \equiv \mathcal{H}^{LSJ}_{l'j'lj}\, \mathcal{R}^{LM}_{\alpha'\alpha},\end{aligned} \tag{37}$$

where $\mathcal{H}^{LSJ}_{l'j'lj}$ is a Racah structure. The radial integral $\mathcal{R}^{LM}_{\alpha'\alpha}$ comprises the radial components of the single-particle wave functions. Regarding these radial wave functions, we have the flexibility to opt for either a standard harmonic oscillator form or a Woods-Saxon form. The Woods-Saxon form is more realistic as it incorporates a binding energy of the particle, which is obtained from experimental data.

An expression for the spherical component of the complete electroproduction am-

plitude is

$$T^{(1)}_{\lambda} = \sum_{Jm} \mathcal{C}^{J_{\rm H} M_{\rm H}}_{J_{\rm A} M_{\rm A} Jm} \frac{1}{[J_{\rm H} J]} \sum_{S\eta} \mathcal{F}^{S}_{\lambda\eta} \sum_{LM} \mathcal{C}^{Jm}_{LMS\eta} \times \sum_{\alpha'\alpha} \mathcal{R}^{LM}_{\alpha'\alpha} \, \mathcal{H}^{LSJ}_{l'j'lj} \, (\, \Phi_{\rm H} \, || \, [b^{+}_{\alpha'} \otimes a_{\alpha}]^{J} \, || \, \Phi_{\rm A} \,). \tag{38}$$

This equation represents the complete production amplitude, expressed in terms of the spherical elementary amplitudes $\mathcal{F}^{S}_{\lambda\eta}$, the radial integrals $\mathcal{R}^{LM}_{\alpha'\alpha}$ and the OBDME which are essential inputs for the calculations. The radial integral is computed using a selected form of the radial one-particle wave functions for the bound proton and Λ, along with the radial component F_{LM} derived from the decomposed product of the photon and kaon wave functions. The kaon distorted wave function $\chi^{*}_{K}(\vec{p}_{K}, B\vec{\xi}\,)$ used in the DWIA calculations can be obtained through various methods. One approach is to solve the scattering problem for the kaon-hypernucleus system, typically in the eikonal approximation as the momenta are high, see Eq. (70). Another method involves solving the Klein-Gordon equation to calculate the distorted wave function numerically. These approaches provide a suitable description of a kaon wave function distorted by the interaction between the kaon and hypernucleus. More details on the radial integrals will be given in subsection 2.5.

The reduced amplitude used in Eqs. (16)-(19) then reads

$$A^{\lambda}_{Jm} = \frac{1}{[J]} \sum_{S\eta} \mathcal{F}^{S}_{\lambda\eta} \sum_{LM} \mathsf{C}^{Jm}_{LMS\eta} \sum_{\alpha'\alpha} \mathcal{R}^{LM}_{\alpha'\alpha} \, \mathcal{H}^{LSJ}_{l'j'lj} \times (\, \Phi_{\rm H} \, || \, [b^{+}_{\alpha'} \otimes a_{\alpha}]^{J} \, || \, \Phi_{\rm A} \,) \, . \tag{39}$$

2.3 Kinematics

The electroproduction of hypernuclei is experimentally investigated in lab frame with the target nucleus at rest, $\vec{P}_{\rm A} = 0$, as it is depicted in Fig. 4. The $\hat{z}$ axis of the right-handed coordinate system is oriented along the photon momentum $\vec{P}_{\gamma}$, which lies in the "Scattering plane", and the $\hat{y}$ axis is perpendicular to this plane. The kaon momentum, which lies in the "Reaction plane" is determined by its polar, θ_K, and azimuthal, Φ_K, angle. Our convention is such that in the case of the coplanar kinematics, $\Phi_K = 0$, the kaon momentum lies in between the momenta of the beam

($\vec{k}$) and photon ($\vec{P}_\gamma$). See also Fig. 5 for the analogous coplanar case with $\Phi_K = 180°$.

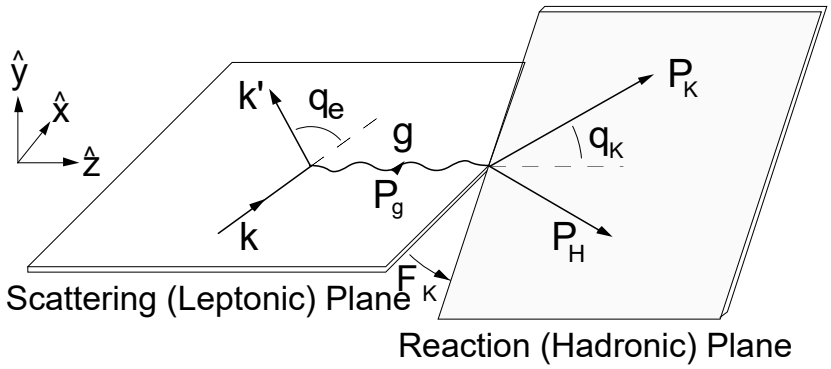

Figure 4: Kinematics in electroproduction of hypernuclei in lab frame. The reaction is considered in the one-photon exchange approximation.

An experiment on electroproduction can be described with kinematical quantities such as the energy of the initial electron E_e(the beam energy), the energy and angle of the scattered electron, E'_e and θ_e, and the polar, θ_K, and azimuthal, Φ_K, angle of the kaon, see Fig. 4. In the one-photon exchange approximation, the hypernucleus production is mediated by a virtual photon with the energy and momentum determined by the electron kinematics. As this photon is off its mass shell, it has a non-zero "mass" defined as $Q^2 = -P_\gamma^2 = \vec{P}_\gamma^{\,2} - E_\gamma^2$ and $Q^2 > 0$. The other participating particles are assumed on their mass shells.

In the impulse approximation the elementary-production process proceeds in the nuclear medium where the Λ and initial proton are not free particles anymore. In fact, they are indeed intermediate (virtual) particles as depicted in Fig. 3, but within the framework of the non-relativistic nuclear physics used here, we assume that they are still on their mass shells. We also require the translational invariance of the elementary and total amplitudes, as well as of the nuclear and hypernuclear wave functions. These wave functions are taken as a product of the plane wave for the center of inertia and the internal part expressed as a function of relative (Jacobi) coordinates.

The 3-momentum conservation in each vertex in Fig. 3 is

$$\vec{P}_\gamma + \vec{p}_p = \vec{P}_K + \vec{p}_\Lambda\,, \qquad \vec{P}_{\rm A} = \vec{p}_{\rm c} + \vec{p}_p\,, \qquad \vec{P}_{\rm H} = \vec{p}_{\rm c} + \vec{p}_\Lambda\,, \tag{40}$$

where $\vec{p}_{\rm c}$ is a momentum of the "core" nucleus. These relations provide the 3-

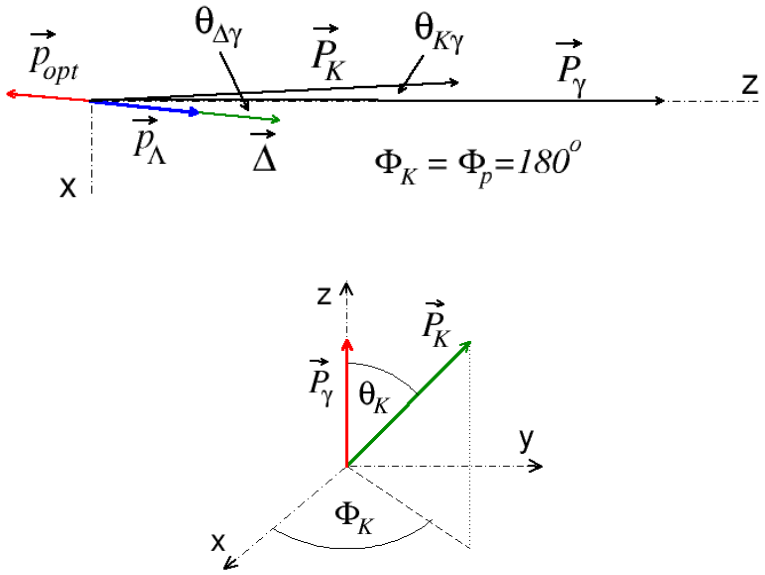

Figure 5: Coplanar kinematics ($\Phi_K = 180°$) for a non zero proton momentum with $\theta_{\Delta p} = 180°$. In the bottom panel, the kaon momentum in the lab frame is depicted.

momentum conservation in the entire many-body system

$$\vec{P}_\gamma + \vec{P}_{\rm A} = \vec{P}_K + \vec{P}_{\rm H}\,. \tag{41}$$

The energy conservation in the elementary vertex is

$$E_\gamma + \sqrt{m_p^2 + \vec{p}_p^{\,2}} = E_K + \sqrt{m_\Lambda^2 + \vec{p}_\Lambda^{\,2}}\,, \tag{42}$$

which together with the 3-momentum conservation means that the elementary amplitude is on energy-momentum shell and that the amplitude constructed in the free space can be used in the calculation. Energy conservation in the many-body vertices are

$$E_{\rm A} = \sqrt{M_{\rm c}^2 + (\vec{P}_{\rm A} - \vec{p}_p)^2} + \sqrt{m_p^2 + \vec{p}_p^{\,2}} + \epsilon_p\,, \tag{43}$$

$$E_{\rm H} = \sqrt{M_{\rm c}^2 + (\vec{P}_{\rm A} - \vec{p}_p)^2} + \sqrt{m_\Lambda^2 + \vec{p}_\Lambda^{\,2}} + \epsilon_\Lambda\,, \tag{44}$$

where $M_{\rm c}$ is the mass of the core nucleus and the binding energies ϵ_p and ϵ_Λ are introduced because the proton and Λ are bound in the nucleus and hypernucleus, respectively. Unfortunately, these binding energies together with the energy conservation in the elementary vertex lead to a violation of the energy conservation in the

reaction

$$E_\gamma + E_{\rm A} = E_K + E_{\rm H} + (\epsilon_p - \epsilon_\Lambda)\,. \tag{45}$$

Note however, that the additional factor is relatively small, $(\epsilon_p - \epsilon_\Lambda) \approx 10$ MeV, in comparison with the total energy, $E_\gamma + E_{\rm A} \approx 10$ GeV, and therefore an effect of energy violation is expected to be quite small, typically below 1%.

As we require that the total energy conservation has the ordinary form,

$$E_\gamma + E_{\rm A} = E_K + E_{\rm H}\,, \tag{46}$$

there are two possibilities how to solve the situation. The first one is to neglect the difference of binding energies at all, assuming $\epsilon_p - \epsilon_\Lambda = 0$ and use the on-shell elementary amplitude. The other choice is to permit an energy violation in the elementary vertex

$$E_\gamma + \sqrt{m_p^2 + \vec{p}_p^{\,2}} = E_K + \sqrt{m_\Lambda^2 + \vec{p}_\Lambda^{\,2}} + (\epsilon_\Lambda - \epsilon_p)\,, \tag{47}$$

which requires that the amplitude is calculated off energy shell. However, as this off shell extension of the elementary amplitude would require additional assumptions which are not unique, we do not consider this possibility. In the calculations we therefore consider the standard energy conservation both in the elementary and many-body systems. Note that in the previous calculations [56], the binding effects due to $\epsilon_p - \epsilon_\Lambda$ were also neglected.

The magnitude of the kaon momentum $|\vec{P}_K|$ needs to be established from the energy conservation either in the elementary (two-body) system

$$E_\gamma + \sqrt{m_p^2 + \vec{p}_p^{\,2}} = \sqrt{m_K^2 + \vec{P}_K^{\,2}} + \sqrt{m_\Lambda^2 + (\vec{P}_\gamma + \vec{p}_p - \vec{P}_K)^2}\,, \tag{48}$$

or in the many-body system, written in the lab frame as

$$E_\gamma + M_{\rm A} = \sqrt{m_K^2 + \vec{P}_K^{\,2}} + \sqrt{M_{\rm H}^2 + (\vec{P}_\gamma - \vec{P}_K)^2}\,. \tag{49}$$

It is evident that due to the proton-momentum dependence in Eq. 48, these equations cannot be solved simultaneously for a general value of the proton momentum. The previous calculations, e.g. in Ref. [56] done in the frozen-proton approximation with $\vec{p}_p = 0$, were performed with two different values of $|\vec{P}_K|$ calculated from Eqs. (48) and (49). However, these equations can provide the same solution for $|\vec{P}_K|$ assuming a special value of the proton momentum which we denote as the optimum momentum $\vec{p}_{\rm opt}$. This momentum is obtained from Eq. (48) using $|\vec{P}_K|$ calculated from Eq. (49)

$$E_\gamma - \sqrt{m_K^2 + \vec{P}_K^{\,2}} = \sqrt{m_\Lambda^2 + (\vec{\Delta} + \vec{p}_{\rm opt})^2} - \sqrt{m_p^2 + \vec{p}_{\rm opt}^{\,2}} = \sqrt{M_{\rm H}^2 + \vec{\Delta}^{\,2}} - M_{\rm A}\,, \tag{50}$$

where $\vec{\Delta}$ is the momentum transfer in the reaction, $\vec{\Delta} = \vec{P}_\gamma - \vec{P}_K$. One can see that the value of $|\vec{p}_{\rm opt}|$ is not uniquely determined as Eq. (50) depends also on the proton angle with respect to $\vec{\Delta}$ which can be chosen in the calculation, see Fig. 5 for the choice $\theta_{\Delta p} = 180^\circ$.

For a given angle $\theta_{\Delta p}$ the proton polar angle with respect to the photon (see Fig. 5) can be calculated using

$$\vec{P_\gamma} \cdot \vec{p_p} = \vec{\Delta} \cdot \vec{p_p} + \vec{P}_K \cdot \vec{p_p} \tag{51}$$

and

$$\vec{P}_K \cdot \vec{p_p} = |\vec{P}_K||\vec{p_p}|(\sin\theta_p \sin\theta_K \cos(\Phi_p - \Phi_K) + \cos\theta_p \cos\theta_K)\,, \tag{52}$$

which give the expression for the proton polar angle

$$\begin{aligned}\cos\theta_p = &\Big[|\vec{\Delta}|\cos\theta_{\Delta p}\left(|\vec{P_\gamma}| - |\vec{P}_K|\cos\theta_K\right) \pm \left(|\vec{P}_K|\sin\theta_K\cos(\Phi_p - \Phi_K)\right) \\ &\times\sqrt{(|\vec{P_\gamma}| - |\vec{P}_K|\cos\theta_K)^2 - (|\vec{\Delta}|\cos\theta_{\Delta p})^2 + (|\vec{P}_K|\sin\theta_K\cos(\Phi_p - \Phi_K))^2}\Big] \\ &\times\left((|\vec{P_\gamma}| - |\vec{P}_K|\cos\theta_K)^2 + (|\vec{P}_K|\sin\theta_K\cos(\Phi_p - \Phi_K))^2\right)^{-1}\,.\end{aligned} \tag{53}$$

The negative sign is used for $\theta_{\Delta p} > 60^\circ$ where we will get a physical value of the proton momentum. The angle θ_p still depends on the proton azimuthal angle Φ_p which can be chosen. In our calculations we chose $\theta_{\Delta p} = 180^\circ$ and $\Phi_p = 180^\circ$, but we will also show the dependence of the cross sections on $\theta_{\Delta p}$.

2.4 Elementary amplitude

In this subsection we present a two-component form of the elementary amplitude for the electrodroduction of K^+ on a proton induced by a virtual photon. This formalism can be also used for electroproduction of other pseudo-scalar mesons. The invariant amplitude of the process

$$\gamma_\nu(P_\gamma, \varepsilon) + p(p_p, \xi_p) \to \Lambda(p_\Lambda, \xi_\Lambda) + K^+(P_K)\,, \tag{54}$$

where the momenta, spin-projections and polarizations of involved particles are given in the parentheses, can be expressed using six Lorentz and gauge invariant operators M_j^μ multiplied by the Dirac bispinors $u(p, \xi)$ for the baryon fields

$$\mathcal{M}^\mu \varepsilon_\mu = \sum_{j=1}^{6} \bar{u}(p_\Lambda, \xi_\Lambda)\,\gamma_5\, M_j^\mu\, \varepsilon_\mu u(p_p, \xi_p)\, A_j(s,t)\,. \tag{55}$$

In the one-photon exchange approximation, the electron part enters as the four-vector $\varepsilon_\mu = -e\ \bar{u}(p'_e)\,\gamma_\mu u(p_e)\,/Q^2$ where $u(p_e)$ is the Dirac bispinor for the electron. The scalar amplitudes A_j in (55) are functions of the Mandelstam variables $s = (P_\gamma + p_p)^2$ and $t = (P_\gamma - P_K)^2$ and describe dynamics of the production. They can be obtained e.g., from the decomposition of Feynamm diagrams contributing to the process [52].

The gauge invariant operators can be rewritten as

$$\begin{aligned}
M_1^\mu &= \frac{1}{2}[(\gamma\cdot P_\gamma)\,\gamma^\mu - \gamma^\mu(\gamma\cdot P_\gamma)]\,,\\
M_2^\mu &= p_p^\mu - \frac{1}{P_\gamma^2}(P_\gamma\cdot p_p)\,P_\gamma^\mu\,,\\
M_3^\mu &= p_\Lambda^\mu - \frac{1}{P_\gamma^2}(P_\gamma\cdot p_\Lambda)\,P_\gamma^\mu\,,\\
M_4^\mu &= \gamma^\mu(P_\gamma\cdot p_p) - (\gamma\cdot P_\gamma)\,p_p^\mu\,,\\
M_5^\mu &= \gamma^\mu(P_\gamma\cdot p_\Lambda) - (\gamma\cdot P_\gamma)\,p_\Lambda^\mu\,,\\
M_6^\mu &= (\gamma\cdot P_\gamma)\,P_\gamma^\mu - \gamma^\mu P_\gamma^2\,.
\end{aligned} \tag{56}$$

and they fulfill the Ward identity $\mathcal{M}_j^\mu \cdot (P_\gamma)_\mu = 0$.

The invariant amplitude (55) can be used to calculate observable quantities of the elementary process in any reference frame but this form of the $\mathcal{M}^\mu$ cannot be directly used to calculate the many-particle matrix element (21), which is considered in the non relativistic formalism. For computing this matrix element, we need to construct a one-body transition operator on the non relativistic proton-hyperon Hilbert space. This transition operator is written in the two-component formalism using Pauli matrices which can fold with the Pauli spinors in the non relativistic wave functions of the nucleus and hypernucleus.

A special case of the two-component form of the amplitude, written in the laboratory and centre-of-mass frame in terms of the so called Chew-Goldberger-Low-Nambu (CGLN) amplitudes, can be found in Ref. [14]. This CGLN form in the laboratory frame was used in previous calculations [56] assuming the frozen proton approximation, i.e. the effective proton momentum was zero in Eqs. (25) and (26) ($\vec{p}_{\rm eff} = 0$). A novel feature of our approach is that we have constructed the elementary amplitude which can be used with a non-zero proton momentum $\vec{p}_{\rm eff}$. This more general amplitude allows to go beyond the frozen proton approximation and, partially, to account for the Fermi motion effects due to the proton motion in the nucleus.

The gauge invariance enables re-writing the invariant amplitude into a form that is still covariant but includes non relativistic structures composed of Pauli matrices and

three-vectors – the photon polarization vector and the momenta of the photon, proton and kaon. Particularly, the gauge invariance facilitates using a new polarization vector $\epsilon_\mu = \varepsilon_\mu - \varepsilon_0\,(P_\gamma)_\mu/(P_\gamma)_0 = (\,0,\,\vec{\epsilon}\,)$ which sets the time component to zero. Note that the Ward identity, with the new polarization vector remains valid as guaranteed by the definition of ϵ_μ which becomes zero after the formal replacement $\varepsilon_\mu \to (P_\gamma)_\mu$. Then it allows to write the amplitude in a non-relativistic-like two-component form

$$\mathcal{M}\cdot\varepsilon = \overline{u}_\Lambda\gamma_5\left(\sum_{j=1}^{6} M_j\cdot\varepsilon\,A_j\right)u_p = X_\Lambda^+\;(\vec{J}\cdot\vec{\epsilon}\,)\;\;X_p\,, \tag{57}$$

where ${X_\Lambda}^+$ and X_p are Pauli spinors and $\overline{u}_\Lambda$ and u_p are Dirac bispinors for the Λ and proton particles, respectively.

The invariant amplitude on the left-hand part of Eq. (57) includes covariant structures composed of Dirac bispinors and γ matrices

$$\begin{aligned}
\mathcal{M}\cdot\varepsilon = \overline{u}_\Lambda\gamma_5\,u_p\Bigg[&\left((p_p\cdot\varepsilon) - \frac{(P_\gamma\cdot p_p)(P_\gamma\cdot\varepsilon)}{P_\gamma^2}\right)A_2\\
&+\left((p_\Lambda\cdot\varepsilon) - \frac{(P_\gamma\cdot p_\Lambda)(P_\gamma\cdot\varepsilon)}{P_\gamma^2}\right)A_3 - (P_\gamma\cdot\varepsilon)A_1\Bigg]\\
&+\overline{u}_\Lambda\gamma_5(\gamma\cdot\varepsilon)\,u_p\left[(P_\gamma\cdot p_p)A_4 + (P_\gamma\cdot p_\Lambda)A_5 - P_\gamma^2 A_6\right]\\
&-\overline{u}_\Lambda\gamma_5(\gamma\cdot P_\gamma)\,u_p\left[(p_p\cdot\varepsilon)A_4 + (p_\Lambda\cdot\varepsilon)A_5 - (P_\gamma\cdot\varepsilon)A_6\right]\\
&+\overline{u}_\Lambda\gamma_5(\gamma\cdot P_\gamma)(\gamma\cdot\varepsilon)\,u_p\,A_1\,,
\end{aligned} \tag{58}$$

that can be expressed via Pauli matrices. Here the photon polarization appears only via gauge-invariant combinations $\varepsilon_\mu - P_{\gamma_\mu}(P_\gamma\cdot\varepsilon)/P_\gamma^2$, $P_{\gamma_\mu}\varepsilon_\nu - \varepsilon_\mu P_{\gamma_\nu}$, and $\vec{P_\gamma}\times\vec{\varepsilon}$.

The structure of the first term in Eq. (58) is

$$\begin{aligned}
\overline{u}_\Lambda(p_\Lambda,\xi_\Lambda)\,\gamma_5\,u_p(p_p,\xi_p) &= \sqrt{\frac{(E_\Lambda+m_\Lambda)(E_p+m_p)}{4m_\Lambda m_p}}\\
&\times\;\mathsf{X}_\Lambda^+\left(\mathbf{1},\;\frac{\vec{\sigma}\cdot\vec{p}_\Lambda}{E_\Lambda+m_\Lambda}\right)\begin{pmatrix}0 & \mathbf{1}\\ -\mathbf{1} & 0\end{pmatrix}\begin{pmatrix}\mathbf{1}\\ \frac{1}{E_p+m_p}\vec{\sigma}\cdot\vec{p}_p\end{pmatrix}X_p =\\
&= \sqrt{\frac{(E_\Lambda+m_\Lambda)(E_p+m_p)}{4m_\Lambda m_p}}\;\mathsf{X}_\Lambda^+\left(\frac{\vec{\sigma}\cdot\vec{p}_p}{E_p+m_p} - \frac{\vec{\sigma}\cdot\vec{p}_\Lambda}{E_\Lambda+m_\Lambda}\right)X_p\,.
\end{aligned} \tag{59}$$

The second and third term in (58) with the notation $a_\mu = \varepsilon_\mu$ and $(P_\gamma)_\mu$, respectively,

give us

$$\overline{u}_\Lambda(p_\Lambda,\xi_\Lambda)\,\gamma_5(\gamma\cdot a)\;u_p(p_p,\xi_p) = \\ = \sqrt{\frac{(E_\Lambda+m_\Lambda)(E_p+m_p)}{4m_\Lambda m_p}}\;X^+_\Lambda\left\{-a_0\left(\frac{\vec\sigma\cdot\vec p_p}{E_p+m_p}+\frac{\vec\sigma\cdot\vec p_\Lambda}{E_\Lambda+m_\Lambda}\right)+\vec\sigma\cdot\vec a+ \right. \\ \frac{1}{(E_\Lambda+m_\Lambda)(E_p+m_p)}\Big[\,(\vec\sigma\cdot\vec p_\Lambda)(\vec p_p\cdot\vec a)+(\vec\sigma\cdot\vec p_p)(\vec p_\Lambda\cdot\vec a)-(\vec\sigma\cdot\vec a)(\vec p_\Lambda\cdot\vec p_p)- \\ \left. i\,\vec p_\Lambda\times\vec p_p\cdot\vec a\,\Big]\right\}X_p\,, \tag{60}$$

For practical calculations, it is more convenient to express the amplitude using the photon P_γ, proton p_p, and kaon momenta P_K instead of the Λ momentum p_Λ because the kaon momentum is measured in experiment. From momentum conservation, we have $p_\Lambda = P_\gamma + p_p - P_K$. So, we can obtain the elementary production amplitude in the two-component form with an arbitrary value of the proton momentum

$$\begin{aligned}\vec J\cdot\vec\epsilon = {}& G_1\,(\vec\sigma\cdot\vec\epsilon\,)+G_2\,i(\vec p_p\times\vec P_\gamma\cdot\vec\epsilon\,)+G_3\,i(\vec P_K\times\vec P_\gamma\cdot\vec\epsilon\,)+\\ &+G_4\,i(\vec p_p\times\vec P_K\cdot\vec\epsilon\,)+\;i(\vec p_p\times\vec P_K\cdot\vec P_\gamma\,)\;\Big[\,G_5\,(\vec P_\gamma\cdot\vec\epsilon\,)+G_6\,(\vec p_p\cdot\vec\epsilon\,)+\\ &+G_7\,(\vec P_K\cdot\vec\epsilon\,)\,\Big]+G_8\,(\vec\sigma\cdot\vec P_\gamma\,)(\vec P_\gamma\cdot\vec\epsilon\,)+G_9\,(\vec\sigma\cdot\vec P_\gamma\,)(\vec p_p\cdot\vec\epsilon\,)+\\ &+G_{10}\,(\vec\sigma\cdot\vec P_\gamma\,)(\vec P_K\cdot\vec\epsilon\,)+G_{11}\,(\vec\sigma\cdot\vec p_p)(\vec P_\gamma\cdot\vec\epsilon\,)+G_{12}\,(\vec\sigma\cdot\vec p_p)(\vec p_p\cdot\vec\epsilon\,)+\\ &+G_{13}\,(\vec\sigma\cdot\vec p_p)(\vec P_K\cdot\vec\epsilon\,)+G_{14}\,(\vec\sigma\cdot\vec P_K)(\vec P_\gamma\cdot\vec\epsilon\,)+G_{15}\,(\vec\sigma\cdot\vec P_K)(\vec p_p\cdot\vec\epsilon\,)+\\ &+G_{16}\,(\vec\sigma\cdot\vec P_K)(\vec P_K\cdot\vec\epsilon\,)\,.\end{aligned} \tag{61}$$

Formulas for the CGLN-like amplitudes G_j expressed in terms of scalar amplitudes A_j and kinematical variables are given in Appendix B. There are 16 amplitudes G_j but not all of them are independent. These CGLN-like amplitudes are suitable to specify the entire elementary amplitude in a non relativistic calculations. One can check the general formula (61) comparing it for a special case with that in Ref. [14]. Indeed, in lab frame ($\vec p_p = 0$) the general form (61) reduces to only six terms

$$\begin{aligned}\vec J_{LAB}\cdot\vec\epsilon\;\;=\;\;& G_1\,(\vec\sigma\cdot\vec\epsilon\,)+G_3\,i(\vec P_K\times\vec P_\gamma\cdot\vec\epsilon\,)+G_8\,(\vec\sigma\cdot\vec P_\gamma\,)(\vec P_\gamma\cdot\vec\epsilon\,)+\\ &G_{10}\,(\vec\sigma\cdot\vec P_\gamma\,)(\vec P_K\cdot\vec\epsilon\,)+G_{14}\,(\vec\sigma\cdot\vec P_K)(\vec P_\gamma\cdot\vec\epsilon\,)+\\ &G_{16}\,(\vec\sigma\cdot\vec P_K)(\vec P_K\cdot\vec\epsilon\,)\,,\end{aligned} \tag{62}$$

which coincides with the expression in Ref. [14]. Also the formulas for G_j agree with the corresponding formulas for F_i ($i = 1, ..., 6$) in [14]. Similarly for the case of the center-of-mass frame ($\vec p_p = -\vec P_\gamma$), the expression and the corresponding CGLN-like amplitudes in Appendix B (61) can be compared with those in Ref. [14] .

In some calculations, especially in our case of evaluating the matrix element in Eq. (21), it is convenient to use the amplitude in the spherical coordinates. Then the scalar product can be expressed as:

$$\vec{J}\cdot\vec{\epsilon}=-\sqrt{3}\,[\,J^{(1)}\otimes\epsilon^{(1)}\,]^0=-\sqrt{3}\,\mathcal{C}^{00}_{1\lambda1-\lambda}J^{(1)}_{\lambda}\epsilon^{(1)}_{-\lambda}=\sum_{\lambda=\pm1,0}(-1)^{-\lambda}\,J^{(1)}_{\lambda}\epsilon^{(1)}_{-\lambda}\,. \tag{63}$$

The spherical components of $J^{(1)}$ can be defined via 12 spherical amplitudes $F^S_{\lambda\xi}$ with $S=0,1$ and $\lambda,\xi=\pm1,0$.

$$J^{(1)}_{\lambda}=\sum_{\lambda,\xi}\mathcal{F}^S_{\lambda\xi}\,\sigma^S_{\xi}\,, \tag{64}$$

where σ^1_η are the spherical components of the Pauli matrices and σ^0 is the unit matrix (see Appendix). Inserting Eq. (64) into (63) we get the following decomposition of the elementary amplitude

$$\begin{aligned}\vec{J}\cdot\vec{\epsilon}=\;&-\;\epsilon_{\,1}^{\,1}\,(\,\mathcal{F}^{\,0}_{-10}+\sigma^1_{\,1}\,\mathcal{F}^{\,1}_{-11}+\sigma^1_{\,0}\,\mathcal{F}^{\,1}_{-10}+\sigma^1_{-1}\,\mathcal{F}^{\,1}_{-1-1}\,)+\\&+\;\epsilon_{\,0}^{\,1}\,(\,\mathcal{F}^{\,0}_{00}\;+\sigma^1_{\,1}\,\mathcal{F}^{\,1}_{01}\;+\sigma^1_{\,0}\,\mathcal{F}^{\,1}_{00}\;+\sigma^1_{-1}\,\mathcal{F}^{\,1}_{0-1}\,)-\\&-\;\epsilon_{-1}^{\,1}\,(\,\mathcal{F}^{\,0}_{10}\;+\sigma^1_{\,1}\,\mathcal{F}^{\,1}_{11}\;+\sigma^1_{\,0}\,\mathcal{F}^{\,1}_{10}\;+\sigma^1_{-1}\,\mathcal{F}^{\,1}_{1-1}\,)\,.\end{aligned} \tag{65}$$

The formulas for $F^S_{\lambda\xi}$ expressed through the spherical components of the momenta and the CGLN-like amplitudes G_j are given in Appendix C.

2.5 Radial integral

In this subsection we discuss in detail the radial integral used in Eq. (39). It is calculated in the plane wave impulse approximation and the distorted wave impulse approximation.

Neglecting the kaon re-scattering on the hypernucleus in the PWIA, the product of the initial photon and final kaon plane waves can be decomposed into the partial waves as

$$\begin{aligned}\chi_\gamma\,(\vec{r}\,)\,\chi_k^{(-)}\,(\vec{r}\,)&=e^{iB\vec{\Delta}\cdot\vec{r}}\\&=4\pi\sum_{LM}i^L j_L\,(\Delta Br)\,Y^*_{LM}\left(\widehat{\Delta}\right)Y_{LM}\,(\widehat{r})\\&=\sum_{LM}F_{LM}\,(\Delta Br)\,Y_{LM}\,(\widehat{r})\end{aligned} \tag{66}$$

where $B=(A-1)/(A-1+\gamma)$ and $\gamma=m_\Lambda/m_p$ with the Λ and proton masses. Y_{LM} are the spherical harmonic functions and F_{LM} is a projected wave that can be

expressed as

$$
\begin{aligned}
F_{LM}\left(\Delta Br\right) &= \int d\widehat{r}\, Y_{LM}^{*}\left(\widehat{r}\right) e^{iB\overrightarrow{\Delta}\cdot\overrightarrow{r}} \\
&= \int d\widehat{r}\, Y_{LM}^{*}\left(\widehat{r}\right)\cdot 4\pi \sum_{L'M'} i^{L'} j_{L'}\left(\Delta Br\right) Y_{L'M'}^{*}\left(\widehat{\Delta}\right) Y_{L'M'}\left(\widehat{r}\right) \\
&= 4\pi\, i^{L} j_{L}\left(\Delta Br\right) Y_{LM}^{*}\left(\widehat{\Delta}\right), \qquad (67)
\end{aligned}
$$

where $j_L\left(\Delta Br\right)$ is the spherical Bessel function. Then the radial integral in PWIA that can be used in calculations of the reduced amplitude (39) is

$$
R_{\alpha'\alpha}^{LM} = \int_0^{\infty} dr r^2 R_{\alpha'}^{*}\left(r\right) F_{LM}\left(\Delta Br\right) R_{\alpha}\left(r\right), \qquad (68)
$$

where $R_{\alpha'}^{*}(r)$ and $R_{\alpha}(r)$ are the radial wave functions of the Λ and proton, respectively. The function F_{LM} is given in Eq. (67).

A more interesting and realistic case is when we include the kaon distortion in the radial integral in DWIA. Then the projected wave $F_{LM}(\Delta B\xi)$ is determined from

$$
e^{iB\vec{\Delta}\cdot\vec{\xi}}\,\chi_K^{(-)*}(\vec{p}_K, B\vec{\xi}\,) = \sum_{LM} F_{LM}(\Delta B\xi)\, Y_{LM}(\hat{\xi}), \qquad (69)
$$

where χ_K^{*} stands for the kaon distorted wave which is not present in PWIA as $\chi_K^{*}=1$ in this case. In the case of DWIA, χ_K^{*} is calculated in eikonal approximation [64] assuming the first-order optical potential

$$
\chi_K^{(-)*}\left(\overrightarrow{p_K}, B\overrightarrow{\xi}\right) = \exp\left\{-a\sigma_{tot}\frac{1-i\alpha}{2}\int_0^{\infty} dt\rho\left(B\overrightarrow{\xi}+\widehat{p_K}t\right)\right\}, \qquad (70)
$$

where $\alpha = \mathrm{Re}f(0)/\mathrm{Im}f(0)$ and $f(0)$ is the forward-angle amplitude of the kaon-nucleon scattering. σ_{tot} is the kaon-nucleon total cross section, $\vec{p}_K$ is the kaon momentum with respect to the hypernucleus, and a is a kinematical factor

$$
a = \frac{\left|\overrightarrow{k_K}\right|}{\left|\overrightarrow{p_K}\right|}\frac{\varepsilon_K\left(p_K\right)+\frac{p_K^2}{2M_{\mathrm{A}}}}{\varepsilon_K\left(p_K\right)\cdot\varepsilon_N\left(p_K/\mathrm{A}\right)}\left[\frac{s}{\left(1+\frac{\varepsilon_K}{M_{\mathrm{A}}}+\frac{p_K^2}{4M_{\mathrm{A}}^2}\right)\left(1+\frac{\varepsilon_K}{M_{\mathrm{A}}}\right)+\frac{p_k^2}{2M_{\mathrm{A}}^2}}\right]^{\frac{1}{2}}. \qquad (71)
$$

In this equation, $\varepsilon_x\left(y\right)=\sqrt{m_x^2+y^2}$ with $x=K$ and N, are the kaon and nucleon energies calculated with the momenta $y=\vec{p}_K$ and $\vec{p}_K/\mathrm{A}$, respectively. The kaon momentum $\vec{k}_K$ is computed with respect to the nucleon and the invariant kaon-nucleon energy is $\sqrt{s}=\varepsilon_K\left(k_K\right)+\varepsilon_N\left(k_K\right)$. It is important to note here that we construct the optical potential replacing the hypernucleus density ρ in Eq. (70) with the density of the initial nucleus. The reason for this approximation is that we do not know the

kaon-Λ scattering amplitude and therefore we replace it with the kaon-nucleon one. Consequently, the final-state kaon scatters on the potential of the initial nucleus with kinematics of the final hypernucleus.

The nuclear density used in Eq. (70) can be parameterised in the harmonic oscillator representation

$$\rho(r) = (a_0 + a_1\alpha_n^2 r^2)\, e^{-\alpha_n^2 r^2}\,, \tag{72}$$

with the parameters

$$a_0 = 3\frac{A}{A-1}\left(\frac{\alpha_n}{\pi}\right)^{\frac{3}{2}}\,, \quad a_1 = \frac{2}{9}\,(A-4)\,a_0\,, \quad \alpha_n^2 = \frac{A}{A-1}\alpha_{\rm HO}^2\,,$$

where $\alpha_{\rm HO}$ is a harmonic oscillator parameter.

The nuclear density can be also described in a Hartree-Fock model or using a Woods-Saxon potential. These approaches are more realistic, especially for a description of weakly bound particles and for heavy hypernuclei.

The nuclear density in the Wood-Saxon representation is

$$\rho(r) = \frac{\rho_0}{1+\exp(\frac{r-R}{a})}\,, \tag{73}$$

where ρ_0 is a central density, $R = r_0 {\rm A}^{1/3}$ is the radius of half density, A is the mass number of a nucleus, r_0 is the Fermi radius, and a is the diffuseness parameter, that represents the surface thickness of the nucleus. These parameters where compared with the calculation and data from [68]. The parameter ρ_0 is determined by the normalization condition

$$4\pi\int_0^\infty dr r^2\rho(r) = {\rm A}\,. \tag{74}$$

The nuclear density in the Hartree-Fock method can be calculated using formula

$$\rho(r) = \frac{1}{4\pi}\sum_k |R_{n_k l_k}(r,b)|^2\,(2j_k+1)\,v_k^2\,, \tag{75}$$

where v_k is the occupation number of a single-particle state k in j-scheme, b is the harmonic oscillator parameter and $R_{n_k l_k}(r,b)$ are the radial parts of the Hartree-Fock single-particle wave functions.

2.6 Nucleus and hypernucleus structures

We describe a nucleus as a many-body system of interacting nucleons. Dynamics of this system is governed by Hamiltonian

$$\hat{H} = -\sum_{i=1}^{A}\frac{\hbar^2}{2M_N}\Delta_i + \sum_{i<j}^{A} V(\vec{r}_i,\vec{r}_j), \tag{76}$$

where M_N is the nucleon mass and $V(\vec{r}_i, \vec{r}_j)$ is the nucleon-nucleon (NN) interaction.

In this work we solve the nuclear many-body problem within methods based on the self-consistent mean field, namely the Hartree-Fock (HF) method and the Tamm-Dancoff (TD) Approximation [65]. The HF approach is based on minimization of nuclear the ground state energy to satisfy the variation condition

$$\delta\langle\Psi\,|\hat{H}\,|\Psi\rangle = 0, \tag{77}$$

where Ψ is the many-body wave function in the form of Slater determinant

$$\Psi_{\alpha_1,\alpha_2,...,\alpha_A}(\vec{r}_1, \vec{r}_2, ..., \vec{r}_A) = \frac{1}{\sqrt{A!}} \begin{pmatrix} \phi_{\alpha_1}(\vec{r}_1)\phi_{\alpha_2}(\vec{r}_1)\ldots\phi_{\alpha_A}(\vec{r}_1) \\ \phi_{\alpha_1}(\vec{r}_2)\phi_{\alpha_2}(\vec{r}_2)\ldots\phi_{\alpha_A}(\vec{r}_2) \\ \vdots \\ \phi_{\alpha_1}(\vec{r}_A)\phi_{\alpha_2}(\vec{r}_A)\ldots\phi_{\alpha_A}(\vec{r}_A) \end{pmatrix}. \tag{78}$$

The variation condition (77) leads to Hartree-Fock equation

$$-\frac{\hbar^2}{2M_N}\Delta\phi_i(\vec{r}) + U(\vec{r})\phi_i(\vec{r}) - \int d^3r'\, W(\vec{r},\vec{r}')\phi_i(\vec{r}') = \epsilon_i\phi_i(\vec{r}) \tag{79}$$

where $\phi_i(\vec{r})$ and ϵ_i are the single-particle wave functions and energies, respectively. $U(\vec{r})$ and $W(\vec{r},\vec{r}')$ are the direct and exchange potentials defined as follows

$$U(\vec{r}) \equiv \sum_{i-\mathrm{occ}} \int d^3r'\, \phi_i^*(\vec{r}')V(\vec{r},\vec{r}')\phi_i(\vec{r}'), \tag{80}$$

$$W(\vec{r},\vec{r}') \equiv \sum_{i-\mathrm{occ}} \phi_i^*(\vec{r}')V(\vec{r},\vec{r}')\phi_i(\vec{r})\,, \tag{81}$$

where the summations run over occupied states only.

The HF method can be also formulated in the second quantization formalism where the nuclear Hamiltonian (76) is expressed as

$$\hat{H} = \sum_{kl} t_{kl}a_k^\dagger a_l + \frac{1}{4}\sum_{klmn} V_{klmn}^{NN}a_k^\dagger a_l^\dagger a_n a_m. \tag{82}$$

Here $a_k^\dagger$ (a_l) are the creation (annihilation) operators, $t_{kl} =< k|(-\frac{\hbar^2}{2M_N}\Delta)|l >$ represents the kinetic operator, and $V_{klmn}^{NN} =< kl|\hat{V}(\vec{r},\vec{r}')|mn - nm >$ are antisymmetric NN interaction elements.

In the second quantization, the Slater determinant (78) which satisfies the HF variation condition (77) is represented as

$$|\mathrm{HF}\rangle = \prod_h^A a_h^\dagger|0\rangle. \tag{83}$$

In Eq. (83), particle vacuum is denoted as $|0\rangle$, and the index h denotes hole states, i.e. the single particle levels below the Fermi energy. If we reserve the index p for the single-particle states above the Fermi energy, the following conditions hold

$$a_h^\dagger|\mathrm{HF}\rangle = 0 \iff \langle \mathrm{HF}|a_h = 0, \tag{84}$$

$$a_p|\mathrm{HF}\rangle = 0 \iff \langle \mathrm{HF}|a_p^\dagger = 0. \tag{85}$$

Note that the nuclear Hamiltonian (82) as well as HF method itself can be generalized also for the case of three-body NNN interactions (for more details see [60]).

Since the HF method describes only properties of the nucleus ground state we need to introduce a many-body approach suitable to compute also the nuclear excitations. A very simple method which starts from the self-consistent single-particle basis is the Tamm-Dancoff (TD) approximation. Within this method we solve an equation of motion

$$\langle \mathrm{HF}|Q_{\nu'}[\hat{H}, Q_\nu^\dagger]|\mathrm{HF}\rangle = (E_\nu - E_{\mathrm{HF}})\delta_{\nu\nu'}, \tag{86}$$

where $\hat{H}$ is the nuclear Hamiltonian, $E_{\mathrm{HF}} = \langle \mathrm{HF}|\hat{H}|\mathrm{HF}\rangle$ is the energy of the HF ground state, and Q_ν is the phonon operator defined as general linear superposition of particle-hole excitations on the ground state

$$Q_\nu^\dagger = \sum_{ph} C_{ph}^\nu a_p^\dagger a_h. \tag{87}$$

By using the phonon operators (87) in the equation of motion (86) we obtain the TD equation

$$\sum_{p'h'}[(\epsilon_p - \epsilon_h)\delta_{pp'}\delta_{hh'} + V_{ph'hp'}^{NN}]C_{p'h'}^\nu = (E_\nu - E_{HF})C_{ph}^\nu. \tag{88}$$

Eq. (88) is an eigenvalue equation where E_ν (C_{ph}^ν) are eigen-energies (eigen-vectors), respectively.

The HF and TD methods are suitable for the description of nuclei which enter the electroproduction reaction. But we also need to describe the structure of hypernuclei produced in this reaction. To this end we use the proton-neutron-Λ Hartree-Fock method (p-n-Λ HF) and the Tamm-Dancoff Λ (TD_Λ) approximation. Both these approaches were introduced in Refs. [60, 66], where one can found more details.

In p-n-Λ HF we construct a self-consistent single-particle basis for protons, neutrons, and Λ particles by using the nucleon-nucleon and nucleon-Λ (NΛ) interactions.

In the TD_Λ approximation we start from the equation of motion in analogy to Eq. (86) but we use Λ-nucleon phonons defined as follows

$$R^\dagger_\nu = \sum_{ph} R^\nu_{ph} c^\dagger_p a_h. \tag{89}$$

In this equation $c^\dagger_p$ creates Λ in a particle state p and a_h annihilates nucleon (in the case of electroproduction proton) in the hole state h. If the phonon operator $R^\dagger_\nu$ acts on the HF ground state, the resulting many-body state describes the hypernucleus with one Λ particle bound in an even-odd nuclear core. The corresponding TD_Λ equation has the form

$$\sum_{p'h'}[(\epsilon^\Lambda_p - \epsilon_h)\delta_{pp'}\delta_{hh'} - V^{N\Lambda}_{h'php'}]R^\nu_{p'h'} = (E_\nu - E_{HF})R^\nu_{ph}, \tag{90}$$

where ϵ^Λ_p is the single-particle energy of Λ and $V^{N\Lambda}_{h'php'}$ is the interaction matrix element of the NΛ potential.

The OBDME, used in computing the reduced amplitude of hypernucleus electroproduction, is defined within the TD_Λ approximation as follows

$$R^\nu_{ph} = \frac{1}{[J_\nu]} \left\langle \nu || (c^\dagger_p \times a_h)^{J_\nu} || 0 \right\rangle, \tag{91}$$

where R^ν_{ph} is the solution of Eq. (90).

Another many-body method applied in our calculations of hypernuclear electroproduction is shell model which uses the effective ΛN interactions fitted to γ-ray spectroscopic data of p-shell hypernuclei [35]. This effective ΛN interaction is

$$V_{\Lambda N}(r) = V_0(r) + V_\sigma(r) s_N s_\Lambda + V_\Lambda(r) l_{N\Lambda} s_\Lambda + V_N(r) l_{N\Lambda} s_N + V_T(r) S_{12}, \tag{92}$$

where the tensor interaction is defined as

$$S_{12} = 3\left(\sigma_N \cdot r\right)\left(\sigma_\Lambda \cdot r\right) - \sigma_N \sigma_\Lambda = \sqrt{6} C^2\left(r\right) \cdot \left[\sigma_N, \sigma_\Lambda\right]^2. \tag{93}$$

In Eq. (92), $l_{N\Lambda} \simeq l_N$ when Λ is in the s orbit.

In our analysis we use the shell-model OBDME calculated by John Millener which were already used in previous calculations, e.g. in Ref. [56].

3 Results

In this section we present selected results of our calculations of the cross sections in electroproduction of hypernuclei. Predominantly, we will show results for ${}^{12}_{\Lambda}$B but in some cases we also present results for ${}^{16}_{\Lambda}$N, ${}^{40}_{\Lambda}$K, and ${}^{48}_{\Lambda}$K.

In subsection 3.1 we discuss the effects from the Fermi motion of the initial proton, i.e. we compare the electroproduction cross sections calculated using different values of the proton momentum such as $\vec{p}_p = 0$ ("the frozen proton approximation"), $\vec{p}_p = -\vec{\Delta}$ ("the frozen Λ approximation" as $\vec{p}_\Lambda = 0$) and the optimum proton momentum. The results are presented on the angular and energy distributions of the cross sections for various excited states of the hypernucleus and the "selection rule" is discussed. In the calculations we utilize the BS3 model [52] for the elementary amplitude and in some cases also the SLA [19] model. The nucleus and hypernucleus structure (OBDME) is described in the frame of the shell model [35] and TD$_\Lambda$ approximation [5].

In computing the kaon momentum we have introduced the following three schemes [4].
(1) The 2-Body scheme where the kaon momentum is calculated from the energy conservation in the two-body system, but the many-body system energy conservation is violated. This value is then used for the elementary amplitude, the radial integral, and the kinematical factor β in the cross section, see Eqs. (16)–(19).
(2) The Many-Body scheme where the kaon momentum is calculated from the energy conservation in the many-body system and in the two-body system the energy is not conserved. This makes that the elementary amplitude is off-energy-shell which causes additional uncertainty in the calculations. This Many-Body value is then used for the elementary amplitude, the radial integral, and kinematical factor in the cross section.
(3) The 2-Body Hybrid, scheme where we use two different kaon momenta in the calculation. One of them is calculated from the energy conservation in the two-body system and it is used for the elementary amplitude. The other momentum is calculated from the many-body system energy conservation and it is used for the radial integral, and kinematical factor in the cross section.

In subsection 3.2 we explore a significance of the contributions from the radial integral in the cross section, particularly focusing on the kaon distortion and models that can be used for computing the nuclear density present in the kaon-nucleus optical potential, namely the Woods-Saxon (WS), Hartree-Fock (HF) and Harmonic Oscillator (HO) approach.

In subsection 3.3, we delve into the importance of the One-Body Density Matrix

Elements (OBDME) in calculating the cross sections. We discuss the results obtained with the shell model and the TD_Λ approach mostly for ${}^{12}_{\Lambda}$B and ${}^{16}_{\Lambda}$N and compare them with experimental data [56]. We also provide predictions of the excitation spectra in electroproduction of ${}^{40}_{\Lambda}$K and ${}^{48}_{\Lambda}$K, which will be measured at the JLab experiment E12-15-008.

3.1 Fermi motion effect

As demonstrated in Eq. (26), in the optimal factorization approximation the elementary amplitude is calculated for an effective value of the proton momentum ($\vec{p}_{\rm eff}$) which has not been specified yet and, therefore, it is interesting to show a dependence of the cross sections on this momentum. In previous calculations [14, 56, 16, 15] the zero value of the proton momentum was used assuming that the proton is "frozen" in the nucleus whereas a non zero value of $\vec{p}_{\rm eff}$ partially accounts for the proton Fermi motion in the nucleus.

In this subsection, we will demonstrate variations in the electroproduction cross section using three different values of the proton effective momentum: $\vec{p}_{\rm eff} = 0$, $\vec{p}_{\rm eff} = -\vec{\Delta}$, and $\vec{p}_{\rm eff} = \vec{p}_{\rm opt}$ (the optimal value given in Eq. (50)). The calculations are based on the elementary BS3 amplitude [52] within the 2-body-hybrid scheme, which means that the amplitude is on-energy-shell. The nuclear structure is included using the shell model approach [35] and the results are shown for the photon energy $E_\gamma = 2.2$ GeV.

In Figs. 6 and 7 we show angular distrubution of the cross section in electroproduction of ${}^{12}_{\Lambda}$B for the ground state doublet and three states in the 11 MeV multiplet, respectively. The states are denoted with the spin-parity and the excitation energy in MeV as (J^P; E) and, from here on we denote the effective proton momentum as $\vec{p}_p$. In these figures the black solid line represents the frozen proton approximation ($\vec{p}_p = 0$), the blue doted line represents the frozen Λ approximation ($\vec{p}_\Lambda = 0$ but $\vec{p}_p = -\vec{\Delta}$) and the pink dashed line represents the optimum proton momentum approximation ($\vec{p}_p = \vec{p}_{\rm opt}$) calculated with $cos(\theta_{p\Delta}) = -1$. It should be noted, that Fig. 6 depicts the first doublet of excited states, whereas the data from the experiment E94-107 [56] is only available for the sum of those cross sections, particularly at the $\theta_{Ke} = 6^o$.

One can see in these figures that the difference of the differential cross sections calculated with $\vec{p}_p = 0$ and $\vec{p}_\Lambda = 0$ is quite large, especially at small kaon angles. On the other hand the optimum proton momentum, being about 100 MeV/c in this case, makes the results quite close to those with the zero proton momentum. From

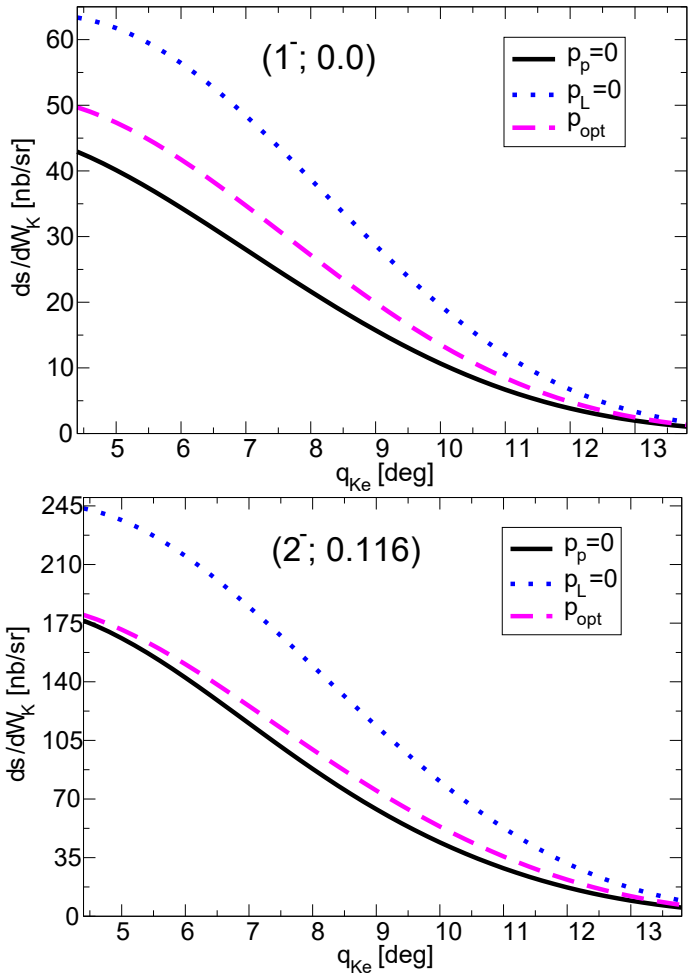

Figure 6: Fermi motion effects are shown in angular distribution of the cross section for the ground and first excited state of ${}^{12}_{\Lambda}$B. The results are for the frozen-proton ($\vec{p}_p = 0$), frozen-Λ ($\vec{p}_\Lambda = 0$), and optimum ($\vec{p}_{\rm opt}$) approximations. The states are denoted with their spin-parity and energy in MeV as (J^P; E).

comparison of the results for various hypernuclear states it is evident that the Fermi effects depend on the quantum numbers of the states (J^P). This pattern is clearly seen comparing the results for the frozen proton approximation and the optimum proton momentum. For example, it is apparent in Fig. 7 that the cross section at very small kaon angles calculated with $\vec{p}_{\rm opt}$ is more suppressed in the 1^+ and 3^+ states than in the 2^+ state. A similar behavior is observed for the 2^- and 1^- states. This pattern can be explained formulating the so-called dynamical selection rule.

In the case of the target nucleus ^{12}C, with the spin and parity of the ground state 0^+, the Clebsh-Gordan coefficients in Eq. (39) allow contributions from the spin

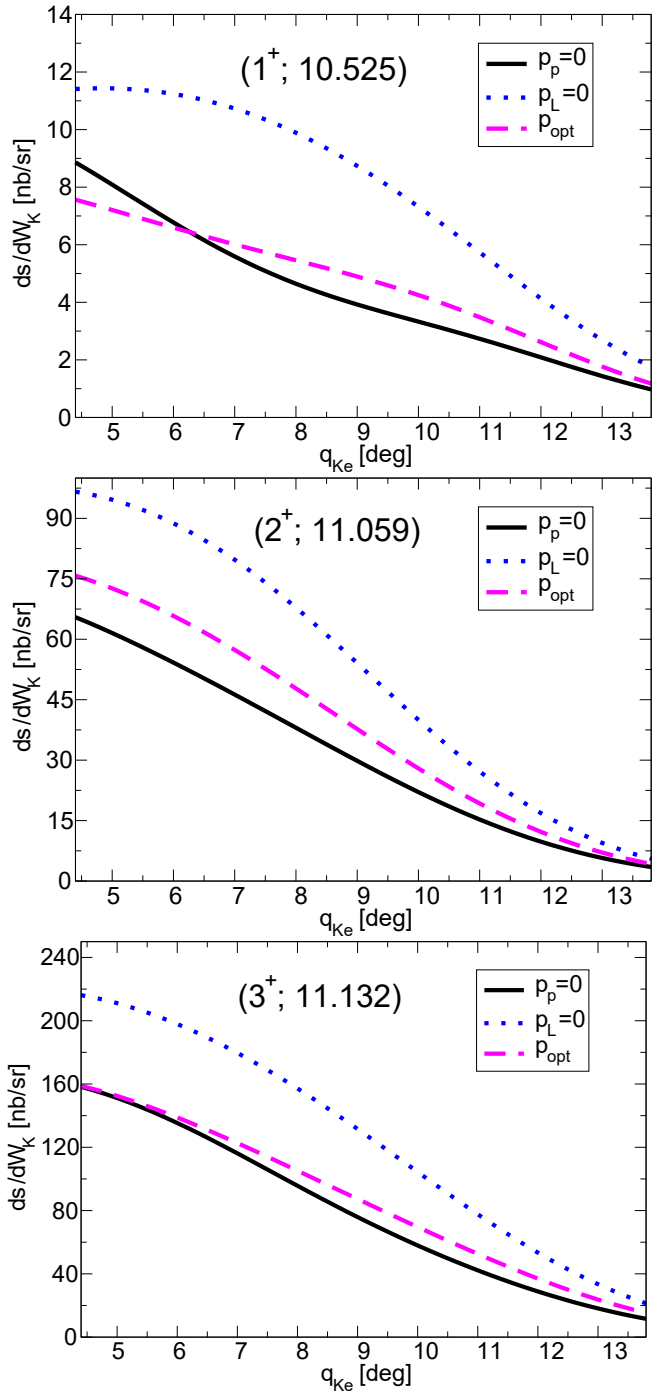

Figure 7: The same as in Fig. 6 but for the 1^+, 2^+, and 3^+ states in the multiplet at about 11 MeV.

non-flip part of the elementary amplitude ($S = 0$) to be only for the negative-parity states with odd spin and positive-parity states with even spin, i.e., for the states 1^- ($L = 1$) and 2^+ ($L = 2$). In the other states, 2^-, 1^+, and 3^+, the spin non-flip part does not contribute. However, it is important to emphasize that in the kinematical

region characterized by small kaon-photon angles $\theta_{K\gamma}$, the strength of the spin non-flip spherical amplitudes is negligibly small and the process is dominated by the spin-flip ($S = 1$) part. Therefore, this simple straightforward selection rule cannot explain the effects observed in Figs. 6 and 7.

In the numerical analysis of contributions to the reduced amplitude in Eq. (39) we found that significantly large contributions in the given kinematical region are from the radial integrals with $M = 0$ and the spin-flip elementary amplitude with $\lambda = 0$ and $\nu = 0$. One can therefore conclude that the dominant contributions to the reduced amplitude are controlled by the Clebsch-Gordan coefficient C^{J0}_{L010} which provides a simple "dynamical" selection rule for the longitudinal component of the reduced amplitude ($\lambda = 0$). In particular, the longitudinal amplitude A^0_{J0} notably contributes only for the states 2^-, 1^+, and 3^+ but it does not for the states 1^- and 2^+. This results in a substantial enhancement of the longitudinal $\mathrm{d}\sigma_L$ and interference $\mathrm{d}\sigma_{TL}$ cross sections. This effect is also shown in Table 1 where the amplitude $|A^0_{J0}|$ is zero for the state 1^- but non zero for 2^-. Note that in the considered kinematics with a very small value of Q^2 the longitudinal component of the amplitude is generally quite small. However, this dynamical selection rule can explain the different order of the curves for the two groups of states presented in Figs. 6 and 7.

Differences of the Fermi motion effects in separate contributions to the full cross section, the transverse (T), longitudinal (L), and interference (TL) parts, are shown in Figs. 8 and 9 for the states 1^- and 3^+ of ${}^{12}_{\Lambda}\mathrm{B}$. We can observe the differences mainly in behaviour of the L and TL parts, where in the case of the 3^+ state the former adds quite an important contribution to the full cross section at small kaon angles rising the full cross section with respect to the transverse part. However, we see that this effect depends on the value of the proton effective momentum, $\vec{p}_{\mathrm{p}} = 0$ or $\vec{p}_{\mathrm{opt}}$.

Numerical results for the full and separate cross sections and the longitudinal component ($\lambda = 0$) of the reduced amplitude are shown in Table 1 for the states 1^- and 2^-. The values are calculated at the angle $\theta_{Ke} = 6^\circ$ for different values of the proton momentum using the 2-body-hybrid scheme, where the elementary amplitude is on-energy-shell. One can observe a significant enhancement of $d\sigma_{\mathrm{L}}$ and $d\sigma_{\mathrm{TL}}$ for the 2^- state attributed to contributions from $|A^0_{20}|$. Similarly, the longitudinal cross section is enhanced in the states 1^+ and 3^+. The calculations in Table 1 show that the contribution of the longitudinal component $|A^0_{20}|$ to the cross section is more pronounced in the frozen proton and the optimum proton momentum approximation.

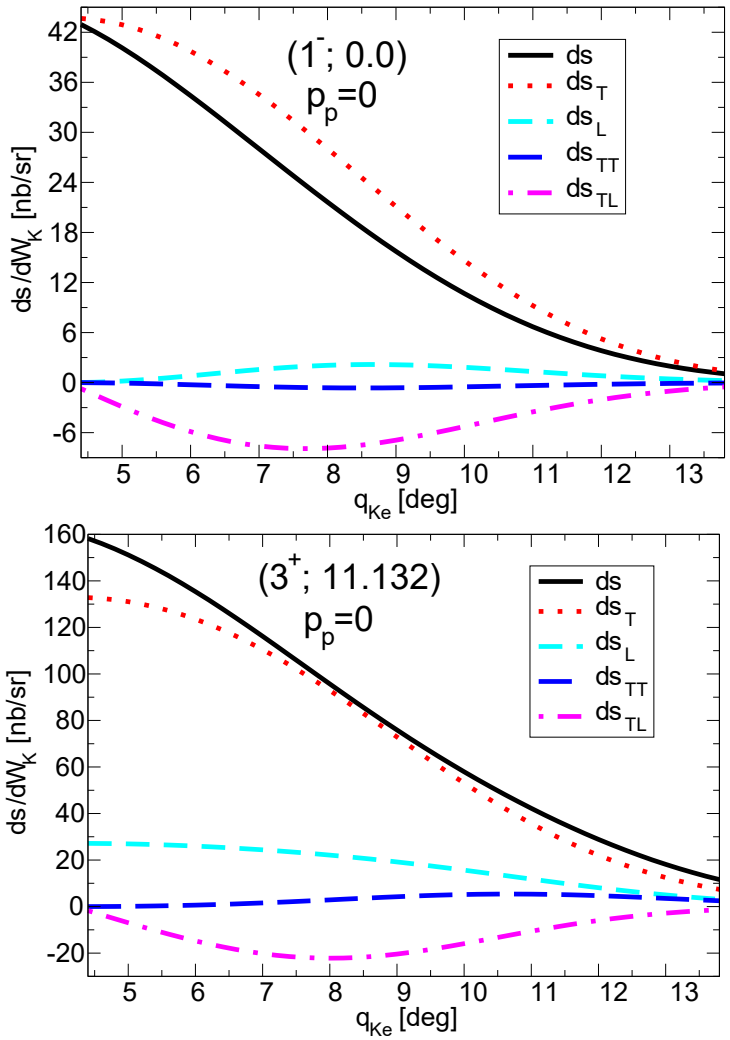

Figure 8: Separate contributions to the electroproduction cross section, namely the transverse (T), longitudinal (L) and interference parts (TT, TL), for the ground and an excited state of ${}^{12}_{\Lambda}$B. The results are for the zero proton momentum, $\vec{p}_{\rm p} = 0$ (the frozen proton approximation).

Note that even if the virtuality of the photon is small ($Q^2 = 0.06$ (GeV/c)^2) the contributions of the longitudinal modes, d$\sigma_{\rm L}$ and d$\sigma_{\rm TL}$ to the full cross section are quite important.

It is also important to note a distinction between the electroproduction and photoproduction calculations. In the considered kinematical region, characterized by small values of $\theta_{K\gamma}$ and Q^2, the transverse part of the full cross section is dominant. However, contributions from the longitudinal (L) and interference (TL) parts are also important as we have shown it in Figs. 8 and 9 and in Table 1. Recall that these lon-

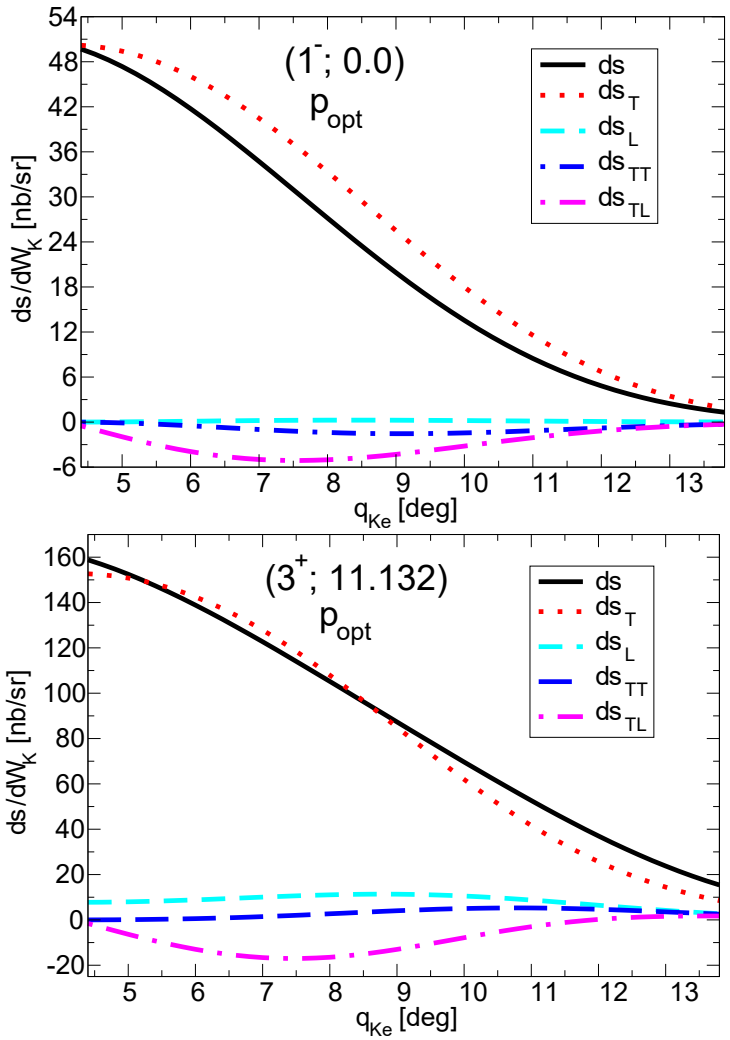

Figure 9: The same as in Fig. 8 but with the optimum proton momentum, $\vec{p}_{\rm p} = \vec{p}_{\rm opt}$.

gitudinal components play a significant role, especially for the 2^-, 1^+ and 3^+ states. The comparison of the excitation spectrum for ${}^{12}_{\Lambda}$B calculated with the full differential cross section $d\sigma$ (the electroproduction) and only with the transverse part $d\sigma_{\rm T}$ (approximately equivalent to the photoproduction) is shown in Fig. 10. The difference is not too big, which is due to a relatively small value of Q^2 in the considered kinematics. The results in the region of the two main peaks show that the longitudinal components tend to reduce a bit the full cross section. In Figs. 8 and 9 one can see that at $\theta_{Ke} = 6^\circ$, except for the state 3^+, the negative TL component is important, which results in a reduction of the full cross section observed in Fig. 10.

As the optimum proton momentum depends also on the angle with respect to the momentum transfer $\vec{\Delta}$ (see Fig. 5), it is desirable and interesting to show how much

Table 1: The full differential cross section and its components, such as the transverse (T), longitudinal (L), and interference (TL) are shown for the ground-state doublet of ${}^{12}_{\Lambda}$B and for various proton momenta. In the last column, the reduced amplitudes with $\lambda = 0$ are also presented. The calculations were carried out within the two-body hybrid scheme and kinematics $Q^2 = 0.06$ (GeV/c)^2, $E_\gamma = 2.2$ GeV, $\epsilon = 0.7$, $\theta_{Ke} = 6°$, and $\Phi_K = 180°$. The cross sections are in nb/sr.

$(J^p; E_x)$	proton momentum	dσ	d$\sigma_{\rm T}$	d$\sigma_{\rm L}$	d$\sigma_{\rm TL}$	$\lvert A^0_{J0}\rvert$
$(1^-; 0.0)$	$\vec{p}_p = 0$	34.4	39.72	0.82	-5.88	0.0
	$\vec{p}_p = -\vec{\Delta}$	56.43	58.69	0.07	-1.46	0.0
	$\vec{p}_p = \vec{p}_{\rm opt}$	41.74	46.04	0.11	-3.92	0.0
$(2^-; 0.116)$	$\vec{p}_p = 0$	142.47	135.35	25.91	-19.6	0.1806
	$\vec{p}_p = -\vec{\Delta}$	215.11	197.7	23.35	-6.83	0.0299
	$\vec{p}_p = \vec{p}_{\rm opt}$	150.53	156.09	8.69	-15.03	0.0709

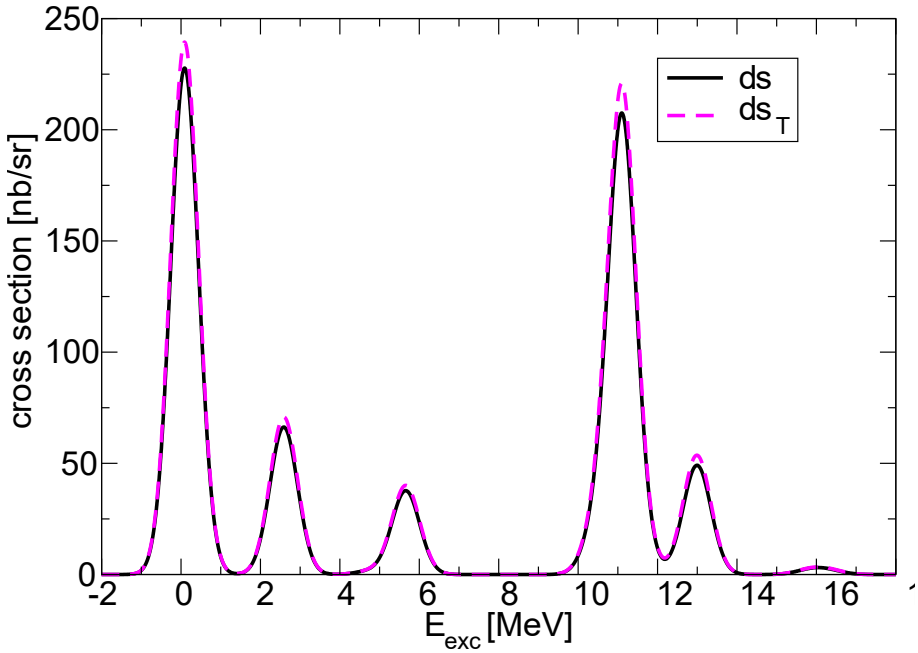

Figure 10: The full electroproduction cross section ($d\sigma$) and its transverse part ($d\sigma_{\rm T}$) are compared for ${}^{12}_{\Lambda}$B. The results are calculated using OBDME from the shell model and the elementary amplitude BS3 with the optimum proton momentum ($\vec{p}_{\rm p} = \vec{p}_{\rm opt}$).

the cross sections depend on this angle $\theta_{\Delta p}$. This dependence is shown in Figs. 11 and 12 for the values of $\cos(\theta_{\Delta p})$ in the range from -1 to 0.26. Note that the previous

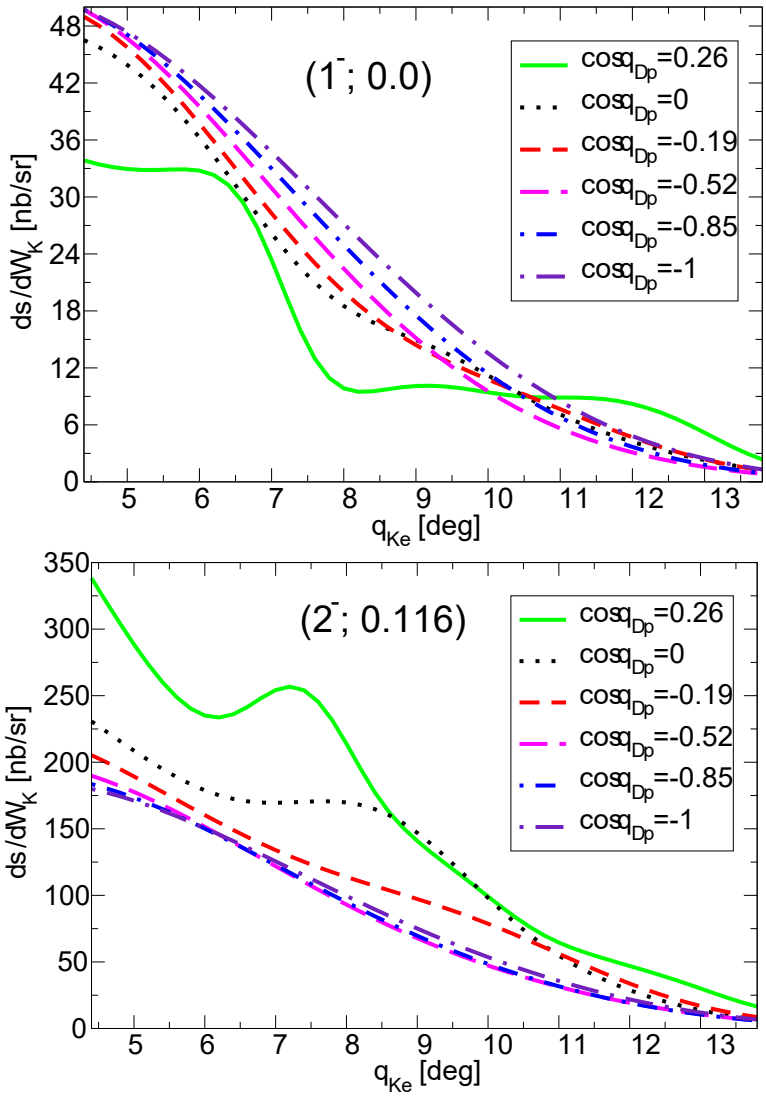

Figure 11: Angular dependence of the electroproduction cross section for the ground and first excited state of ${}^{12}_{\Lambda}$B calculated in the optimum on-shell approximation with different values of $\cos(\theta_{\Delta p})$.

calculations in this work and in Refs. [4, 5, 56] were done with the value $\cos(\theta_{\Delta p}) = -1$ and that this value provides the minimum value of the Λ momentum.

In Table 2 we present values of the proton and Λ momentum in electroproduction of ${}^{12}_{\Lambda}$B for different values of the angle $\theta_{\Delta p}$. For the values smaller than $\theta_{\Delta p} = 90°$ we observe a notable increase in the proton and Λ momentum. However, such large particle momenta can be considered as non-physical because both proton and Λ bound in a nucleus and hypernucleus, respectively, cannot have momenta exceeding reasonable

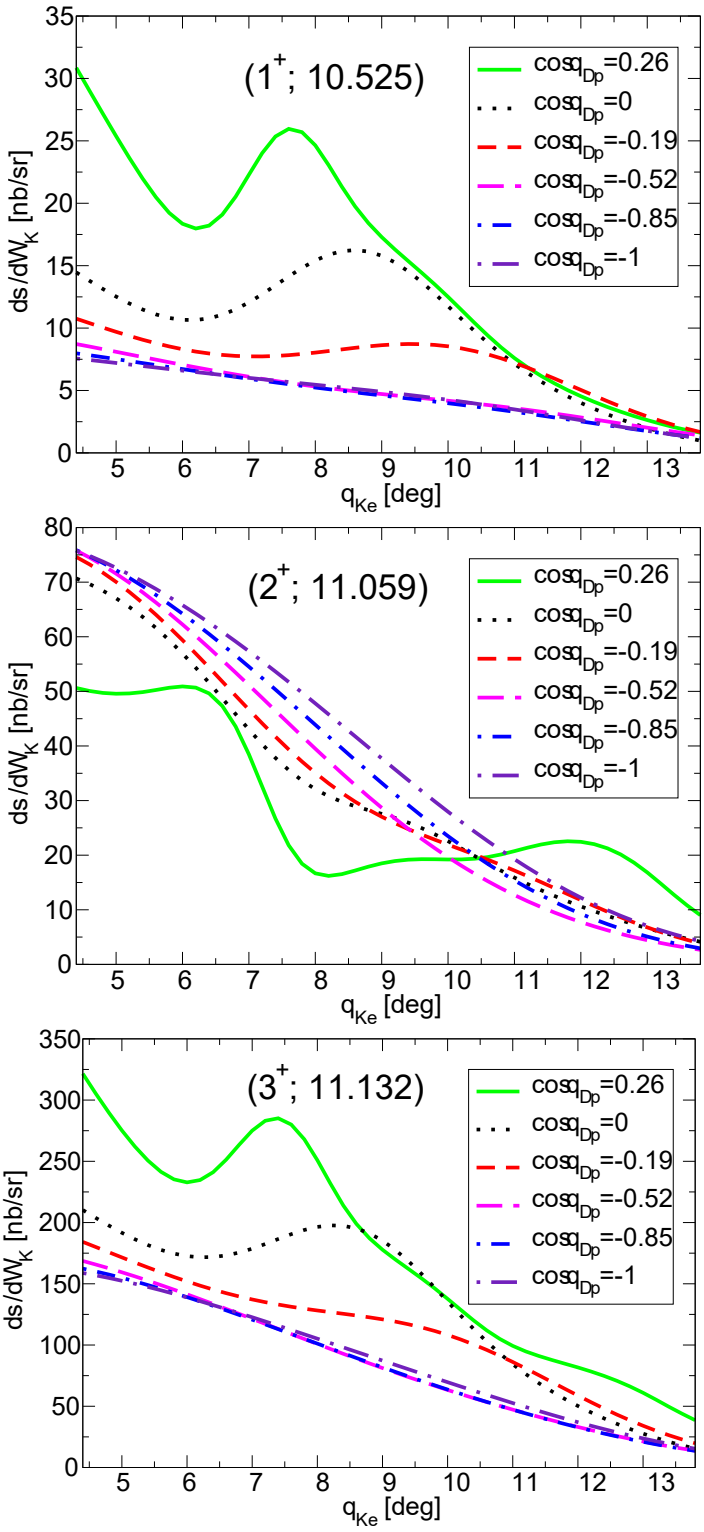

Figure 12: The same as in Fig. 11 but for the 1^+, 2^+, and 3^+ states in the multiplet at about 11 MeV.

Table 2: The optimum proton momentum in electroproduction of ${}^{12}_{\Lambda}$B is shown for different values of $\cos(\theta_{\Delta p})$, similarly as in Fig. 5, in kinematics $Q^2 = 0.06$ (GeV/c)^2, $E\gamma = 2.2$ GeV, $\epsilon = 0.7$, $\theta_{Ke} = 6°$, and $\Phi_K = 180°$. The momentum of Λ is also shown for comparison.

$\cos(\theta_{\Delta p})$	-1.0	-0.85	-0.52	-0.19	0	0.26
p_p (GeV/c)	0.099	0.115	0.175	0.331	0.548	1.24
p_Λ (GeV/c)	0.17	0.182	0.232	0.385	0.61	1.33

limits allowed by the nuclear structure, i.e. to remain bound particles. A possible characteristic of the motion of a particle bound in the nucleus is its mean momentum calculated for a particular single-particle state. In ^{12}C the mean momentum of the proton in the p shell is about 180 MeV/c. Therefore, only the values of the proton momentum for $\cos\theta_{\Delta p} \leq 0$ given in Table 2 seem to be reasonable. In Figs. 11 and 12 we see that the results with $\cos\theta_{\Delta p} = 0.26$ markedly deviate from the others. One can also observe a difference in the dependence of the cross sections on $\theta_{\Delta p}$ for various hypernucleus states. This difference for the group of states 1^- and 2^+ and for the other group 1^+, 3^+, and 2^- can be again attributed to the dynamical selection rule and, particularly, to the contributions from the longitudinal modes of the virtual photon. This is also consistent with the observations in Figs. 8 and 9.

The effects in the excitation spectrum of ${}^{12}_{\Lambda}$B from various values of $\cos(\theta_{\Delta p})$ are shown in Fig. 13. We see that the values of $\theta_{\Delta p}$ smaller than 180° give quite a significant enhancement of the cross section. It seems that the value adopted in previous calculations, $\cos(\theta_{\Delta p}) = -1$ with the minimum magnitude of the Λ momentum is quite good in view of experimental data. Note that magnitudes of the peaks depend on the width used in calculating the excitation spectrum.

Alternatively, one can consider averaging of the elementary amplitude over the angle $\theta_{\Delta p}$ with a cut-off on the angle, $\theta_{\Delta p} < 100°$, to prevent excessively high proton momenta. This averaging can effectively be interpreted as averaging over various values of the optimum proton momentum, where the elementary amplitude remains on its energy shell. It is important to recall that in our calculations, we operate within the optimal factorization approximation, which means that we do not average over the proton motion, i.e., we do not perform the so called Fermi averaging or the

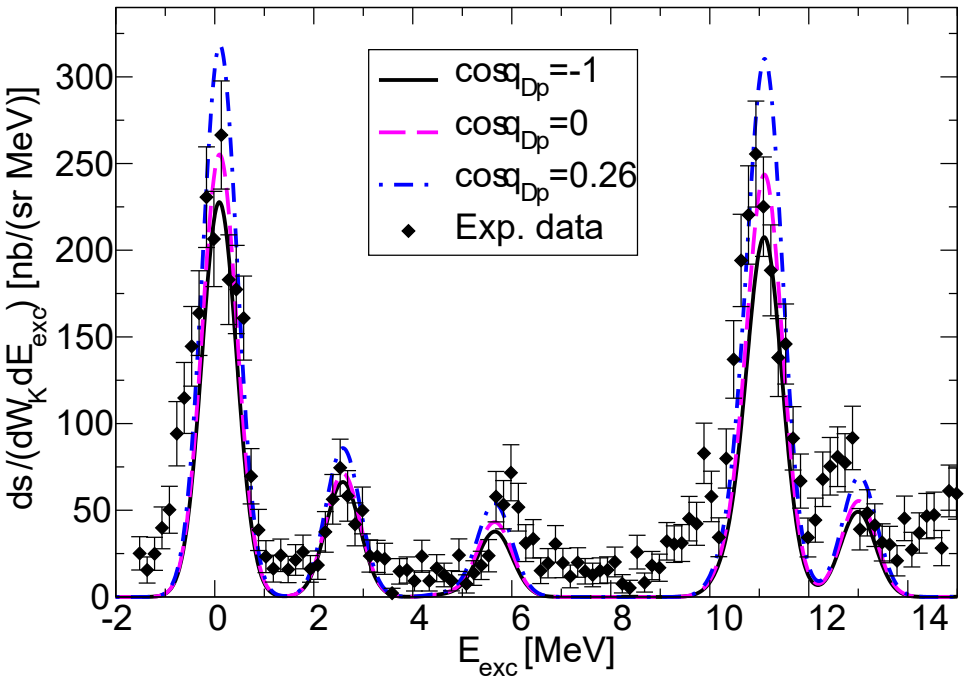

Figure 13: The excitation spectrum of ${}^{12}_{\Lambda}$B calculated for different values of $\cos\theta_{\Delta p}$. The results were obtained using the OBDME from the empirical shell model and the BS3 elementary amplitude in the optimum on-shell approximation. Distortion of the final kaon was included. The experimental data on the 3-fold differential cross section were taken from Ref. [56] and divided by the virtual-photon flux factor Γ in Eq. (15).

full-folding integration.

As we already mentioned, we can perform the calculations in various schemes of determining the magnitude of the kaon momentum. It is therefore interesting to show the kinematic effects resulting from the utilization of various kaon momenta obtained in these schemes. In Figs. 14 and 15 we show comparison of the differential cross sections calculated in the 2-body, 2-body-hybrid, and many-body schemes. The calculations were done with the BS3 elementary amplitude in the frozen-proton approximation ($\vec{p}_p = 0$). The energy of the virtual-photon is $E_\gamma = 2.2$ GeV. Note that in the many-body scheme the energy in the 2-body vertex is not conserved and therefore the elementary amplitude is off its energy shell, i.e., in the region where the amplitude is not well under control because it was constructed on-shell assuming the data in the elementary reaction. The impact of employing the off-energy-shell elementary amplitude is evident from the comparison between the 2-body-hybrid (on-shell) and many-body (off-shell) schemes.

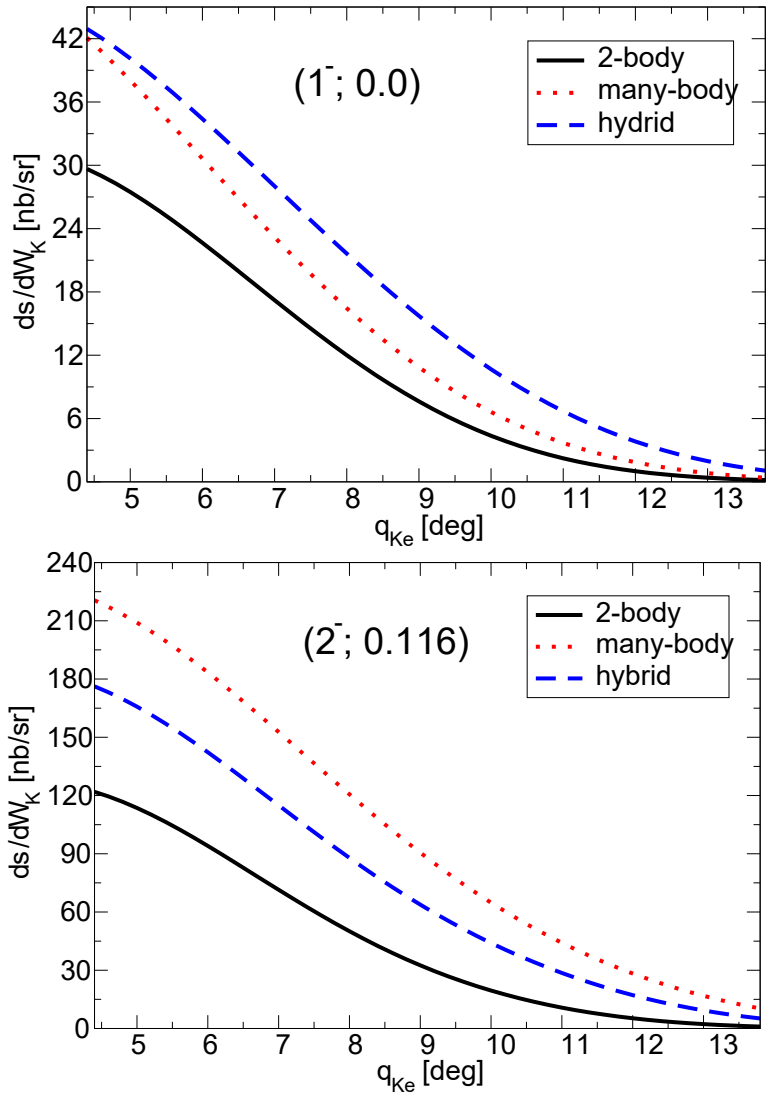

Figure 14: The electroproduction cross section for the ground-state doublet of ${}^{12}_{\Lambda}$B calculated in the frozen-proton approximation ($\vec{p}_{\rm p} = 0$) using the BS3 elementary amplitude and various schemes of computing the kaon momentum: 2-body, many-body, and 2-body hybrid.

The effects arising from different values of the kaon momentum $|\vec{p_K}|$ are significant in the whole displayed angular region in Figs. 14 and 15. Even though the discrepancy between the values of $|\vec{p_K}(2b)|$ and $|\vec{p_K}(mb)|$ in the considered kinematics with $\theta_{Ke} = 6^\circ$ is relatively small, the corresponding momentum transfer $|\vec{\Delta}|$ experiences an approximately 10% difference, thereby elevating the values of the radial integrals. Indeed, the comparative analysis of the results in the 2-body and 2-body-hybrid schemes reveals influences from the radial integrals and the normalization of

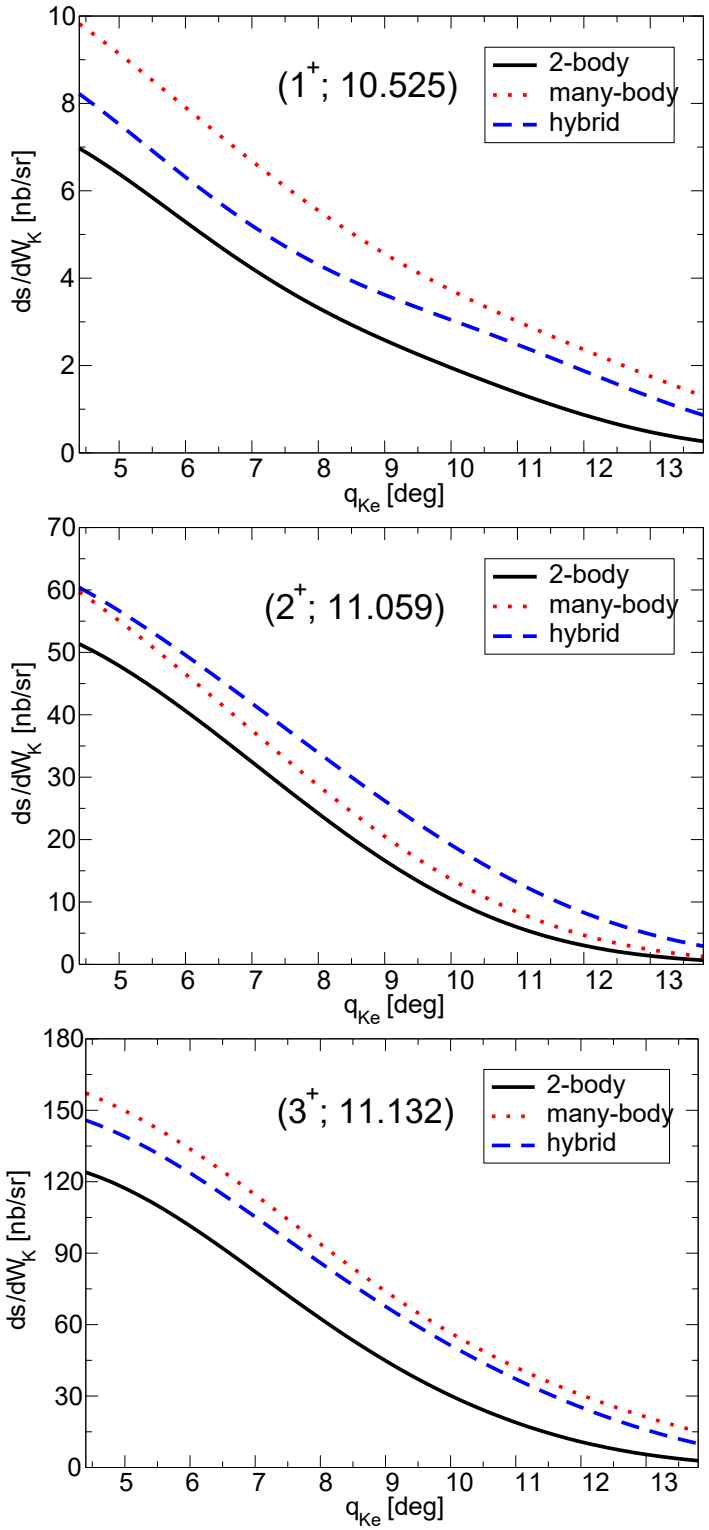

Figure 15: Same as Fig. 14 but for the 1^+, 2^+, and 3^+ states of ${}^{12}_{\Lambda}$B in the multiplet at about 11 MeV.

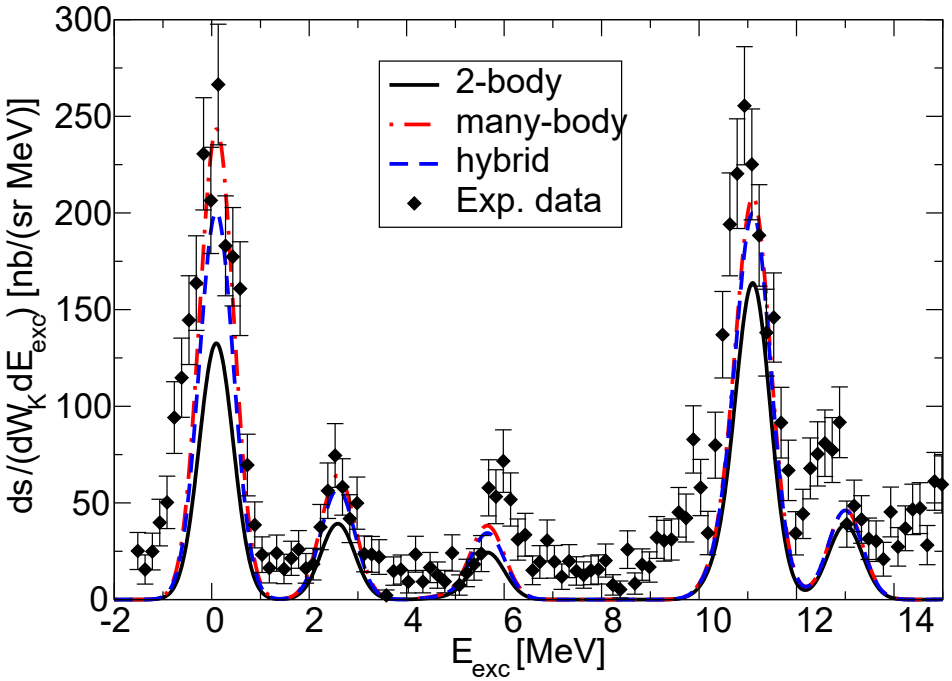

Figure 16: The excitation spectrum of ${}^{12}_{\Lambda}$B calculated using various computation schemes, incorporating the OBDME from the empirical shell model and the BS3 elementary amplitude in the optimum on-shell approximation, along with the inclusion of final kaon distortion. The experimental data are the same as in Fig. 13.

cross sections controlled by the parameter β, see Eqs. (16)–(19).

If we compare the cross sections for many-body and hybrid schemes in Figs. 14 and 15 their behaviour differs for the group of states the 2^-, 1^+, and 3^+ and for the other group of the states, namely 1^- and 2^+. Interestingly, the curves for the two groups of states, for example those of the states 1^- and 2^-, exhibit distinct ordering. This feature can be understood through a numerical analysis of contributions to the reduced amplitude A^{λ}_{Jm} in Eq. (39). Indeed, from the analysis, one can conclude that the radial integrals with $M = 0$ acquire the largest values, particularly their imaginary components, and that the radial integrals are rising functions of $|\vec{p_K}|$. Then because $|\vec{p_K}(mb)| > |\vec{p_K}(2b)|$, the cross section in the many-body scheme is larger than that in the 2-body scheme.

We can compare cross-section calculations with the same kinematics $E_\gamma = 2.2$ GeV, $\theta_{Ke} = 6°$, and $\Phi_K = 180°$ but using different calculation schemes for the kaon momentum. In Fig. 16 we can see that a small violation ($\approx 1\%$) from many-body energy conservation in the 2-body scheme leads to a reduction in cross sections by

approximately 10–20% compared to the 2-body-hybrid scheme. In all calculations, both prior and subsequent, we prefer to utilize the 2-body-hybrid scheme with the on-energy-shell amplitude. This preference arises from the fact that it is quite a challenging task to effectively control an extension of the elementary amplitude off its energy shell.

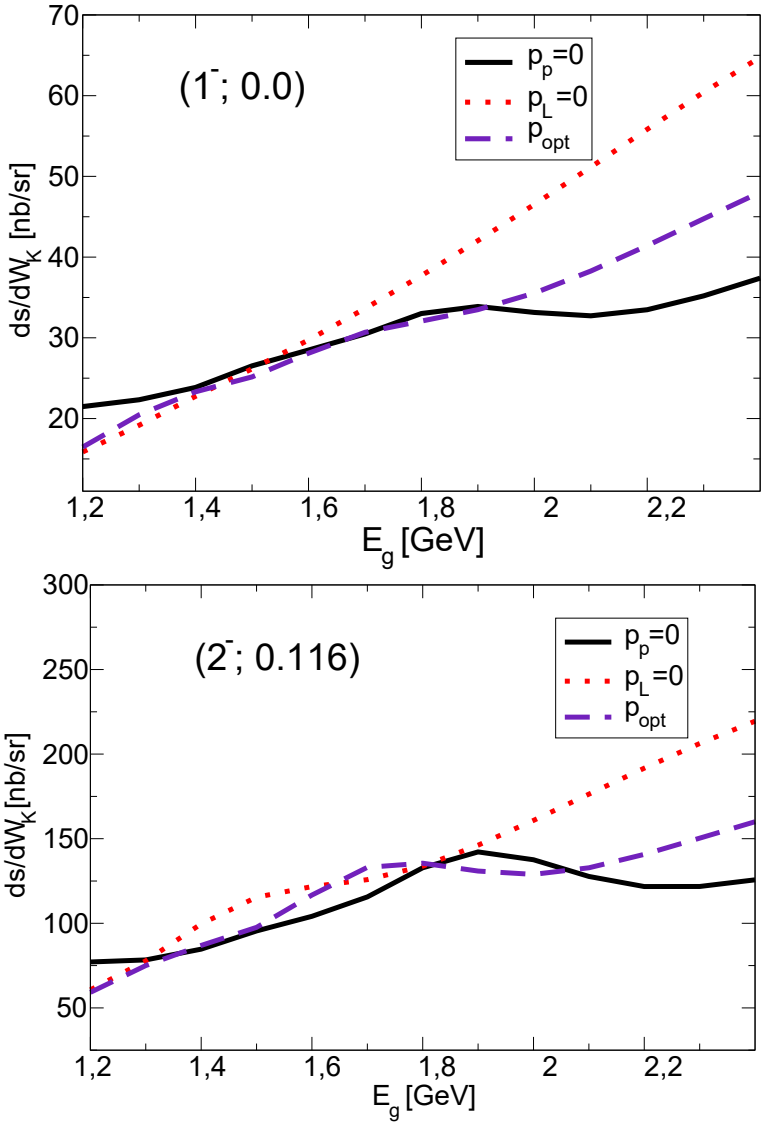

Figure 17: Energy dependence of the cross section in electroproduction of ${}^{12}_{\Lambda}$B at the kaon angle $\theta_{Ke} = 6^\circ$ is compared for different values of the proton momentum. The results for the ground and first excited state were obtained with the elementary amplitude BS3 and the OBDME from the shell model.

So far we presented the Fermi motion effects in the case of angular distribution of

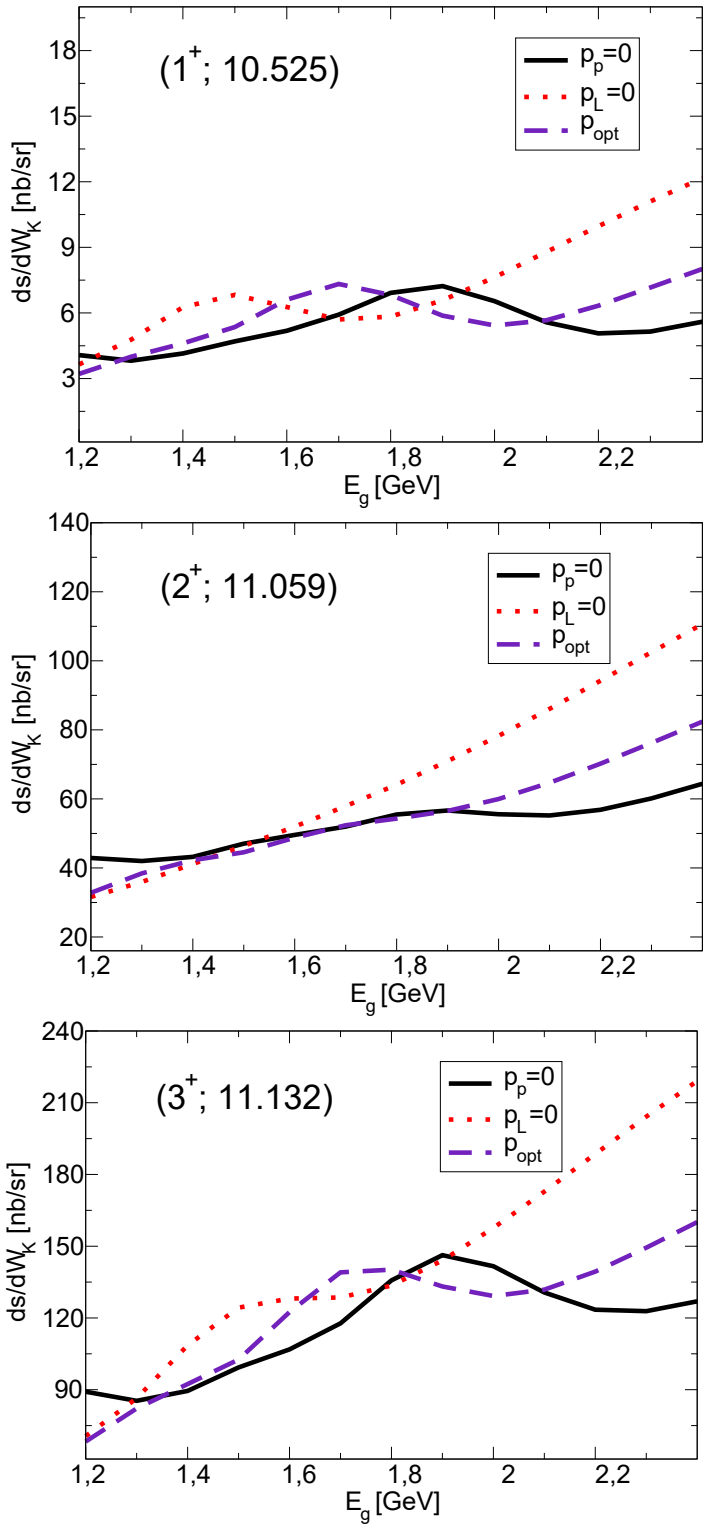

Figure 18: The same as in Fig. 17 but for the states in the multiplet at 11 MeV.

the cross sections at energy 2.2 GeV. It is also interesting to show the effects on the energy dependence of the cross sections. Here one can expect a distinct behaviour of the effects for different elementary amplitudes due to their different energy dependence.

The energy-dependent effects from using various proton momenta are shown in Figs. 17 and 18 for the elementary amplitude BS3. The cross sections were calculated using the 2-body hybrid scheme in the fixed kinematic $Q^2 = 0.06\,(\mathrm{GeV/c})^2$, $\epsilon = 0.7$, $\Phi_K = 180°$, and $\theta_{Ke} = 6°$ where the electron kinematics was adjusted accordingly. Note also that using the 2-body hybrid scheme in all cases assures that the elementary amplitude in on-shell.

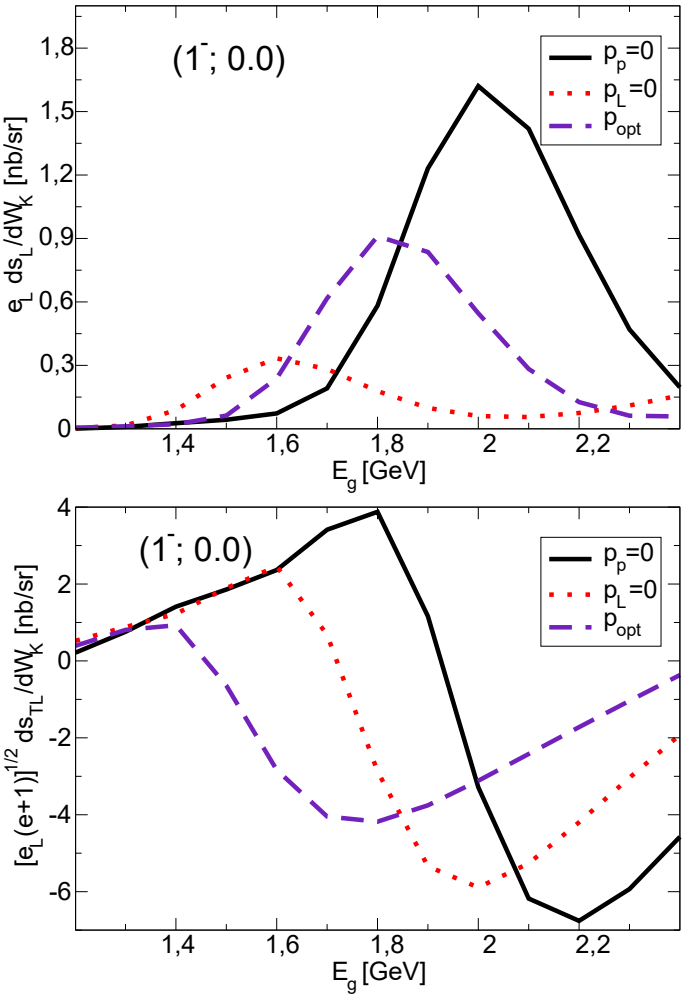

Figure 19: Energy dependence of the cross section in electroproduction of ${}^{12}_{\Lambda}$B at the kaon angle $\theta_{Ke} = 6°$ with different values of the proton momentum for the ground state. Contributions from longitudinal (L), and transverse-longitudinal interference (TL) parts to the full cross section are presented.

While character of the results with the given elementary amplitude is largely the same for all states, see for example the order of the curves above 2 GeV, the magnitude of the effect from the proton motion depends on the energy. Note that the particular shape of the curves depends also on the elementary amplitude. The cross sections differ significantly more for the photon energies above about 2 GeV. where the cross sections are rising for all proton momenta. On the other hand the results with different proton momentum do not differ too much below 2 GeV. In the region of 1.7–2 GeV one observes a resonant structure which can be attributed to the longitudinal contributions in the reduced amplitude controlled by the dynamical selection rule. This is therefore the reason why the resonant structure is more pronounced in the group of the states 2^-, 1^+, and 3^+ than in the other group of 1^- and 2^+ states.

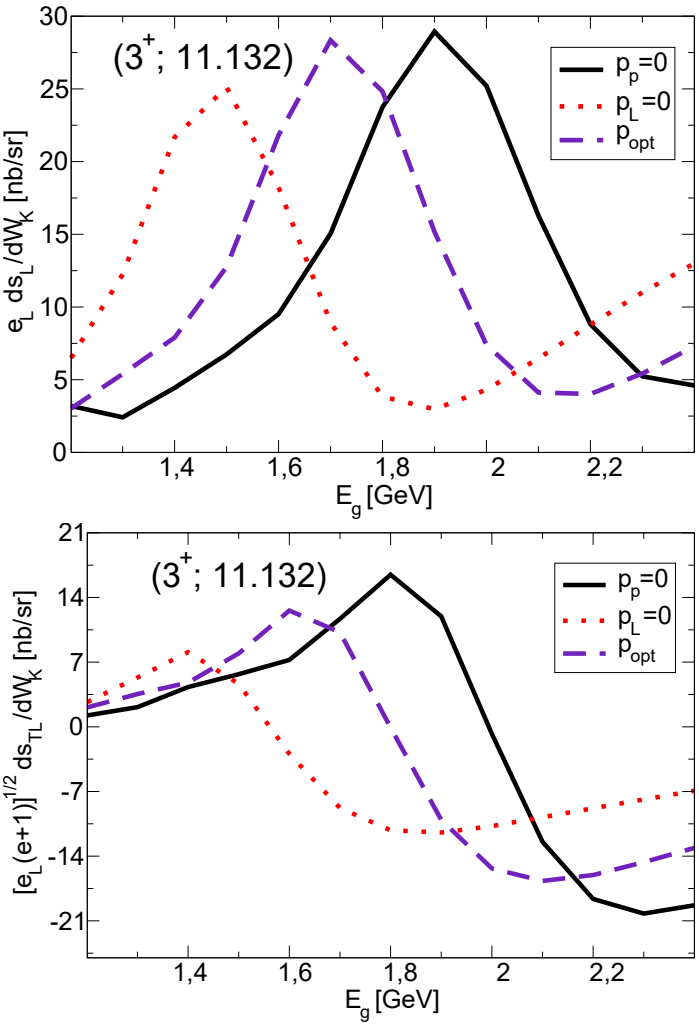

Figure 20: Same as in Fig. 19 but for the 3^+ state.

Contributions from the longitudinal and transverse-longitudinal interference parts of the differential cross section for the ground and 3^+ excited states are shown in Figs. 19 and 20, respectively. One can observe the resonant pattern in the energy region 1.7–2 GeV for both states but with a different strength. The relative importance of these longitudinal contributions (L and TL) in the full cross section is about a factor five larger for the 3^+ state than for the 1^- ground state. This phenomenon can be attributed to a significant contribution from the elementary amplitude F^1_{00} in the longitudinal part for the 3^+ state (where $A^0_{30} \neq 0$), which is absent in the 1^- state

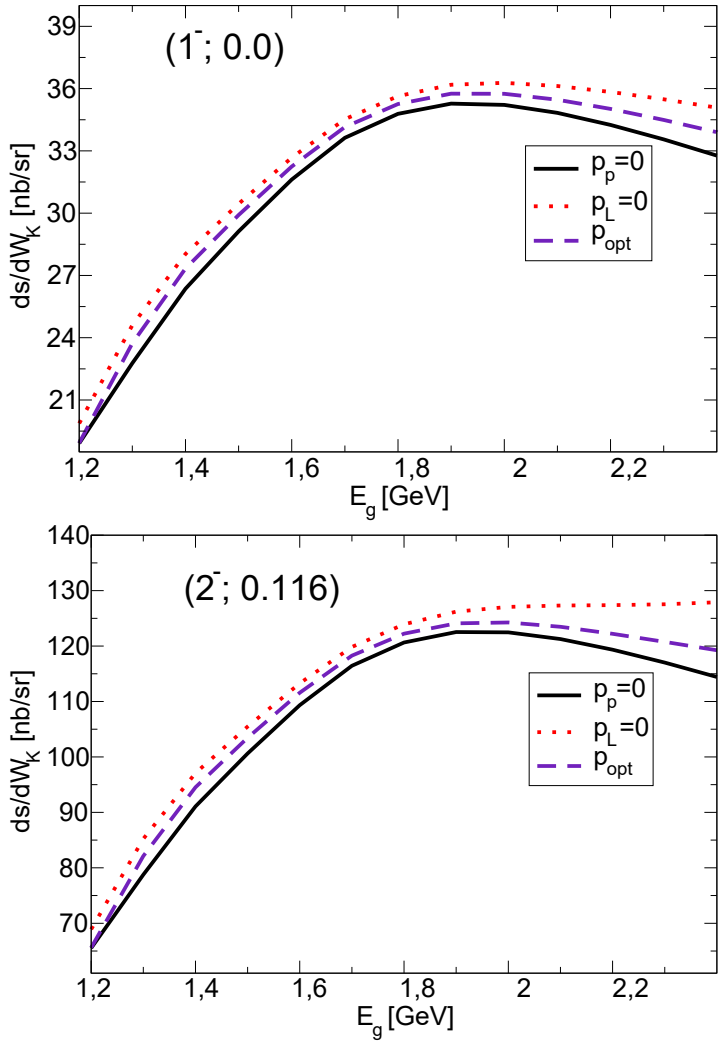

Figure 21: Energy dependence of the cross section in electroproduction of ${}^{12}_{\Lambda}$B at the kaon angle $\theta_{Ke} = 6^\circ$ calculated using the elementary amplitude SLA with different values of the proton momentum. The ground and first excited states are shown.

(where $A^0_{10} = 0$). The relatively large contribution from the longitudinal part at 2 GeV further emphasizes the importance of electroproduction calculations even in kinematics with a photon that is almost real ($Q^2 = 0.06$ (GeV/c)^2).

As the nature of the Fermi motion effects depends also on the elementary amplitude we depict in Figs. 21 and 22 the energy dependence of the cross sections calculated with the elementary amplitude SLA. We see a smooth energy dependence of the cross sections in the whole considered energy region which is due to a moderate energy dependence in the SLA amplitude. This is especially apparent at energies above 2.2 GeV where the results with SLA did not tend to diverge so much as the results with the BS3 amplitude. The Fermi motion effects observed in Figs. 21 and 22 remain moderate also in the other energy region suggesting that the contribution from the longitudinal mode of the virtual photon is not so much important in the SLA as in BS3 amplitude where it forms the resonant structure. It is the wealthy energy dependence in the BS3 amplitude that makes more pronounced structures in the energy dependence of the hypernucleus cross sections in comparison with the SLA amplitude.

3.2 Effects from kaon distortion

In electroproduction of hypernuclei the distortion of the kaon wave function in the final state is an important effect in computing the production cross sections. Including the kaon distortion in DWIA reduces the cross section by several tens of per cent in comparison with the results obtained in PWIA. Therefore, it is useful to discuss the kaon distortion in more detail.

In Fig. 23 we compare the cross sections for several states of ${}^{12}_{\Lambda}$B calculated in PWIA and DWIA. The comparison is done for (a) the frozen proton approximation, (b) frozen Λ approximation, and (c) the optimum proton momentum. We can confirm that the kaon distortion makes the cross sections smaller by about 30% and that these effects do not depend too much on the kaon angle. Note that at very small angles the Fermi motion effect also amounts about 35%, see for example the difference of the DWIA cross section in the $p = 0$ and $p_\Lambda = 0$ cases for the 3^+ state.

The cross sections calculated in PWIA and DWIA at $E_\gamma = 2.2$ GeV and $\theta_{Ke} = 6^\circ$ are compared in Table 3. We see that the relative suppression of the cross section in DWIA in not the same for all states. It is clearly visible that the difference between PWIA and DWIA is steadily decreasing with rising energy of the excited state: it varies from 45% for the ground state $(J^P; E) = (1^-; 0.0)$ to 35% for the excited state

Table 3: Comparison of the cross sections for selected states of ${}^{12}_{\Lambda}$B calculated in PWIA and DWIA. The results are for three different values of the proton momentum calculated in kinematics $Q^2 = 0.06$ (GeV/c)^2, $E_\gamma = 2.2$ GeV, $\epsilon = 0.7$, $\theta_{Ke} = 6°$, and $\Phi_K = 180°$. The virtual-photon flux factor is $\Gamma = 0.0174$ (GeV sr)$^{-1}$ and the cross sections are in nb/sr.

proton momentum	$(J^P; E_x)$	PWIA	DWIA
$\vec{p}_p = 0$	$(1^-; 0.0)$	61.9	34.4
	$(2^-; 0.116)$	250.61	142.47
	sum	**312.52**	**177.1**
	$(1^+; 10.525)$	11.04	6.78
	$(2^+; 11.059)$	82.15	54.21
	$(3^+; 11.132)$	195.39	135.39
	sum	**288.85**	**196.38**
$\vec{p}_p = -\vec{\Delta}$	$(1^-; 0.0)$	99.17	56.43
	$(2^-; 0.116)$	388.49	215.11
	sum	**487.66**	**271.54**
	$(1^+; 10.525)$	16.4	11.24
	$(2^+; 11.059)$	131.53	88.76
	$(3^+; 11.132)$	301.88	197.9
	sum	**449.81**	**297.9**
$\vec{p}_p = \vec{p}_{\rm opt}$	$(1^-; 0.0)$	74.14	41.74
	$(2^-; 0.116)$	268.97	150.53
	sum	**343.11**	**192.27**
	$(1^+; 10.525)$	10.06	6.6
	$(2^+; 11.059)$	98.38	65.79
	$(3^+; 11.132)$	207.18	138.85
	sum	**315.62**	**211.24**

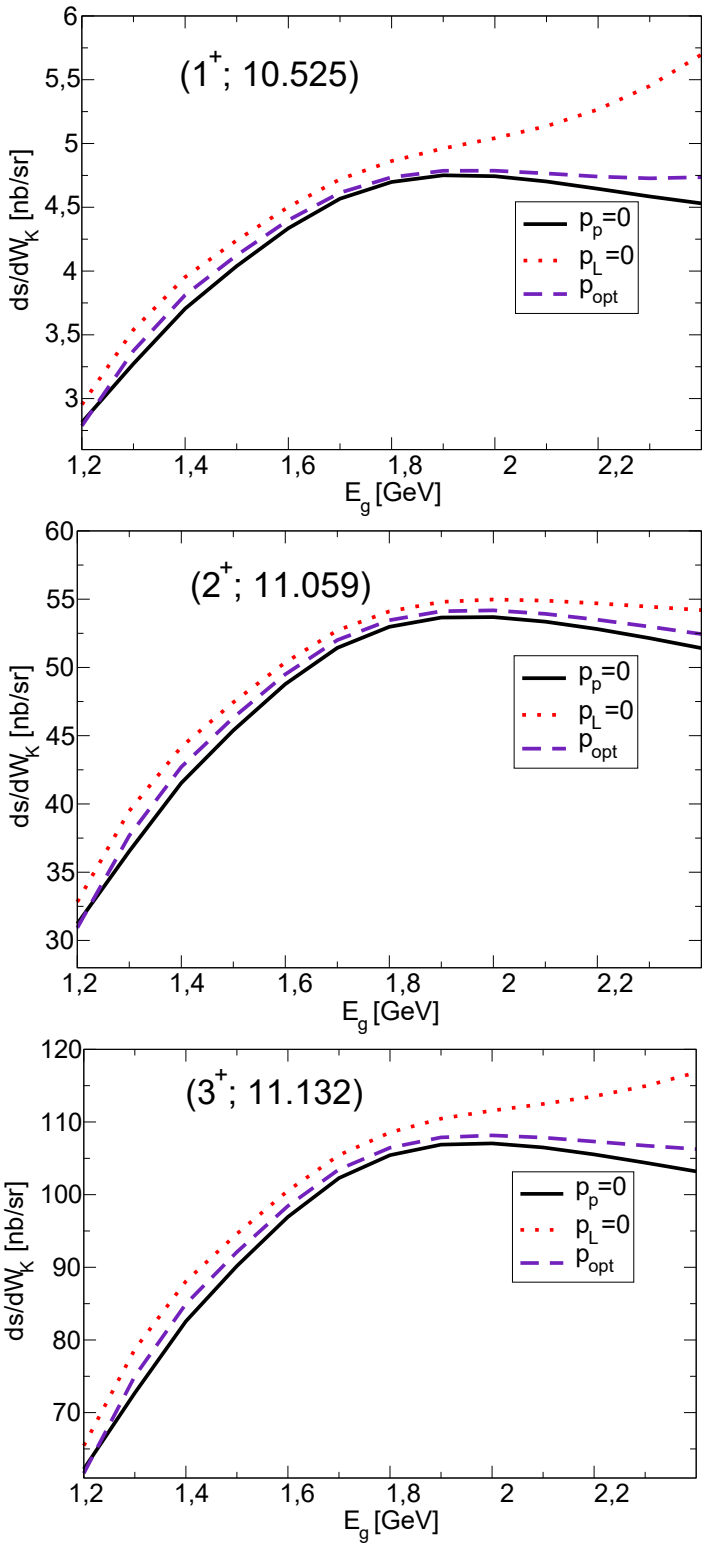

Figure 22: The same as in Fig. 21 but for states in the multiplet at 11 MeV.

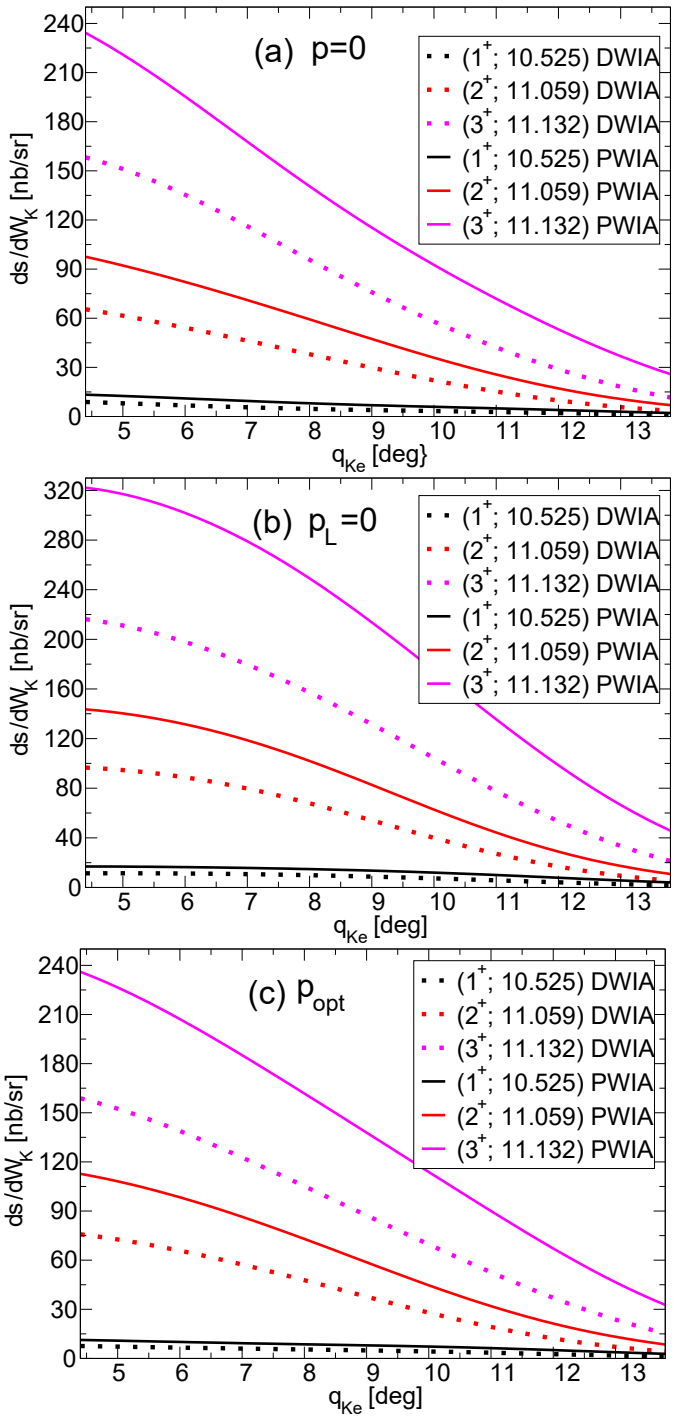

Figure 23: Angular distribution of the cross section in electroproduction of ${}^{12}_{\Lambda}$B with (a) frozen proton momentum $p_{\rm eff} = 0$, (b) frozen Λ momentum $p_\Lambda = 0$, and (c) optimum proton momentum $p_{\rm eff} = p_{\rm opt}$. Different colors are used for various states with the spin-parity and energy (J^P; E). The solid and the dashed lines are for calculations in PWIA and DWIA, respectively.

$(J^P; E) = (3^+; 11.132)$. In the ground state, the Λ particle is more deeply bound leading to a stronger distortion of the kaon wave function. From previous comparison we know that the suppression of the cross sections in DWIA improves agreement with the experimental data and therefore using DWIA is necessary.

In Table 3 we also present the sum of the cross sections for the given multiplet which can be compared with the experimental data [56] taken in the same kinematics ($E_\gamma = 2.2$ GeV, $\theta_{Ke} = 6°$, and $\Phi_K = 180°$). The experimental value of the triple-differential cross section for the $(1^-; 0.0)$ and $(2^-; 0.116)$ states is $\simeq$ 3.61 - 5.41 nb/(sr^{2}GeV) and that for the $(1^+; 10.525)$, $(2^+; 11.059)$ and $(3^+; 11.132)$ states is $\simeq$ 3.84 - 5.52 nb/(sr^{2}GeV). Dividing these values by the virtual-photon flux factor $\Gamma = 0.0174\ (GeVsr)^{-1}$ we obtain values of the differential cross section $\mathbf{207.47 - 310.92}$ nb/sr and $\mathbf{220.69 - 317.24}$ nb/sr, respectively. These values can be compared with the calculations from Table 3. It is evident that the experimental cross sections align more closely with the DWIA results where the non-zero effective proton momentum is assumed.

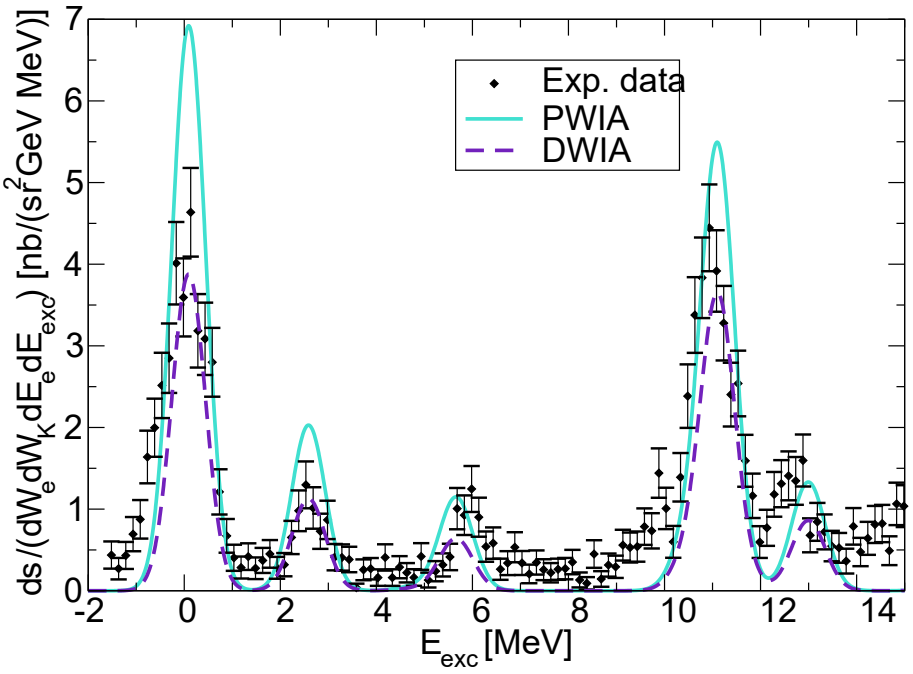

Figure 24: Calculations in PWIA and DWIA are compared with the experimental data on the excitation spectrum in electroproduction of ${}^{12}_{\Lambda}$B [56]. The theoretical results were obtained using the OBDME from the shell model [4] and the elementary amplitude BS3.

In Fig. 24 we compare the excitation spectrum of ${}^{12}_{\Lambda}$B calculated in PWIA and DWIA with experimental data [56]. The theoretical predictions were obtained using the OBDME from the shell model calculations [35] and the elementary amplitude BS3. This comparison clearly demonstrates that considering the kaon distorted wave brings the result much closer to the experimental data than the result with the kaon plane wave. One can also see that the difference between the PWIA and DWIA results is bigger for the ground-state doublet than for the multiplet at 11 MeV. This discrepancy arises because the Λ hyperon is located in the s shell for the ground-state doublet of ${}^{12}_{\Lambda}$B and in the p shell in the 11-MeV multiplet. This makes larger overlap of the wave functions in the radial integral rising the effect of kaon distortion in the former case.

As we showed in Eq. (70) the kaon distorted wave function depends (in our approximation) on the nucleus density $\rho(r)$ used in constructing the kaon-nucleus first-order optical potential. This density can be calculated assuming various approaches. It is therefore interesting to show how much various forms of the nucleus density influence the hypernucleus production cross sections.

In Fig. 25 we show various forms of the nuclear density for ^{12}C, ^{16}O and ^{48}Ca obtained in different approaches. The densities were calculated employing the parametrization in the harmonic oscillator model (HO), the Hartree-Fock (HF) method, and the Wood-Saxon (WS) potential. The densities differ mainly in the central region of the nucleus and the case of ^{48}Ca the HO density provides a very bad description.

In Fig. 26, we present predictions of the excitation-energy spectrum of ${}^{48}_{\Lambda}$K in the planned experiment E12-15-008 at JLab. The cross sections were calculated with the elementary amplitude BS3 in the optimum on-shell approximation. The nucleus-hypernucleus structure was described using the $N\Lambda$ TDA formalism with the effective Nijmegen interaction and $k_F = 1.5$ fm^{-1}. The experiment is planned in kinematics: $E_i = 2.24$ GeV, $E_f = 0.74$ GeV, $\theta_e = 8.0^\circ$, $\theta_{Ke} = 11^\circ$, and $\Phi_K = 180^\circ$. In accounting for the kaon distortion we used the HO parametrization and the HF method. It is evident from the results that including of the kaon distortion in DWIA significantly suppresses the cross sections (by 50-60%) in both cases. However, the difference between the HF and HO results is very small even if the HO density provides unrealistic description of ^{48}Ca as we can see in Fig. 25.

In Fig. 26 we also see that the effects from the kaon distortion are more pronounced for the medium-mass hypernuclei than for lighter (p-shell) hypernuclei. This is be-

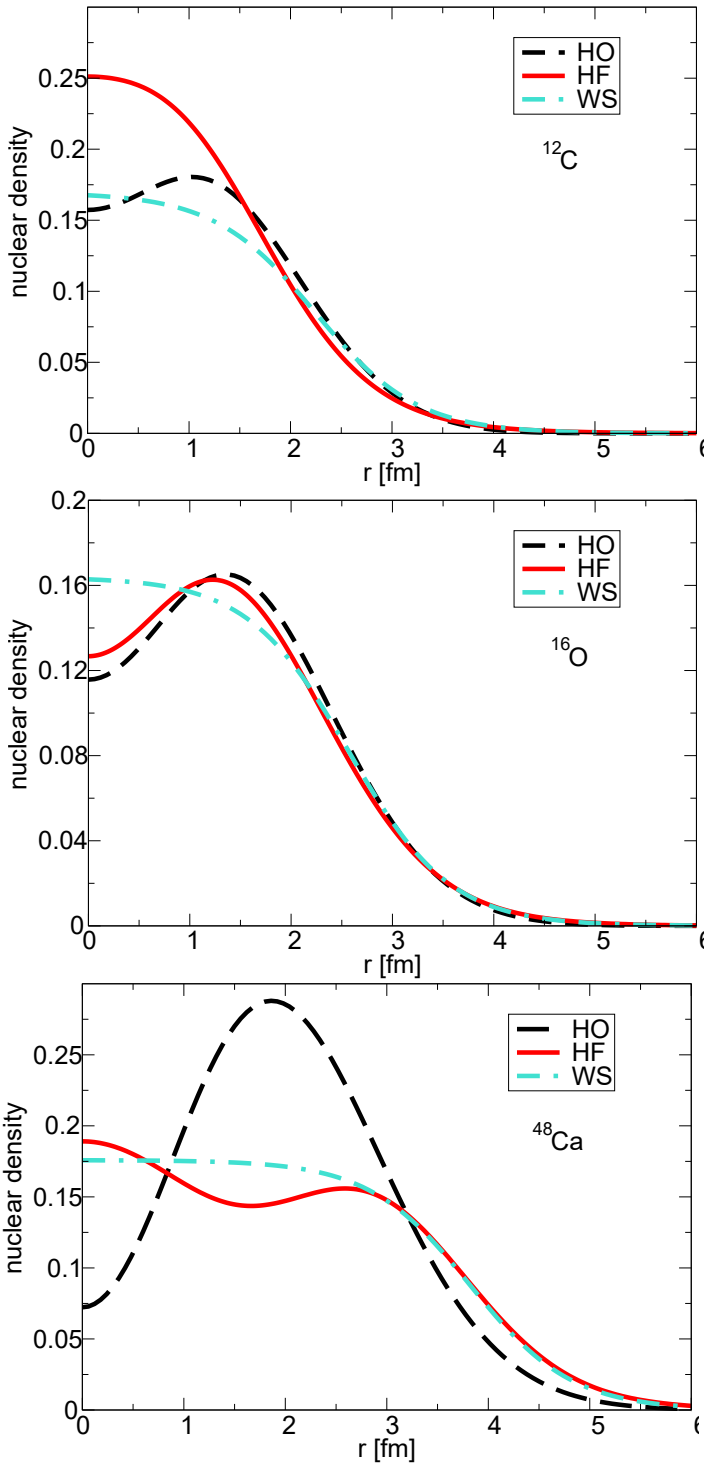

Figure 25: Nuclear density of ^{12}C, ^{16}O and ^{48}Ca calculated using the harmonic oscillator parametrization (HO), the Hartree-Fock method (HF), and the Woods-Saxon potential (WS).

cause the kaon-nucleus optical potential is, in general, deeper and with longer range for heavier nuclei and the mean free path of the kaon moving inside a hypernucleus

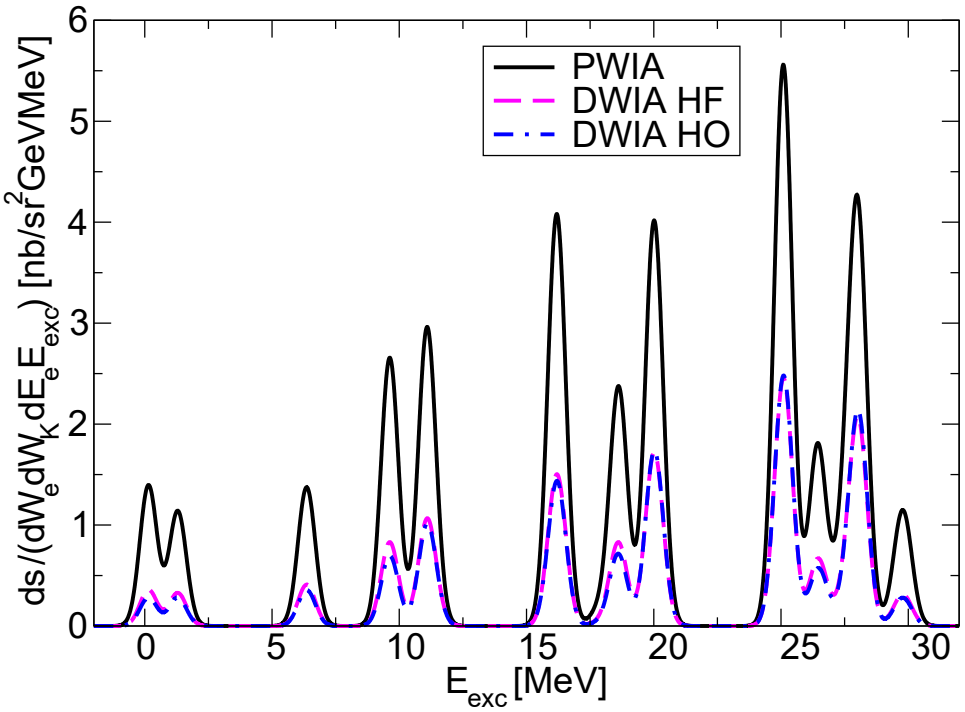

Figure 26: Predictions of the excitation spectrum for electroproduction of ${}^{48}_{\Lambda}$K calculated in kinematics of the upcoming experiment E12-15-008 at Jefferson Laboratory. The results obtained in PWIA are compared with the DWIA results calculated with two different forms of the nuclear density (HF and HO) in the kaon-nucleus optical potential.

is larger.

In Table 4 we demonstrate differences of the differential cross sections for ${}^{48}_{\Lambda}$K calculated using the HO and HF densities in the DWIA. It is evident that the difference strongly depends on the particular hypernucleus state. For some states, such as 1^+ and 2^-, the calculations exhibit even substantial discrepancies, 17–25%. Note, however that this is still smaller effect than the difference of the cross sections calculated in DWIA and PWIA. Conversely, for the higher-energy ($E_{exc} > 19$ MeV) states, the differences between the HO and HF cross sections are smaller, approximately 2–6%, suggesting that both forms of nuclear densities are quite suitable for these states. This variance observed in Table 4 can be attributed to a different overlap of the proton and Λ radial wave functions and the function F_{LM} as given in Eq. (68).

E_{exc} [MeV]	J^P	$d\sigma$ with HO	$d\sigma$ with HF	percentage diff
0.148	1^+	16.8035	21.4916	24.5%
6.359	3^+	15.6061	18.0227	14.4%
9.657	2^-	23.0594	27.3040	16.9%
11.068	2^-	20.6302	22.3071	7.8%
11.117	3^-	35.0237	36.6657	4.6%
18.671	1^+	18.8498	22.8882	19.3%
16.217	4^-	53.6477	56.7453	5.6%
19.941	3^+	30.5433	30.0982	1.5%
20.067	4^+	51.1163	49.8918	2.4%
24.980	4^+	28.9620	28.4601	1.7%
25.155	5^+	82.9344	81.2487	2.1%
28.013	4^-	40.0661	37.6276	6.3%
28.129	5^-	52.9324	49.5265	6.6%

Table 4: The differential cross sections for selected hypernucleus states in electroproduction of ${}^{48}_{\Lambda}$K. The DWIA results are obtained in the TD$_\Lambda$ formalism using the Nijmegen F YNG interaction with $k_F = 1.25$ fm^{-1} and the elementary amplitude BS3 in the optimum on-shell approximation. Two different forms of the nuclear density are considered: the Harmonic Oscillator (HO) and the Hartree-Fock (HF). The percentage difference between the results with HO and HF is shown.

3.3 Nuclear structure effects

Calculations of the hypernucleus wave functions were performed within the HF and TD$_\Lambda$ methods with the Hamiltonian

$$H = T_{\rm intr} + V = T_N + T_\Lambda - T_{\rm c.m.} + V_{\rm sat} + V_{\Lambda N}\,. \tag{94}$$

The intrinsic kinetic term $T_{\rm intr}$ is derived by subtracting the center of mass energy term, $T_{\rm c.m.}$, from the kinetic energies of nucleons (T_N) and Λ (T_Λ). The chiral NNLO$_{sat}$ potential, $V_{\rm sat}$, consists of NN + NNN parts [62]. This interaction was optimized in order to reproduce the low-energy NN scattering data as well as binding energies and radii of selected nuclei up to oxygen and carbon isotopes [62]. While the NNN component is considered explicitly when constructing the HF basis, the TD$_\Lambda$ calculations are solved with two-body NN interaction corrected by NNN term within normal-order approximation [66]. Let us notice that residual NNN interaction would

not affect TD_Λ, anyway. We used the effective NΛ potential in the form of G-matrix derived from the Nijmegen-F YN interaction [63] parameterized by a sum of Gaussian functions,

$$V_{\Lambda N}(r) = \sum_{i=1}^{3}(a_i + b_i k_F + c_i k_F^2)\exp(-\mathrm{r}^2/\beta^2), \tag{95}$$

where a_i, b_i, c_i coefficients are given in [63]. This potential depends on Fermi momentum k_F which plays a role of physical parameter.

The shell model calculations were performed assuming the nucleons in the p shell and Λ in the s and p shells. The effective YN interaction was constructed in frame of this shell model approach fitting the free parameters to γ-ray spectroscopic data of the p-shell hypernuclei [35]. This effective YN interaction is therefore fully consistent with the shell model formalism and can describe well the γ-ray spectroscopic data of the p-shell hypernuclei. Note also that the $\Lambda - \Sigma$ mixing is included in this calculation. In computing the OBDME within this approach the Woods-Saxon single-particle basis was adopted and therefore we also use this basis in calculating the radial integrals.

In Figs. 27 and 28 we present a comparison of the excitation spectra in electroproduction of ${}^{12}_{\Lambda}$B and ${}^{16}_{\Lambda}$N calculated within the TD_Λ and shell model approaches. The theoretical results are also compared with experimental data from Ref. [56]. Note that the theoretical results presented in Ref. [56] there obtained in the frozen-proton approximation whereas our new results presented here and in Ref. [4] were obtained in the optimum on-shell approximation which, together with other tiny modifications, significantly enhances agreement with the experimental data.

As one can see in Fig. 27, the result obtained within the TD_Λ approach is well consistent with the data and the SM result in the region of the main peaks at 0 and 11 MeV which correspond to Λ bound in the s and p orbit, respectively. The central energy of these peaks therefore agree quite well with the experiment. The TD_Λ calculations were executed with the HF basis and are parameter-free, except for the Fermi momentum k_F. This parameter was chosen to reproduce the empirical energy gap between the $(0p_{3/2})_\Lambda$ and $(0s_{1/2})_\Lambda$ states, resulting in $k_F = 1.1$ fm^{-1}.

However, the TD_Λ method lacks the observed small excitations in between the two main peaks in Fig. 27 generated by excitations of the core nucleus ^{11}C [56]. This discrepancy suggests that the production strength is more concentrated in these states in the TD_Λ calculation compared to the shell model one, where the strength is also distributed across the core-excited region in a better agreement with the data. This is also why the peaks in TD_Λ are so high in comparison with those in SM. To accurately

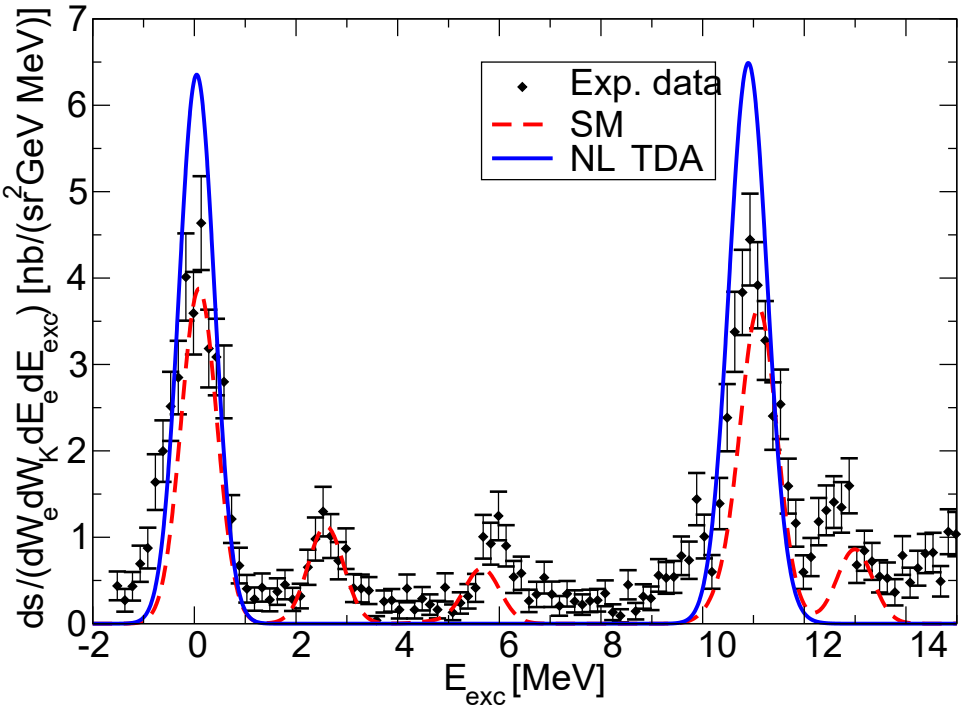

Figure 27: The excitation spectra of ${}^{12}_{\Lambda}$B calculated in the TD$_\Lambda$ method (the blue line) and the empirical shell model (the dashed red line) are compared with experimental data from Ref. [56]. The calculations were performed using the BS3 elementary amplitude in the optimum on-shell approximation with kaon distortion included.

describe the core-excited peaks, an approach beyond the mean-field description is needed, for example the equation of motion phonon method (EMPM$_\Lambda$) [5], which is an extension of EMPM used in ordinary nuclear physics. Indeed, in the EMPM$_\Lambda$ description, the magnitudes of the main peaks are reduced redistributing the strength into a new structure in the region of core-excited states. However, in this approach, the second peak at 11 MeV is slightly shifted to lower energy and the structure in the core-excited region differs from that observed in the data. These new features observed in the EMPM$_\Lambda$ approach are attributed to a more complex structure of the hypernuclear wave function, which is correlated by complex configurations of the NΛ TDA states coupled to the phonon excitations of the core. For more detailed information on the EMPM$_\Lambda$ method, its description and calculations, see Ref. [5].

The excitation spectrum in electroproduction of ${}^{16}_{\Lambda}$N is shown in Fig. 28. The result obtained from the NΛ TDA approach with the Nijmegen YN interaction and $k_F = 1.1\,\mathrm{fm}^{-1}$ (solid blue line) does not accurately depict the positions of the second and fourth peaks. These peaks are associated with the proton $p_{3/2}$ hole state and with

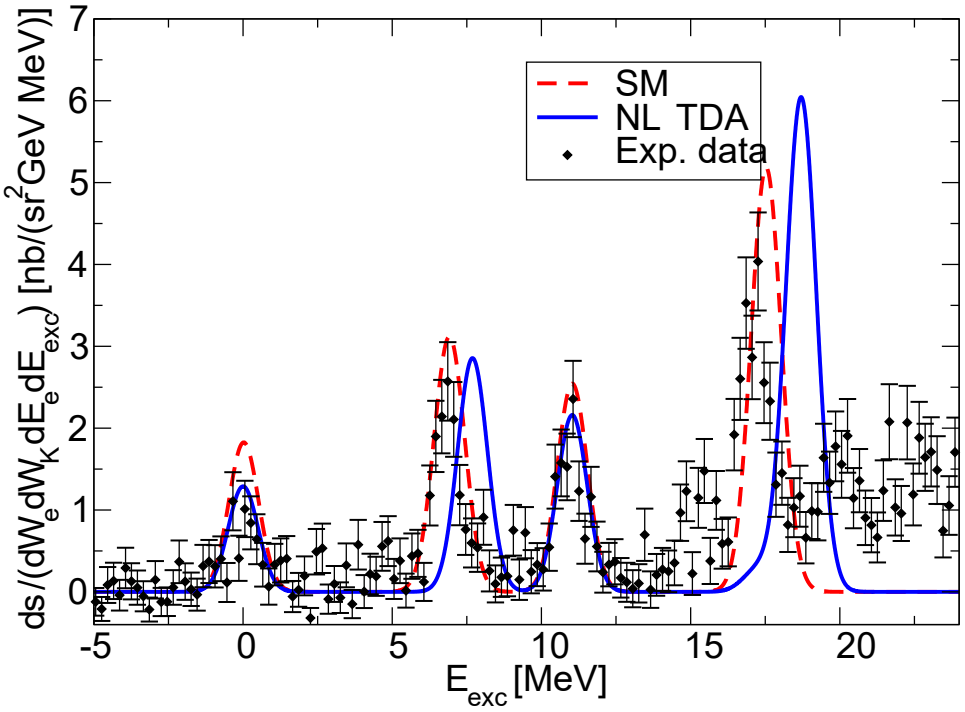

Figure 28: The same as in Fig. 27 but for ${}^{16}_{\Lambda}$N.

the Λ hyperon occupying the s and p orbit, respectively. The discrepancy suggests a problem with accurate description of the energy gap between the proton $p_{3/2}$ and $p_{1/2}$ levels, where the latter is represented by the first and third peaks in the excitation spectrum. Varying the value of k_F, which alters the effective YN interaction, typically changes the gap between the states with Λ in the s and p orbits, corresponding to the first and third peaks, and between the second and fourth peaks. However, this modification is unnecessary in this context. Instead, adjusting the energy gap between the first and second peaks can be achieved by modifying the three-nucleon interaction (NNN). For further discussion, we refer to [5].

The excitation-energy spectrum of ${}^{40}_{\Lambda}$K is illustrated in Fig. 29. The calculations were performed with the BS3 amplitude in the frozen-proton approximation and in kinematics of the planned JLab experiment E12-15-008 set at $E_\gamma = 1.3$ GeV and $\theta_K = 5^\circ$. The theoretical predictions shown for various values of the parameter k_F differ not only in the position of the peaks but also in their magnitudes which illustrates a distinct nature of the employed forms of the YNG interaction given by its dependence on k_F. One can conclude that the larger value of k_F shifts the peaks to lower energies, resulting in a more bound Λ in the hypernucleus.

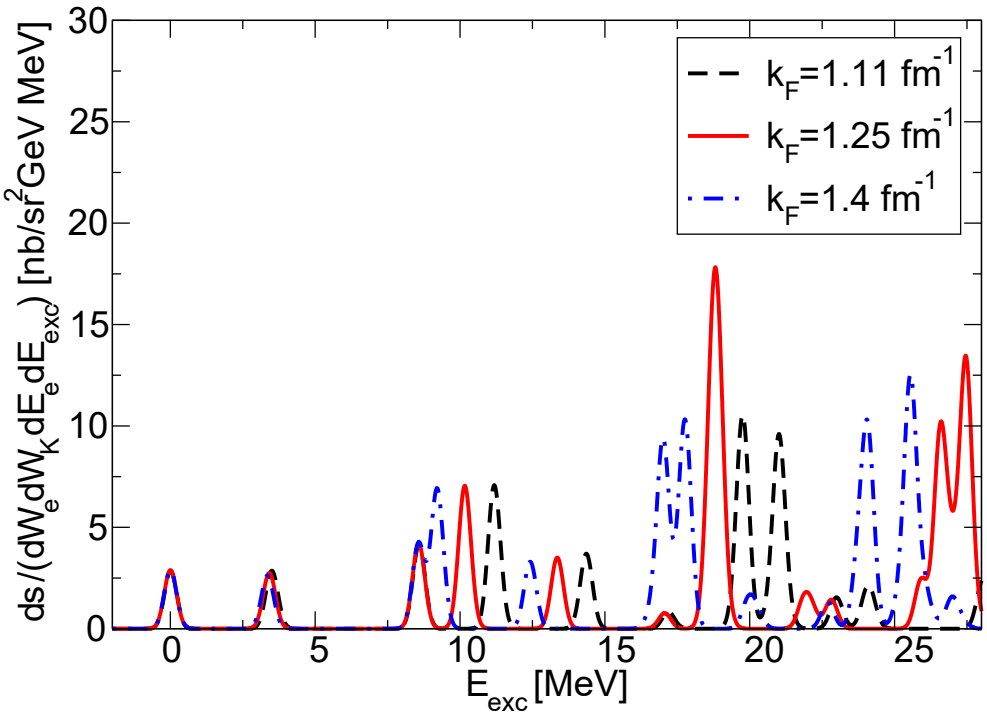

Figure 29: The excitation spectrum for electroproduction of ${}^{40}_{\Lambda}$K calculated using the TD$_\Lambda$ method with different values of the parameter k_F in the G-matrix parametrisation of the Nijmegen-F YN interaction. The results were obtained in kinematics of the upcoming experiment E12-15-008 at Jefferson Laboratory.

4 Conclusion

We investigated in detail various effects in computing the cross sections in electroproduction of hypernuclei. The model calculations are based on the impulse approximation assumed in the optimal factorization where the elementary amplitude is evaluated for an effective proton momentum. The general two-component (CGLN-like) form of the elementary amplitude, developed in this work, allows assuming arbitrary value of the effective momentum wherewith a motion of the initial proton in the nucleus can be included (the Fermi motion effect). Distortion of the final-state kaon wave function is included via the eikonal approximation using the first-order optical potential for the kaon re-scattering on the nucleus. The optical potential can be modified using various forms of the nuclear density. Moreover, our formalism for the DWIA calculations enables accounting for sufficiently large model space of the single-particle states which is important in production of medium- and heavy-mass hypernuclei. The transition densities represented by OBDME can be taken from different many-body calculations which utilize various effective NN and NY interactions. In the calculations we can also use different elementary amplitudes and the single-particle wave functions in computing the radial integrals.

This advanced formalism made it possible to study various effects in predicted cross sections for electroproduction of a wide range of hypernuclei. Particularly, we studied the effects from Fermi motion, kinematics, and kaon distortion as well as from various many-body approaches and forms of the effective YN interactions. The effects were investigated on the angle and energy dependence of the differential cross sections for various hypernuclear states in electroproduction of the p-shell hypernuclei ${}^{12}_{\Lambda}$B and ${}^{16}_{\Lambda}$N and the sd-shell hypernuclei ${}^{40}_{\Lambda}$K and ${}^{48}_{\Lambda}$K. In the case of the p-shell hypernuclei the excitation spectra were also compared with experimental data whereas in the latter case we provided predictions of the spectra for the experiments prepared at the Thomas Jefferson National Laboratory (JLab) in the U.S.A..

In the case of the cross sections for ${}^{12}_{\Lambda}$B and ${}^{16}_{\Lambda}$N we carefully examined the impact of different approaches in computing the kaon momentum (kinematical effects) and different choices of the effective proton momentum (Fermi motion effect). We found that the Fermi motion effects vary significantly in dependence on kinematics and the elementary amplitude. These effects are more noticeable at higher photon energies, specifically above 2 GeV in the laboratory frame, and at small kaon angles. The magnitude and nature of the effects depend strongly on the elementary amplitude

where more pronounced effects were observed for the more modern amplitude BS3 than for the older amplitude Saclay-Lyon A. We also studied the separate components of the full differential cross section and found that both the longitudinal and the transverse-longitudinal interference components are considerably sensitive to the specific value of the proton momentum, mainly at small kaon angles. Generally, the largest differences in the cross sections were observed for the two extreme cases of the proton momentum, particularly with the frozen proton and the frozen Λ hyperon.

We have shown that the results obtained from various approaches in computing the kaon momentum (the computational scheme) reveal quite large differences, especially when the kaon momentum is determined from the energy conservation in the many-body system and therefore the elementary amplitude is off-its-energy shell. However, the uncertainty due to a choice of the computational scheme can be avoided when the optimum value of the effective proton momentum is chosen. In this case the energy conservation is fulfilled both in the many-body and two-body systems and therefore the elementary amplitude is on-shell. Moreover this optimum proton momentum acquires values which are quite close to the mean momentum of the proton in the target nucleus. As the optimum proton momentum depends on the angle with respect to the momentum transfer in the reaction we also investigated a sensitivity of the cross sections to this angle. We can conclude that the choice where the proton moves opposite to the momentum transfer, wherewith the momentum of Λ is minimal, is a reasonable choice. The choice with the optimum proton momentum and the on-shell elementary amplitude we denote as the optimum on-shell approximation.

In the earlier calculations [14, 56, 16] we considered the frozen-proton approximation and utilized a hybrid computational scheme with two different kaon momenta incorporating both the on-energy-shell elementary amplitude and the kaon momentum calculated from the many-body energy conservation. However, with the elaborated formalism and the newly developed form of the elementary amplitude we can employ the optimum on-shell approximation which improves an agreement with the experimental data.

The Fermi motion effects also exhibit apparent systematic variations among hypernuclear states with different spin and parity due to the selective contribution from the longitudinal component of the reduced amplitude A^0_{J0}. These distinctions of the results for two sets of hypernuclear states can be characterized by a “dynamical selection rule." This selection rule significantly influences behaviour of the longitudinal

and transverse-longitudinal components of the cross section in dependence on the spin and parity of the states.

From our analysis of the kaon distortion we can confirm that the distortion suppresses the cross section by several tens of per cent (30–40% for ${}^{12}_{\Lambda}$B and ${}^{16}_{\Lambda}$N) where the effect is larger for the more deeply bound Λ hyperon. The effect is stronger for heavier hypernuclei (e.g. ${}^{40}_{\Lambda}$K), where it amounts up to 50%, and it significantly improves an agreement with the experimental data. The relative size of the effect from kaon distortion is basically uniform in the angular dependence. Tiny effects in the excitation spectrum were observed when different forms of the nuclear density in the kaon-nucleus optical potential were used even if the densities markedly differ in the central part of the nucleus. A dependence of the distortion on the quantum numbers of a hypernucleus state and on the proton momentum was also observed.

We demonstrated that the TD_Λ approach, employed for calculating the one-body density matrix element (OBDME) and the single-particle wave functions, can effectively describe experimental data for the p-shell hypernuclei, yielding results similar to those obtained from the shell-model calculations [5]. Hence, the TD_Λ approach can be applied to predicting the excitation spectra of medium-mass hypernuclei, slated for investigation in an upcoming experiment at JLab. Specifically, we have predicted spectra for the ${}^{48}_{\Lambda}$K and ${}^{40}_{\Lambda}$K hypernuclei, which will be a part of the planned experiment at JLab. In these spectra we have observed appreciable dependence on a form of the effective YN interaction given by its dependence on the Fermi momentum k_F. However, to obtain a better agreement with the data for the ${}^{12}_{\Lambda}$B hypernucleus, describing also the core-excited states, an elaborated method of computing OBDME must be considered, for example using the equation of motion phonon method.

References

[1] Topics in Strangeness Nuclear Physics, edited by P. Bydžovský, A. Gal, and J. Mareš, Lecture Notes in Physics, Vol. 724 (2007).

[2] Hypernuclei and Baryon-Baryon Interaction, edited by E. Hiyama, T. Motoba, and Y. Yamamoto, Prog. Theor. Phys. Suppl. 185 (2010).

[3] A. Gal, E. V. Hungerford, and D. J. Millener, Rev. Mod. Phys. 88, 035004 (2016).

[4] P. Bydžovský, D. Denisova, D. Skoupil, and P. Veselý, Phys. Rev. C 106, 044609 (2022).

[5] P. Bydžovský, D. Denisova, D. Petrellis, D. Skoupil, P. Veselý, G. De Gregorio, F. Knapp, and N. Lo Iudice, Phys. Rev. C 108, 024615 (2023).

[6] Talk by D. Denisova, "Electroproduction of hypernuclei", 16th International Workshop on Meson Physics, Krakow, Poland (2021).

[7] Poster by D. Denisova, "Kinematical effects in electroproduction of hypernuclei", 14th International Conference on Hypernuclear and Strange Particle Physics, Prague, Czech Republic (2022).

[8] Talk by D. Denisova, "Electroproduction of hypernuclei", 17th International Workshop on Meson Physics, Krakow, Poland (2023).

[9] M. Danysz, and J. Pniewski, Phil. Mag. 44, 348 (1953).

[10] M. Jurič et al., Nucl. Phys. B 47, 36 (1972).

[11] O. Hashimoto and H. Tamura, Progress in Particle and Nuclear Physics 57, 564 (2006).

[12] H. Bhang, S. Ajimura, K. Aoki, T. Hasegawa, O. Hashimoto, H. Hotchi, Y. D. Kim, T. Kishimoto, K. Maeda, H. Noumi, Y. Ohta, K. Omata, H. Outa, H. Park, Y. Sato, M. Sekimoto, T. Shibata, T. Takahashi, and M. Youn, Phys. Rev. Lett. 81, 4321 (1998).

[13] M. Sotona and J. Žofka, Czech J. Phys. 40, 1091 (1990).

[14] M. Sotona and S. Frullani, Prog. Theor. Phys. Suppl. 117, 151 (1994).

[15] P. Bydžovský, M. Sotona, T. Motoba, K. Itonaga, K. Ogawa, and O. Hashimoto, Nucl. Phys. A 881, 199 (2012).

[16] T. Motoba, P. Bydžovský, M. Sotona, and K. Itonaga, Prog. Theor. Phys. Suppl., 185, 224 (2010).

[17] C. Bennhold and L. E. Wright, Phys. Rev. C 39, 927 (1989).

[18] T.-S. H. Lee, Z.-Y. Ma, B. Saghai, and H. Toki, Phys. Rev. C 58, 3 (1998).

[19] T. Mizutani, C. Fayard, G. H. Lamot, and B. Saghai, Phys. Rev. C 58, 75 (1998).

[20] J. C. David, C. Fayard, G. H. Lamot, and B. Saghai, Phys. Rev. C 53, 2613 (1996).

[21] J. Cohen, Phys. Rev. C 32, 2 (1985).

[22] S. S. Hsiao and S. R. Cotach, Phys. Rev. C 28, 4 (1983).

[23] R. Shyam, H. Lenske, and U. Mosel, Phys. Rev. C 77, 052201(R) (2008).

[24] R. Shyam, K. Tsushima, and A. W. Thomas, Phys. Lett. B 676, 51 (2009).

[25] T. Mart, L. Tiator, D. Drechsel, and C. Bennhold, Nucl. Phys. A 640, 235 (1998).

[26] T. Mart and B. I. S. van der Ventel, Phys. Rev. C 78, 014004 (2008).

[27] T. Mart and C. Bennhold, Phys. Rev. C 61, 012201(R) (1999).

[28] T. Mart, Phys. Rev. C 62, 038201 (2000).

[29] C. Milner et al., Phys. Rev. Lett. 54, 1237 (1985).

[30] P. H. Pile et al., Phys. Rev. Lett. 66, 2585 (1991).

[31] M. Akei et al., Nucl. Phys. A 534, 478 (1991).

[32] T. Hasegawa et al., Phys. Rev. Lett. 74, 224 (1995); Phys. Rev. C 53, 1210 (1996).

[33] O. Hashimoto et al., Nucl. Phys. A 639, 93c (1998).

[34] T. Miyoshi et al., Phys. Rev. Lett. 90, 232502 (2003).

[35] D. J. Millener, Nucl. Phys. A 804, 84 (2008); 835, 11 (2010); 881, 298 (2012).

[36] L. Yuan et al., Phys. Rev. C 73, 044607 (2006).

[37] J. J. LeRose et al., Nucl. Phys. A 804, 116 (2008).

[38] M. Iodice et al, Phys. Rev. Lett. 99, 052501 (2007).

[39] F. Cusanno et al., Phys. Rev. Lett. 103, 202501 (2009).

[40] D. Skoupil and P. Bydžovský, Phys. Rev. C 93, 025204 (2016).

[41] S. Capstick and W. Roberts, Prog. Part. Nucl. Phys. 45, S241 (2000).

[42] U. Loring, B. C. Metsch, and H. R. Petry, Eur. Phys. J. A 10, 395 (2001); 10, 447 (2001).

[43] S. Janssen, J. Ryckebusch, W. Van Nespen, D. Debruyne, and T. Van Cauteren, Eur. Phys. J. A 11, 105 (2001).

[44] S. Janssen and J. Ryckebusch, Phys. Rev. C 65, 015201 (2001).

[45] S. Janssen, D. G. Ireland, and J. Ryckebusch, Phys. Lett. B 562, 51 (2003).

[46] Zhenping Li, Phys. Rev. C 52, 1648 (1995).

[47] B. Borasoy, P. C. Bruns, U. -G. Meißner and R. Nißler, Eur. Phys. J. A 34, 161 (2007).

[48] S. Steininger and Ulf-G. Meißner Phys. Lett. B 391, 446 (1997).

[49] H. Thom, Phys. Rev. 151, 1322 (1966).

[50] T. Corthals, J. Ryckebusch, and T. Van Cauteren, Phys. Rev. C 73, 045207 (2006).

[51] T. Corthals, T. Van Cauteren, P. Vancraeyveld, J. Ryckebusch, and D.G. Ireland, Phys. Lett. B 656, 186 (2007).

[52] D. Skoupil and P. Bydžovský, Phys. Rev. C 97, 025202 (2018).

[53] V. Pascalutsa, Phys. Rev. D 58, 096002 (1998).

[54] T. Vrancx, L. De Cruz, J. Ryckebusch, and P. Vancraeyveld, Phys. Rev. C 84, 045201 (2011).

[55] P. Bydžovský and T. Mart, Phys. Rev. C 76, 065202 (2007).

[56] F. Garibaldi et al, Phys. Rev. C 99, 054309 (2019).

[57] J. Alcorn, B. D. Anderson, K. A. Aniol, J. R. M. Annand, L. Auerbach, J. Arrington, T. Averett, F. T. Baker, M. Baylac, E. J. Beise et al., Basic instrumentation for Hall A at Jefferson Lab, Nucl. Instrum. Methods Phys. Res., Sect. A 522, 294 (2004).

[58] O. Hashimoto et al, Nucl. Phys. A 835, 121 (2010).

[59] L. Tang et al, Phys. Rev. C 90, 034320 (2014); T. Gogami et al, Phys. Rev. C 103, L041301 (2021).

[60] Jan Pokorný, "Three-body Interactions in Mean-Field Model of Nuclei and Hypernuclei", master thesis, Czech Technical University, Prague, 2018.

[61] J. Millener, Lecture Notes in Physics 724, 31 (2007).

[62] A. Ekstrom, G. R. Jansen, K. A. Wendt, G. Hagen, T. Papenbrock, B. D. Carlsson, C. Forssen, M. Hjorth Jensen, P. Navratil, and W. Nazarewicz, Phys. Rev. C 91, 051301(R) (2015).

[63] Y. Yamamoto, T. Motoba, H. Himeno, K. Ikeda, and S. Nagata, Prog. Theor. Phys. Suppl. 117, 361 (1994).

[64] M. L. Goldberger and K. M. Watson, *Collision Theory*, John Wiley and Sons. Inc., p. 340 (1992).

[65] J. Suhonen, *From Nucleons to Nucleus*, Springer-Verlag (2007).

[66] P. Veselý, G. De Gregorio, and J. Pokorný, Phys. Scr. 94, 014006 (2019).

[67] J. Pokorný, G. De Gregorio, F. Knapp, N. Lo Iudice, and P. Veselý, Acta Phys. Pol. B Proc. Supp. 12, 657 (2019).

[68] W. Horiuchi, Prog. Theor. Exp. Phys. 2021, 12 (2021).

A Evaluation of the production amplitude

To evaluate the matrix element (21) we introduce the coordinates of the baryons

$$\vec{r}_1, \vec{r}_2, ..., \vec{r}_{\rm A-1}, \vec{r}_p \quad \text{for the nucleus and}$$

$$\vec{r}\,'_1, \vec{r}\,'_2, ..., \vec{r}\,'_{\rm A-1}, \vec{r}_\Lambda \quad \text{for the hypernucleus.}$$

The coordinates of the photon and kaon are $\vec{r}_\gamma$ and $\vec{r}_K$, respectively.
We use the following normalization of the states and relation between the coordinate and momentum spaces

$$\langle \vec{r}\,' | \vec{r}\,\rangle = \delta^{(3)}(\vec{r}\,' - \vec{r}\,)\,,$$

$$\langle \vec{r}\,|\,\vec{p}\,\rangle = e^{i\vec{p}\cdot\vec{r}}\,,$$

$$\langle \vec{p}\,'|\,\vec{p}\,\rangle = (2\pi)^3\,\delta^{(3)}(\vec{p}\,' - \vec{p}\,)\,.$$

The corresponding relations of the completeness are

$$\int d^3r\ |\,\vec{r}\,\rangle\langle\,\vec{r}\,| = 1\,,$$

$$\int \frac{d^3p}{(2\pi)^3}\ |\,\vec{p}\,\rangle\langle\,\vec{p}\,| = 1\ .$$

Inserting these multiple relations into the matrix element in Eq. (21) we obtain the following bra-ket scalar product form

$$\begin{aligned} M_\mu \ = \ & \int d^3r'_1 ... \, d^3r'_{\rm A-1}\, d^3r_\Lambda\, d^3r_1 ... \, d^3r_{\rm A-1}\, d^3r_p\, d^3r_K\, d^3r_\gamma\, \frac{d^3p_K\, d^3p_\Lambda\, d^3p_p\, d^3p_\gamma}{(2\pi)^{12}} \\ & \times \langle \Psi_{\rm H}\,|\,\vec{r}\,'_1 ... \, \vec{r}\,'_{\rm A-1}\vec{r}_\Lambda\rangle\ \langle \chi_K\,|\,\vec{r}_K\,\rangle\ \exp[\,i(\vec{p}_K\cdot\vec{r}_K + \vec{p}_\Lambda\cdot\vec{r}_\Lambda)\,] \\ & \times \langle\,\vec{p}_K\,\vec{p}_\Lambda\,|\,Z\,\hat{\rm J}_\mu({\rm A})\,|\,\tilde{\rm p}_\gamma\,\tilde{\rm p}_{\rm p}\,\rangle\ \exp[-{\rm i}(\tilde{\rm p}_\gamma\cdot\tilde{\rm r}_\gamma + \tilde{\rm p}_{\rm p}\cdot\tilde{\rm r}_{\rm p})\,] \\ & \times \langle\,\vec{r}_\gamma\,|\,\chi_\gamma\rangle\ \langle\vec{r}_1 ... \, \vec{r}_{\rm A-1}\vec{r}_p\,|\Psi_{\rm A}\rangle\ \langle\,\vec{r}\,'_1 ... \, \vec{r}\,'_{\rm A-1}\,|\,\vec{r}_1 ... \, \vec{r}_{\rm A-1}\,\rangle\,. \end{aligned} \tag{96}$$

The last term in (96) expresses a passivity of the core particles in the reaction (see Fig. 3) and allows to integrate over the variables $\vec{r}\,'_1$, $...\,\vec{r}\,'_{\rm A-1}$ using the corresponding δ-functions. Then, as a consequence, the coordinates of the nucleus and hypernucleus cores are equal $\vec{R}_c = \frac{1}{\rm A-1}(\vec{r}_1 + ...\vec{r}_{\rm A-1}) = \vec{R}\,'_c$.

It is convenient to introduce the standard Jacobi coordinates to separate the nucleus and hypernucleus center of mass degrees of freedom

$$\vec{\xi}_1 = \vec{r}_2 - \vec{r}_1,\ \ \vec{\xi}_2 = \vec{r}_3 - \frac{1}{2}(\vec{r}_1 + \vec{r}_2), \ldots \vec{\xi}_{\rm A-2} = \vec{r}_{\rm A-1} - \frac{1}{\rm A-2}(\vec{r}_1 + \ ...\,\vec{r}_{\rm A-2})$$

$$\vec{\xi}_p = \vec{r}_p - \frac{1}{\mathrm{A}-1}(\vec{r}_1 + \ldots \vec{r}_{\mathrm{A}-1})$$
$$\vec{\xi}_\Lambda = \vec{r}_\Lambda - \frac{1}{\mathrm{A}-1}(\vec{r}_1 + \ldots \vec{r}_{\mathrm{A}-1})$$
$$\vec{R}_\mathrm{A} = \frac{1}{\mathrm{A}}(\vec{r}_1 + \ldots \vec{r}_{\mathrm{A}-1} + \vec{r}_p)$$
$$\vec{R}_\mathrm{H} = \frac{1}{\mathrm{A}-1+\gamma}(\vec{r}_1 + \ldots \vec{r}_{\mathrm{A}-1} + \gamma\vec{r}_\Lambda)$$

with $\gamma = m_\Lambda/m_p$. Note that we have used expressions for the masses $M_\mathrm{A} = \mathrm{A}\,\mathrm{m_p}$ and $M_\mathrm{H} = (\mathrm{A}-1)\mathrm{m_p} + \mathrm{m}_\Lambda$ neglecting any binding effects in the compound systems. It is also obvious that $\vec{\xi}_\Lambda - \vec{\xi}_p = \vec{r}_\Lambda - \vec{r}_p$. Moreover it holds

$$\vec{R}_\mathrm{A} = \frac{1}{\mathrm{A}}\vec{r}_p + \frac{\mathrm{A}-1}{\mathrm{A}}\vec{R}_c = \vec{r}_p - \frac{\mathrm{A}-1}{\mathrm{A}}\vec{\xi}_p = \vec{r}_\Lambda - \vec{\xi}_\Lambda + \frac{1}{\mathrm{A}}\vec{\xi}_p\,, \tag{97}$$

$$\begin{aligned}\vec{R}_\mathrm{H} &= \frac{\gamma}{\mathrm{A}-1+\gamma}\vec{r}_\Lambda + \frac{\mathrm{A}-1}{\mathrm{A}-1+\gamma}\vec{R}_c = \vec{r}_\Lambda - \frac{\mathrm{A}-1}{\mathrm{A}-1+\gamma}\vec{\xi}_\Lambda \\ &= \vec{R}_\mathrm{A} - \frac{1}{\mathrm{A}}\vec{\xi}_p + \frac{\gamma}{\mathrm{A}-1+\gamma}\vec{\xi}_\Lambda\,.\end{aligned} \tag{98}$$

The Jacobian of the transformation equals to the unity and therefore we can replace the integrating variables as

$$d^3r_1 \ldots d^3r_{\mathrm{A}-1}\, d^3r_p \to d^3\xi_1 \ldots d^3\xi_{A-2}\, d^3\xi_p\, d^3R_\mathrm{A}.$$

The wave functions in the coordinate representation are

$$\begin{aligned}\langle \Psi_\mathrm{H}(\vec{P}_\mathrm{H}) \,|\, \vec{r}_1 \ldots \vec{r}_{\mathrm{A}-1}\, \vec{r}_\Lambda \rangle &= e^{-i\vec{R}_\mathrm{H}\cdot\vec{P}_\mathrm{H}}\, \Phi^*_\mathrm{H}(\vec{\xi}_1, \ldots \vec{\xi}_{\mathrm{A}-2}, \vec{\xi}_\Lambda)\,, \\ \langle \chi_K(\vec{P}_K) \,|\, \vec{r}_K \rangle &= e^{-i\vec{r}_K\cdot\vec{P}_K}\, \chi^*_K(\vec{p}\,'_K, \vec{r}_K - \vec{R}_\mathrm{H})\,, \\ \langle \vec{r}_1 \ldots \vec{r}_{\mathrm{A}-1}\vec{r}_p \,|\Psi_\mathrm{A}(\vec{P}_A)\rangle &= e^{i\vec{R}_\mathrm{A}\cdot\vec{P}_\mathrm{A}}\, \Phi_\mathrm{A}(\vec{\xi}_1, \ldots \vec{\xi}_{\mathrm{A}-2}, \vec{\xi}_p)\,, \\ \langle\, \vec{r}_\gamma \,|\chi_\gamma(\vec{P}_\gamma)\rangle &= e^{i\vec{r}_\gamma\cdot\vec{P}_\gamma}\,.\end{aligned}$$

Note that the wave function of the initial photon is not distorted, it is the plane wave, and that a distortion of the kaon wave function is described by $\chi_\mathsf{K}(\vec{p}\,'_K, \vec{r}_K - \vec{R}_\mathrm{H})$ which equals to the unity in PWIA. This kaon distorted wave depends on the momentum $\vec{p}\,'_K$ which is the kaon-hypernucleus relative momentum associated with the relative coordinate $\vec{r}_K - \vec{R}_\mathrm{H}$. The distorted wave χ_K is obtained as a solution of the kaon-hypernucleus scattering problem. However, due to insufficient knowledge on the $K\Lambda$ scattering we assume that the kaon re-scatters off the nucleus.

We also assume the translational invariance in the two-body elementary-production vertex

$$\langle \vec{p}_K\, \vec{p}_\Lambda \,|\, \hat{\mathrm{J}}_\mu(\mathrm{A}) \,|\, \tilde{\mathrm{p}}_\gamma\, \tilde{\mathrm{p}}_\mathrm{p} \rangle = (2\pi)^3\, \delta^{(3)}(\tilde{\mathrm{p}}_\mathrm{K} + \tilde{\mathrm{p}}_\Lambda - \tilde{\mathrm{p}}_\gamma - \tilde{\mathrm{p}}_\mathrm{p})\, \mathcal{J}_\mu(\tilde{\mathrm{p}}_\mathrm{K}, \tilde{\mathrm{p}}_\gamma, \tilde{\mathrm{p}}_\mathrm{p})\,, \tag{99}$$

where the amplitude $\mathcal{J}_\mu(\vec{p}_K, \vec{p}_\gamma, \vec{p}_p)$ have to be expressed in the two-component form (CGLN-like) to match it with the nonrelativistic nucleus and hypernucleus wave functions. Moreover this form have to be written for a general two-body reference frame defined by an arbitrary value of the proton momentum. Special cases, commonly used in the literature, are the laboratory frame with the proton in rest $\vec{p}_p = 0$ and the photon-proton c. m. frame with $\vec{p}_p = -\vec{P}_\gamma$. Note also that in ordinary nuclear physics the baryons are considered on their mass shell and therefore the two-body energy conservation is violated if the baryons are considered as the bound particles in the compound systems, see Fig. 3.

Using the elementary amplitude, the Jacobi coordinates, and the forms of the wave functions we get for the matrix element in Eq. (96) the expression

$$\begin{aligned} M_\mu \;=\; & Z \int d^3r_\Lambda \, d^3\xi_1 \ldots d^3\,\xi_{\mathrm{A}-2} \, d^3\xi_p \, d^3R_A \, d^3r_K \, \frac{d^3p_p \, d^3p_K}{(2\pi)^6} \, \exp[i(\vec{p}_K - \vec{P}_K)(\vec{r}_K - \vec{r}_\Lambda)] \\ & \times \Phi^*_{\mathrm{H}}(\vec{\xi}_1, \ldots \vec{\xi}_{\mathrm{A}-2}, \vec{\xi}_\Lambda) \, \chi^*_K(\vec{p}\,'_K, \vec{r}_K - \vec{R}_{\mathrm{H}}) \, \mathcal{J}_\mu(\vec{p}_K, \vec{P}_\gamma, \vec{p}_p) \, \Phi_{\mathrm{A}}(\vec{\xi}_1, \ldots \vec{\xi}_{\mathrm{A}-2}, \vec{\xi}_p) \\ & \times \exp\{\, i\,[\,(\vec{P}_\gamma - \vec{P}_K + \vec{p}_p) \cdot \vec{r}_\Lambda - \vec{R}_{\mathrm{H}} \cdot \vec{P}_{\mathrm{H}} - \vec{p}_p \cdot \vec{r}_p + \vec{R}_{\mathrm{A}} \cdot \vec{P}_{\mathrm{A}}]\} \,, \end{aligned} \tag{100}$$

where the δ-function in Eq. (99) allowed to integrate over dp_Λ assuming that $\vec{p}_\Lambda = \vec{p}_p + \vec{p}_\gamma - \vec{p}_K$ in $\mathcal{J}_\mu$ and the phase factor. Moreover, as the only dependence on the photon coordinate $\vec{r}_\gamma$ was in the phase factor (no distortion in the initial state) we could easily integrate over d^3r_γ giving the δ-function $\int d^3r_\gamma \, \exp[i\vec{r}_\gamma(\vec{P}_\gamma - \vec{p}_\gamma)] = (2\pi)^3\delta^{(3)}(\vec{P}_\gamma - \vec{p}_\gamma)$ which was used to integrate over d^3p_γ. Recall that $\vec{p}\,'_K$ is the given relative kaon-hypernucleus momentum but due to a distortion in the final state the kaon wave χ^*_{K} depends on the kaon coordinate $\vec{r}_K$. Therefore we consider the so called eikonal-like approximation, that is, we factorize the integral

$$\int \frac{d^3p_K}{(2\pi)^3} \, \mathcal{J}_\mu(\vec{p}_K, \vec{P}_\gamma, \vec{p}_p) \exp[i(\vec{p}_K - \vec{P}_K)(\vec{r}_K - \vec{r}_\Lambda)] \approx \delta^{(3)}(\vec{r}_K - \vec{r}_\Lambda) \, \mathcal{J}_\mu(\vec{P}_K, \vec{P}_\gamma, \vec{p}_p)$$

supposing that the phase factor is changing more rapidly than is the dependence of $\mathcal{J}_\mu$ on $\vec{p}_K$ and that $\vec{p}_K \approx \vec{P}_K$ in $\mathcal{J}_\mu$. The δ-function then allows to integrate over the kaon coordinate and the elementary amplitude depends on the kaon asymptotic momentum.

The phase factor on the last line of Eq. (100) can be rewritten in terms of the Jacobi

coordinates and the coordinate of the nucleus $\vec{R}_{\rm A}$ which is independent of ξ's

$$
\begin{aligned}
&(\vec{P}_\gamma - \vec{P}_K)\cdot\vec{r}_\Lambda + \vec{p}_p\cdot(\vec{r}_\Lambda - \vec{r}_p) + \vec{P}_{\rm A}\cdot\vec{R}_{\rm A} - \vec{P}_{\rm H}\cdot\vec{R}_{\rm H} = \\
&(\vec{P}_\gamma - \vec{P}_K)\cdot(\vec{R}_{\rm A} + \vec{\xi}_\Lambda - \frac{1}{\rm A}\vec{\xi}_p) + \vec{p}_p\cdot(\vec{\xi}_\Lambda - \vec{\xi}_p) + \vec{P}_{\rm A}\cdot\vec{R}_{\rm A} - \\
&\vec{P}_{\rm H}\cdot(\vec{R}_{\rm A} - \frac{1}{\rm A}\vec{\xi}_p + \frac{\gamma}{{\rm A}-1+\gamma}\vec{\xi}_\Lambda) = \vec{R}_{\rm A}\cdot(\vec{P}_\gamma + \vec{P}_{\rm A} - \vec{P}_K - \vec{P}_{\rm H}) + \\
&\vec{\xi}_\Lambda\cdot(\vec{P}_\gamma - \vec{P}_K + \vec{p}_p - \vec{P}_{\rm H}\frac{\gamma}{{\rm A}-1+\gamma}) - \frac{1}{\rm A}\vec{\xi}_p\cdot(\vec{P}_\gamma - \vec{P}_K + {\rm A}\vec{p}_p - \vec{P}_{\rm H})\,.
\end{aligned}
$$

After integrating over $d^3R_{\rm A}$ we get the δ-function which is needed to introduce the overall amplitude

$$
M_\mu = (2\pi)^3\,\delta^{(3)}(\vec{P}_\gamma + \vec{P}_{\rm A} - \vec{P}_K - \vec{P}_{\rm H})\,\mathcal{T}_\mu\,.
$$

This δ-function expresses the translational invariance in the overall system and the amplitude reads as

$$
\begin{aligned}
\mathcal{T}_\mu \;=\;& Z\,{\rm Tr}\int\frac{d^3p_p}{(2\pi)^3}\,d^3\xi_1...d^3\xi_{{\rm A}-2}\,d^3\xi_p\,d^3r_\Lambda\;\chi^*_K(\vec{p}\,'_K,\vec{r}_\Lambda - \vec{R}_{\rm H})\,\mathcal{J}_\mu(\vec{P}_K,\vec{P}_\gamma,\vec{p}_p) \\
&\times\;\Phi_{\rm A}(\vec{\xi}_1,...\vec{\xi}_{{\rm A}-2},\vec{\xi}_p)\,\Phi^*_{\rm H}(\vec{\xi}_1,...\vec{\xi}_{{\rm A}-2},\vec{\xi}_\Lambda)\;\exp\left[-i\,\vec{\xi}_p\cdot(\vec{p}_p - \frac{1}{\rm A}\vec{P}_{\rm A})\right] \\
&\times\;\exp\left\{i\,\vec{\xi}_\Lambda\cdot\left[\frac{{\rm A}-1}{{\rm A}-1+\gamma}(\vec{P}_\gamma - \vec{P}_K) + \vec{p}_p - \frac{\gamma}{{\rm A}-1+\gamma}\vec{P}_{\rm A}\right]\right\}, \qquad (101)
\end{aligned}
$$

where we have introduced the trace operation (Tr) as the elementary amplitude is a 2×2 matrix on the spin space and the wave functions $\Phi_{\rm A}$ and $\Phi^*_{\rm H}$ are taken as the corresponding spinors. The amplitude in Eq. (101) is written in the ful-folding form, i.e. there is still the integral over the proton momentum which represents averaging over a motion of the initial proton in the nucleus. As the nucleus momentum $\vec{P}_{\rm A}$ was not specified yet the amplitude is computed in a general reference frame.

Considering the laboratory frame, $\vec{P}_{\rm A} = 0$, and assuming that the elementary amplitude is a sufficiently smooth function of the proton momentum and therefore it can be taken outside the integral for some effective value $\vec{p}_p = \vec{p}_{\rm eff}$ we can consider the overall amplitude (101) in the factorized form

$$
\begin{aligned}
\mathcal{T}_\mu \;=\;& Z\,{\rm Tr}\;\mathcal{J}_\mu(\vec{P}_K,\vec{P}_\gamma,\vec{p}_{\rm eff})\int\frac{d^3p_p}{(2\pi)^3}\,d^3\xi_1...d^3\xi_{{\rm A}-2}\,d^3\xi_p\,d^3r_\Lambda\;\chi^*_K(\vec{p}\,'_K,\vec{r}_\Lambda - \vec{R}_{\rm H}) \\
&\times\;\Phi_{\rm A}(\vec{\xi}_1,...\vec{\xi}_{{\rm A}-2},\vec{\xi}_p)\,\Phi^*_{\rm H}(\vec{\xi}_1,...\vec{\xi}_{{\rm A}-2},\vec{\xi}_\Lambda)\;\exp\left[-i\,\vec{p}_p\cdot(\vec{\xi}_p - \vec{\xi}_\Lambda)\right] \\
&\times\;\exp\left\{i\,\vec{\xi}_\Lambda\cdot\left[\frac{{\rm A}-1}{{\rm A}-1+\gamma}(\vec{P}_\gamma - \vec{P}_K)\right]\right\}. \qquad (102)
\end{aligned}
$$

We see that the integral over d^3p_p is trivial and the resulting δ-function allows to integrate also over $d^3\xi_p$ giving $\vec{\xi}_p = \vec{\xi}_\Lambda \equiv \vec{\xi}$. Introducing $B = (A-1)/(A-1+\gamma)$ and $\vec{\Delta} = \vec{P}_\gamma - \vec{P}_K$ and realizing that $\vec{r}_\Lambda - \vec{R}_{\rm H} = B\vec{\xi}$ we obtain the expression

$$\begin{aligned} \mathcal{T}_\mu &= Z\,{\rm Tr}\Big[\,\mathcal{J}_\mu(\vec{P}_K,\vec{P}_\gamma,\vec{p}_{\rm eff})\int d^3\xi_1...d^3\xi_{\rm A-2}\,d^3\xi\ \exp\Big(i\,B\,\vec{\xi}\cdot\vec{\Delta}\Big) \\ &\quad\times\chi^*_K(\vec{p}\,'_K,B\vec{\xi}\,)\,\Phi_{\rm A}(\vec{\xi}_1,...\vec{\xi}_{\rm A-2},\vec{\xi}\,)\,\Phi^*_{\rm H}(\vec{\xi}_1,...\vec{\xi}_{\rm A-2},\vec{\xi}\,)\Big]\,, \end{aligned} \tag{103}$$

which is consistent with Eq. (26).

B CGLN-like amplitudes in a general reference frame

The CGLN-like amplitudes, G_j with $j = 1, 2, ...16$ in Eq. (61), depend on the six scalar amplitudes A_j defined in Eq. (55), which can be calculated using a particular model for electroproduction of K^+ on the proton [52], and on four-momenta of the initial and final particles denoted here as $P_\gamma = (E_\gamma, \vec{P}_\gamma)$, $p_p = (E_p, \vec{p}_p)$, and $p_\Lambda = (E_\Lambda, \vec{p}_\Lambda)$. For the scalar product we use the notation $(a \cdot b) = a_0 b_0 - \vec{a}\,\vec{b}$. The CGLN-like amplitudes are normalised with $N = 1/\sqrt{4 m_\Lambda m_p (E_\Lambda + m_\Lambda)(E_p + m_p)}$ where m_p and m_Λ are the proton and Λ masses, respectively. Except for the virtual photon in electroproduction the particles are on the mass shell, $m^2 = E^2 - \vec{p}^{\,2}$. The CGLN-like amplitudes in terms of the scalar amplitudes and kinematical variables read as

$$
\begin{aligned}
G_1 &= N \Big\{ \Big[(p_\Lambda \cdot p_p)\, E_\gamma - m_\Lambda m_p\, E_\gamma - (P_\gamma \cdot p_\Lambda)(E_p + m_p) - \\
&\quad - (P_\gamma \cdot p_p)(E_\Lambda + m_\Lambda) \Big] A_1 + [(p_\Lambda \cdot p_p) + m_\Lambda m_p + E_\Lambda m_p + E_p m_\Lambda] \\
&\quad \times \Big[(P_\gamma \cdot p_p) A_4 + (P_\gamma \cdot p_\Lambda) A_5 - P_\gamma^2 A_6 \Big] \Big\} \,, \\
G_2 &= N \Big[(E_\gamma + E_p + m_p - E_\Lambda - m_\Lambda) A_1 + (P_\gamma \cdot p_p) A_4 + (P_\gamma \cdot p_\Lambda) A_5 - p_\gamma^2 A_6 \Big] \,, \\
G_3 &= N \left[-(E_p + m_p) A_1 \right] \,, \\
G_4 &= N \Big[-E_\gamma\, A_1 - (P_\gamma \cdot p_p) A_4 - (P_\gamma \cdot p_\Lambda) A_5 + P_\gamma^2 A_6 \Big] \,, \\
G_5 &= N \left[-A_5 + A_6 \right] \,, \\
G_6 &= N \left[-A_4 - A_5 \right] \,, \\
G_7 &= N \left[A_5 \right] \,, \\
G_8 &= N \Big\{ - (E_p + m_p) A_1 - \frac{E_p + m_p}{P_\gamma^2} \Big[(P_\gamma \cdot p_p)\, A_2 + ((P_\gamma \cdot p_\Lambda) - P_\gamma^2)\, A_3 \Big] + \\
&\quad + [(p_\Lambda \cdot p_p) - (P_\gamma \cdot p_p) + m_p (E_\Lambda + m_\Lambda - P_{\gamma 0}) + E_p\, m_\Lambda]\, (A_5 - A_6) \Big\} \,, \\
G_9 &= N \Big\{ (E_\gamma - E_p - m_p - E_\Lambda - m_\Lambda) A_1 + (E_p + m_p)(A_2 + A_3) + \\
&\quad + \Big[(p_p \cdot p_\Lambda) + m_p (E_\Lambda + m_\Lambda - E_\gamma) + E_p\, m_\Lambda \Big] A_4 + \\
&\quad + \Big[(P_\gamma \cdot p_\Lambda) - (P_\gamma \cdot p_p) + (p_p \cdot p_\Lambda) + m_p (E_\Lambda + m_\Lambda - E_\gamma) + E_p m_\Lambda \Big] A_5 - \\
&\quad - P_\gamma^2\, A_6 \Big\} \,,
\end{aligned}
$$

$$
\begin{aligned}
G_{10} &= N\Big\{(E_p+m_p)(A_1-A_3)+\Big[(\,P_\gamma\cdot p_p)-(p_p\cdot p_\Lambda)-m_p(E_\Lambda+m_\Lambda-P_{\gamma 0})- \\
&\quad -E_p\,m_\Lambda\,\Big]\,A_5\Big\}\,, \\
G_{11} &= N\Big\{E_\gamma\,A_1+\frac{E_\Lambda+m_\Lambda-E_p-m_p}{P_\gamma^2}\Big[\,(P_\gamma\cdot p_p)\,A_2+((P_\gamma\cdot p_\Lambda)-P_\gamma^2)\,A_3\Big]+ \\
&\quad +(P_\gamma\cdot p_p)A_4-\Big[\,(P_\gamma\cdot p_p)+E_\gamma(m_\Lambda+m_p)\Big]\,A_5+ \\
&\quad +\Big[\,(P_\gamma\cdot p_p)+(P_\gamma\cdot p_\Lambda)-P_\gamma^2+E_\gamma(m_\Lambda+m_p)\Big]\,A_6\Big\}\,, \\
G_{12} &= N\Big\{2\,E_\gamma\,A_1+(E_p+m_p-E_\Lambda-m_\Lambda)(A_2+A_3)-E_\gamma(m_\Lambda+m_p)(A_4+A_5)- \\
&\quad -[(P_\gamma\cdot p_\Lambda)-(P_\gamma\cdot p_p)]\,(A_4-A_5)-2\,P_\gamma^2A_6\Big\}\,, \\
G_{13} &= N\Big\{-\,E_\gamma\,A_1+(E_\Lambda+m_\Lambda-E_p-m_p)A_3-(P_\gamma\cdot p_p)A_4+ \\
&\quad +[\,(P_\gamma\cdot p_p)+E_\gamma(m_\Lambda+m_p)\,]\,A_5+P_\gamma^2A_6\Big\}\,, \\
G_{14} &= N\left\{\frac{E_p+m_p}{p_\gamma^2}\Big[(P_\gamma\cdot p_p)A_2+((P_\gamma\cdot p_\Lambda)-P_\gamma^2)A_3\Big]+[(P_\gamma\cdot p_p)+E_\gamma m_p]\,(A_5-A_6)\right\}\,, \\
G_{15} &= N\Big\{-\,E_\gamma\,A_1-(E_p+m_p)(A_2+A_3)+E_\gamma\,m_p\,A_4+ \\
&\quad +[\,(P_\gamma\cdot p_p)+E_\gamma\,m_p-(P_\gamma\cdot p_\Lambda)\,]\,A_5+P_\gamma^2A_6\Big\}\,, \\
G_{16} &= N\Big\{(E_p+m_p)A_3-[(P_\gamma\cdot p_p)+E_\gamma\,m_p]\,A_5\Big\}\,.
\end{aligned}
$$

C Spherical amplitudes in a general reference frame

The non spin-flip ($S = 0$) spherical amplitudes $\mathcal{F}^S_{\lambda\eta}$ introduced in Eq. (64) can be written in terms of the CGLN-like amplitudes and the spherical components of the photon ($\vec{p}_\gamma$), proton ($\vec{p}_p$) and kaon ($\vec{p}_K$) momenta

$$
\begin{aligned}
\mathcal{F}^0_{-10} &= -|\vec{p}_\gamma|\,[\,(p_p)^1_{-1}\,G_2 + (p_K)^1_{-1}\,G_3\,] + [\,(p_p)^1_0\,(p_K)^1_{-1} - (p_p)^1_{-1}\,(p_K)^1_0\,]\,G_4 + \\
&\quad + D\,[\,(p_p)^1_{-1}\,G_6 + (p_K)^1_{-1}\,G_7\,] \\
\mathcal{F}^0_{00} &= -[\,(p_p)^1_{-1}\,(p_K)^1_1 - (p_p)^1_1\,(p_K)^1_{-1}\,]\,G_4 + D\,[\,|\vec{p}_\gamma|\,G_5 + (p_p)^1_0\,G_6 + (p_K)^1_0\,G_7\,] \\
\mathcal{F}^0_{10} &= |\vec{p}_\gamma|\,[\,(p_p)^1_1\,G_2 + (p_K)^1_1\,G_3\,] - [\,(p_p)^1_0\,(p_K)^1_1 - (p_p)^1_1\,(p_K)^1_0\,]\,G_4 + \\
&\quad + D\,[\,(p_p)^1_1\,G_6 + (p_K)^1_1\,G_7\,]
\end{aligned}
$$

Similarly we can write down the spin flip ($S = 1$) spherical amplitudes

$$
\begin{aligned}
\mathcal{F}^1_{11} &= G_1 - (p_p)^1_{-1}\,[\,(p_p)^1_1\,G_{12} + (p_K)^1_1\,G_{13}\,] - (p_K)^1_{-1}\,[\,(p_p)^1_1\,G_{15} + (p_K)^1_1\,G_{16}\,] \\
\mathcal{F}^1_{10} &= |\vec{p}_\gamma|\,[\,(p_p)^1_1\,G_9 + (p_K)^1_1\,G_{10}\,] + (p_p)^1_0\,[\,(p_p)^1_1\,G_{12} + (p_K)^1_1\,G_{13}\,] + \\
&\quad + (p_K)^1_0\,[\,(p_p)^1_1\,G_{15} + (p_K)^1_1\,G_{16}\,] \\
\mathcal{F}^1_{1-1} &= -(p_p)^1_1\,[\,(p_p)^1_1\,G_{12} + (p_K)^1_1\,G_{13}\,] - (p_K)^1_1\,[\,(p_p)^1_1\,G_{15} + (p_K)^1_1\,G_{16}\,] \\
\mathcal{F}^1_{01} &= -|\vec{p}_\gamma|\,[\,(p_p)^1_{-1}\,G_{11} + (p_K)^1_{-1}\,G_{14}\,] - (p_p)^1_0\,[\,(p_p)^1_{-1}\,G_{12} + (p_K)^1_{-1}\,G_{15}\,] - \\
&\quad - (p_K)^1_0\,[\,(p_p)^1_{-1}\,G_{13} + (p_K)^1_{-1}\,G_{16}\,] \\
\mathcal{F}^1_{00} &= G_1 + |\vec{p}_\gamma|\,[\,|\vec{p}_\gamma|\,G_8 + (p_p)^1_0\,G_9 + (p_K)^1_0\,G_{10} + (p_p)^1_0\,G_{11} + (p_K)^1_0\,G_{14}\,] + \\
&\quad + (p_p)^1_0\,(p_p)^1_0\,G_{12} + (p_p)^1_0\,(p_K)^1_0\,(G_{13} + G_{15}) + (p_K)^1_0\,(p_K)^1_0\,G_{16} \\
\mathcal{F}^1_{0-1} &= -|\vec{p}_\gamma|\,[\,(p_p)^1_1\,G_{11} + (p_K)^1_1\,G_{14}\,] - (p_p)^1_1\,[\,(p_p)^1_0\,G_{12} + (p_K)^1_0\,G_{13}\,] - \\
&\quad - (p_K)^1_1\,[\,(p_p)^1_0\,G_{15} + (p_K)^1_0\,G_{16}\,] \\
\mathcal{F}^1_{-11} &= -[(p_p)^1_{-1}\,(p_p)^1_{-1}\,G_{12} + (p_p)^1_{-1}\,(p_K)^1_{-1}\,(G_{13} + G_{15}) + (p_K)^1_{-1}\,(p_K)^1_{-1}\,G_{16}] \\
\mathcal{F}^1_{-10} &= |\vec{p}_\gamma|\,[\,(p_p)^1_{-1}\,G_9 + (p_K)^1_{-1}\,G_{10}\,] + (p_p)^1_0\,[\,(p_p)^1_{-1}\,G_{12} + (p_K)^1_{-1}\,G_{13}\,] + \\
&\quad + (p_K)^1_0\,[\,(p_p)^1_{-1}\,G_{15} + (p_K)^1_{-1}\,G_{16}\,] \\
\mathcal{F}^1_{-1-1} &= G_1 - (p_p)^1_1\,[\,(p_p)^1_{-1}\,G_{12} + (p_K)^1_{-1}\,G_{13}\,] - (p_K)^1_1\,[\,(p_p)^1_{-1}\,G_{15} + (p_K)^1_{-1}\,G_{16}\,]
\end{aligned}
$$

The spherical components of the momenta and the parameter D are

$$(p_K)^1_0 = |\vec{p}_K| \cos\theta_K, \qquad (p_K)^1_{\pm 1} = \mp \frac{|\vec{p}_K|}{\sqrt{2}} \sin\theta_K \, \exp(\pm i \Phi_K)$$

$$(p_p)^1_0 = |\vec{p}_p| \cos\theta_p, \qquad (p_p)^1_{\pm 1} = \mp \frac{|\vec{p}_p|}{\sqrt{2}} \sin\theta_p \, \exp(\pm i \Phi_p)$$

$$D = \, i \, |\vec{p}_\gamma \, | \, |\vec{p}_p| \, |\vec{p}_K| \sin\theta_p \sin\theta_K (\cos\Phi_p \sin\Phi_K - \sin\Phi_p \cos\Phi_K) \, .$$

The polar angles θ_K and θ_p are determined with respect to the photon momentum and the azimuthal angles Φ_K and Φ_p are defined with respect to the leptonic plane as shown in Fig. 4.

D Details on the model calculations of the cross sections in photo- and electroproduction of hypernuclei

The cross sections in photo- and electroproduction of hypernuclei in various excited states are calculated in the model which utilize the impulse approximation and the many-body matrix element is assumed in the optimum factorization approximation (OFA) where the elementary production amplitude is evaluated at an effective proton momentum. The full unpolarized differential cross section and its separated contributions (T, L, TL, and TT) are computed in the Laboratory frame where the initial nucleus is at rest. The results are obtained in dependence on the kaon angle or the virtual-photon energy for given kinematics which allows to draw different distributions of the cross sections and study various effects resulting from the optional input data and model assumptions.

The hypernucleus production cross sections are directly calculated from the reduced amplitudes which include three main ingredients: the elementary amplitude (EA), the nucleus-hypernucleus transition matrix elements expressed in terms of the so called One Body Density Matrix elements (OBDME), and the radial integrals.

The elementary production is calculated for an arbitrary value of the effective proton momentum in OFA which is specified in the input file of the computer program. If the special cases, the optimum momentum on-shell approximation and the case with frozen Lambda, are required the numerical value of the proton momentum is calculated by the computer program. Various isobar models for EA can be used as the model parameters are taken from a file which name is provided in the input file. These possible choices allow to study the effects from the Fermi motion of the initial proton and from considering different EA.

The OBDME are also given in an input file and these data are results of the calculations which use various many-body approaches (SM, HF, TDA) and accessible NN and YN effective interactions. Changing the input file with OBDME allows to study effects from the many-body approaches as well as from different effective interactions.

The radial integrals (RI) are calculated using the proton and Λ single-particle wave functions provided in the files with tables of values of the wave functions. The names of these files are given in the input file and various forms of the wave functions (HO, HF,

WS) can be used. The other ingredient in computing RI is the kaon distorted wave which is included in the eikonal approximation. The kaon-nucleus optical potential is constructed from the kaon-nucleon (KN) scattering amplitude and the nuclear density. Both these components are specified in the input and one can change them to study effects which stem from using various input data. The KN amplitude is given in the isospin formalism, for I= 0 and 1, and the proper isospin averaging of the amplitude is performed in computing the parameter α and σ_{tot}.

In the calculation of the reduced amplitudes one can include a sufficiently large model space of the single-particle (s-p) states, denoted with the quantum numbers $[n, l, j]$. This means that it is possible to sum up all relevant s-p transitions, i.e. those for which the OBDME are significantly big. This is especially important in extending the model calculations to production of the medium- and heavy-mass hypernuclei where big model spaces are needed. Note, however, that usually one (or two) OBDME with a specific s-p transition dominates in the amplitude for a given hypernucleus state.

The computer code is organized as follows:
The main program first reads an input file which includes essential information for the calculation such as parameters of the reaction, kinematics, parameters and switches specifying the model calculation, and the names of the other files with required data. Once the input data is read the program proceeds with preparing the parameters and other data for the angle and radial integrations (Gaussian mesh points and weights), the elementary amplitude (model parameters), kaon distortion (kaon-nucleon amplitudes and nucleus density), and more detailed kinematics (of the virtual-photon, proton, kaon, hypernucleus).

The code continues with further steps, utilizing the prepared data and functions to complete the calculation of the electroproduction cross section. The program runs in the loops over the considered multiplets and hypernucleus final states. Data from the file containing the OBDME is read to obtain selected single-particle states for Λ $[n'l'j']$ and the proton $[nlj]$ and the corresponding nucleus-hypernucleus matrix elements of the single-particle transition operator. Using this data the nucleus-hypernucleus structure coefficients $H^{LSJ}_{n'l'j'nlj}$ are computed for the given transitions and stored in the field "HLSJ".

For each hypernucleus state in a multiplet, the program initiates the loop over kaon angles, including polar and azimuthal angles, and the kaon momentum is determined

in dependence on the chosen computational scheme (2-body, many-body, hybrid). Then, the spherical elementary amplitudes are computed for the given momenta of the photon, proton, and kaon. Next, the single-particle radial wave functions for the selected quantum numbers of the proton and Λ are prepared. These radial wave functions are crucial for calculating the radial integrals, including their phase factors due to the rotation for a given angle Φ_K.

In the subsequent step, the reduced amplitudes A^{λ}_{Jm} are computed as the sum over all considered single-particle quantum numbers of the products of the radial integrals and the nucleus-hypernucleus structure coefficients stored in HLSJ. After the Clebsch-Gordan coefficient is added to the sum further summing is performed over the quantum numbers L and M from the partial-wave decomposition. The result is then multiplied by the elementary amplitude and summed over the spin. Finally, the reduced amplitudes are summed over J and m to obtain the separated cross sections for the specific hypernucleus final state and kaon angles.

The process described above is repeated for different hypernuclear states and kaon angles, allowing for calculations of the cross sections for various final states and different angular dependence. This enables researchers to study the angular and energy distributions of the cross sections for various hypernucleus states by providing the output in the form of tables of the kaon angle or energy and the separated cross sections for a list of the hypernucleus states given in the input file.

The proton and Λ hyperon single-particle radial wave functions are computed for the Woods-Saxon and harmonic-oscillator potentials. However, other forms of the wave functions, such as Hartree-Fock, must be supplied by other programs and are read by the program as input data.

The kaon-nucleon scattering amplitude can be computed using various models, e.g. by the separable model for the KN scattering. This flexibility allows to explore different theoretical approaches and select the most suitable one for specific studies of hypernuclear electroproduction.

List of Publications

- P. Bydžovský, D. Denisova, D. Skoupil, and P. Veselý: *Fermi motion effects in electroproduction of hypernuclei*. Phys. Rev. C 106, 044609 (2022).
- P. Bydžovský, D. Denisova, D. Petrellis, D. Skoupil, P. Veselý, G. De Gregorio, F. Knapp, and N. Lo Iudice: *Self-consistent many-body approach to the electroproduction of hypernuclei*. Phys. Rev. C 108, 024615 (2023).